Simultaneous DTI and rs-fMRI using the navigated diffusion sequence

MSc(Med) in Biomedical Engineering

Masters Thesis

Presented by:

Mwape Mofya

MFYMWA001

Biomedical Engineering

Dept. of Human Biology

University of Cape Town

Supervised by:

Prof. Ernesta M. Meintjes

Biomedical Engineering

Dept. of Human Biology

University of Cape Town

and

Dr. Alkathafi A. Alhamud

Biomedical Engineering

Dept. of Human Biology

University of Cape Town

and

Dr. Paul A. Taylor

Biomedical Engineering

Dept. of Human Biology

University of Cape Town

January 2016

Submitted to the Department of Human Biology at the University of Cape Town in partial fulfilment of the academic requirements for a Master of Science (Medicine) degree in Biomedical Engineering

Plagiarism Declaration

1. I know that plagiarism is wrong. Plagiarism is to use another's work and pretend that it is one's own.

2. I have used the American Psychological Association convention for citation and referencing. Each contribution to, and quotation in, this report from the work(s) of other people has been attributed, and has been cited and referenced.

3. This report is my own work.

4. I have not allowed, and will not allow, anyone to copy my work with the intention of passing it off as their own work or part thereof.

M Mofya

Signed by candidate

Signature removed

Date: January 28, 2016.

Abstract

Blood oxygenation level dependent (BOLD) functional magnetic resonance imaging (fMRI) and diffusion tensor imaging (DTI) experiments are normally performed separately. The idea of extracting inherently co-registered activation/connectivity maps and diffusion parameters has resulted in efforts to develop methods for simultaneous fMRI and DTI data acquisition. Recently, a 3D echo planar imaging (EPI) acquisition was successfully inserted after each DTI volume to perform real-time motion correction, with the two sequence protocols remaining separate. We examined using a single 3D EPI acquisition, inserted following each DTI volume acquisition (hereafter called the single nav sequence), modified to acquire BOLD resting state fMRI (rs-fMRI) data. We also investigated inserting a second 3D EPI acquisition in the middle of each DTI volume acquisition (hereafter called the double nav sequence) to increase fMRI temporal resolution. Two adult subjects were scanned with the navigated sequences and the standard separate 2D EPI BOLD and DTI acquisitions for comparison. Preprocessing and analysis of data was performed using FATCAT, AFNI, FSL and in-house Python scripts. Four standard resting state networks (RSNs) were visually identified using the navigated diffusion sequences. While RSNs were apparent in the single nav case, they were quite noisy and in some cases entire regions did not show connectivity. The double nav connectivity maps were more similar to the standard BOLD connectivity maps in terms of the spatial extent of the regions showing connectivity to the seed. The whole brain distributions of fractional anisotropy (FA) and mean diffusivity (MD) were similar among the different acquisition protocols. The jackknife standard error was comparable between the navigated and standard protocols. Further comparisons of diffusion data made using probabilistic tractography and connectivity matrices showed overall small differences indicating that connections derived from the standard DTI, single nav and double nav protocols were overall similar. We have therefore shown a significant "proof of concept" of successfully acquiring simultaneous DTI and rs-fMRI data, and therefore for investigating brain structural and functional connectivity simultaneously.

Acknowledgements

I would like to express my gratitude to the following people and institutes who assisted me with the work presented in this thesis:

- My supervisor Professor Ernesta Meintjes, thank you for being patient with me and all your tremendous efforts in guiding me through my Masters. I could not wish for a better supervisor.
- Dr. Ali Alhamud, you were very strict and always tried to push me to do my best. Thank you for also being very kind to me.
- Dr. Paul Taylor, you always made time for me in you very busy schedule. Thank you for introducing me to this field and for your continuous support through my Masters work.
- Dr. Andrè van der Kouwe, you were very friendly. Thank you for all the useful comments and ideas.
- Participants who were scanned, thank you for willingly sharing your precious time during the process of scanning.
- Muhammad Saleh, Lindie Du Plessis, Frances Roberson, Martha Holmes, Jadrana Toich, Emmanuel Nwosu, Jia Fan, Stephen Jermy, Priya Lakshmi, Kenneth Mbugua, Kerry Woods and Neal Derman for your friendships and many useful discussions. You always knew how to make me laugh when I felt like my head was about to explode.
- The South African Research Chairs Initiative of the Department of Science and Technology and National Research Foundation of South Africa, the Medical Research Council of South Africa, the NIH grants R21AA017410, R21MH096559, R01HD071664 and the University of Cape Town for funding this project.

Contents

Chapter 1

Introduction

Several non-invasive neuroimaging techniques, including magnetic resonance imaging (MRI), electro-encephalography (EEG), and computerized tomography (CT) are available to provide different information on brain function or structure. For example, functional MRI (fMRI) reveals the functional relations of brain regions; structural MRI (sMRI) provides physical information about the tissue types of the brain (i.e., gray matter (GM), white matter (WM) and cerebrospinal fluid (CSF)). Diffusion tensor imaging (DTI) can additionally provide information on structural connectivity among networks in the brain.

As different neuroimaging techniques allow for the collection of information about different features of the brain, combining complementary data from multiple techniques mutually enhances the amount of information obtained and may also serve to overcome technological limitations associated with each individual method. For example, while both EEG and fMRI measure brain function, the former has a poor spatial resolution (about 5 to 9 cm) but a good temporal resolution (on the order of milliseconds), and the latter has a good spatial resolution (about 2 to 3 mm) but a poor temporal resolution (on the order of seconds). Therefore, significant advantages can be realized by combining fMRI and EEG in measuring brain function (Menon et al., 1997; Mullinger and Bowtell, 2011; Valdes-Sosa et al., 2009).

In recent years, it has become common, and of clinical importance, to combine DTI and fMRI data given the complementary information embedded in the two techniques. One of the earliest combined fMRI and DTI studies was by Werring et al. (1998), in order to monitor the recovery of a patient from a traumatic brain injury. The fMRI and DTI data complemented each other in finding that the patient's successful recovery was due to the survival of existing motor

pathways. A year later, the same authors conducted the first study combining fMRI and DTI in healthy human subjects to demonstrate the feasibility of combining data from the two techniques (Werring et al., 1999). The aim of the study was to investigate the structural connections between activated brain regions. As predicted, the combined fMRI/DTI data results showed that the blood oxygenation level dependent (BOLD) response occurs in areas of low anisotropy (i.e. gray matter).

Following the first successful applications of combined fMRI and DTI, many studies have explored further potentials of this technique. In many studies, this technique has been used with the hope of gaining more insight into the brain structural and functional relationships. For example, DTI scans have been used to reconstruct white matter pathways between functionally connected brain regions (Greicius et al., 2009; Honey et al., 2009; Koch et al., 2002; van den Heuvel et al., 2009). In some cases, fMRI activation maps have been used as a guide to DTI tractography or to validate DTI-related results (Dougherty et al., 2005; Guye et al., 2003; Kim et al., 2006; Lowe et al., 2008; Schonberg et al., 2006; Shimono et al., 2012; Supekar et al., 2010; Upadhyay et al., 2007). This is because DTI is a relatively new neuroimaging technique compared to fMRI. With the advent of DTI-tractography, white matter bundles connecting different brain regions can be delineated. DTI-tractography has been hard to verify experimentally, and so the use of fMRI can help to limit some obvious errors, and to guide it. One of the most common applications of combined fMRI and DTI is in neurosurgical planning, providing valuable information that cannot be obtained from each of these techniques separately. For example a combination of DTI and fMRI analysis has provided guidance on the resectioning of brain tumours adjacent to important white matter fibre tracts and also eloquent cortical areas (Hendler et al., 2003; Schonberg et al., 2006; Smits et al., 2007).

In the vast majority of studies combining fMRI and DTI, data have been acquired separately and then combined during postprocessing. Several procedures ranging from qualitative to quantitative ones are available to combine the data, and the appropriate method is selected based on the particular problem being investigated (Rykhlevskaia et al., 2008). The idea of extracting inherently co-registered activation maps and diffusion parameters has resulted in some recent efforts to develop methods for simultaneous fMRI and DTI data acquisition, first attempted by Wheeler-Kingshot et al. (2001). Despite their experiment not being successful due to the interference of the DTI signal in the fMRI scan, it showed the possibility of simultaneously acquiring fMRI and DTI data. After this attempt, to the best of our knowledge, no other attempts have been reported until recently in 2013 (Alhamud et al., 2013).

Alhamud et al. (2013) demonstrated the feasibility of performing simultaneous acquisition of BOLD fMRI and DTI data using the navigated DTI pulse sequence (Alhamud et al., 2012). A three-dimensional (3D) echo planar imaging (EPI) navigator inserted following each diffusion volume acquisition, initially to perform real-time motion tracking, could be used to acquire fMRI data. The initial application of simultaneous fMRI and DTI using the navigated diffusion sequence suffered from low temporal resolution (on the order of 6.5 s) and the contrast of the BOLD-weighted images were partially affected by the T_1 relaxation of preceding diffusion imaging. In this work, we aim to optimize the navigated DTI pulse sequence (hereafter called the single nav sequence) to acquire simultaneously with DTI, BOLD resting state fMRI (rs-fMRI) (Biswal et al., 1995) data for functional analyses of resting state functional connectivity. Additionally, we investigate inserting another navigator into the middle of the diffusion sequence (hereafter called the double nav sequence) in order to increase the fMRI temporal resolution while still minimizing cross-excitation during the acquisition.

Another area of interest in neuroimaging studies has been the characterization and visualization of the uncertainty of estimated DTI parameters. It is important to characterize uncertainty in DTI parameters, such as the anisotropy indices and the principal eigenvector, for robust fibre tract reconstruction. The uncertainty of DTI parameters can be quantified through statistical confidence intervals. Bootstrap methods have previously been mostly used for this purpose (Efron, 1987; Jones, 2003; Jones and Pierpaoli, 2005). However, bootstrap methods require either the acquisition of extra data or model-dependent assumptions. Therefore, in this work we propose using the jackknife resampling technique, which is model free, computationally efficient and, in contrast to traditional bootstrap methods, does not require several repeated acquisitions. We use simulations to show its validity and use in estimating confidence intervals.

This thesis presents two novel features for MRI data acquisition and processing. First, we demonstrate the suitability of the jackknife resampling technique to characterize uncertainty estimates in DTI parameters. Then we demonstrate the possibility of the simultaneous acquisition of fMRI and DTI data. In this latter part, we use the optimal proposed jackknife implementation from the first part to quantitatively compare DTI data from the three different DTI protocols: standard DTI, single nav and the double nav.

1.1 Thesis outline

Chapter 2 presents the basic theory of MRI and the different contrasts it can provide, including an introduction to fMRI and DTI.

Chapter 3 is a study investigating the ability of the jackknife resampling technique to determine confidence intervals of DTI parameters. In this study, we examine the various features to determine an optimal jackknife implementation in real DTI data. This work, which has been presented as an independent manuscript and has been submitted for review to the Magnetic Resonance Imaging journal, was co-authored by Dr. Ali Alhamud, Prof. Ernesta M. Meintjes and Dr. Paul A. Taylor. All the work was done by the student, with input from the co-authors.

Chapter 4 describes the modification and optimization of the navigated diffusion sequence for simultaneous DTI-fMRI. This chapter also describes how the jackknife technique is applied to compare the overall variation of DTI parameters from the three different DTI protocols.

Chapter 5 presents the results obtained from optimization of the navigated diffusion sequence for simultaneous DTI-fMRI.

Chapter 6 is a discussion, summarising the main findings of our attempt to simultaneously acquire DTI and fMRI data. It also provides the overall conclusions drawn from this work as well as recommendations for future work.

Part of this work was presented at the International Society for Magnetic Resonance in Medicine (ISMRM) conference and appears in the following proceeding: Mofya M, Alhamud AA, Taylor PA, van der Kouwe AJW, Meintjes EM, Simultaneous acquisition of structural and resting state functional connectivity data using a volumetric navigated diffusion sequence; Proc ISMRM 23; Toronto Canada, May 2015 (#2110).

Chapter 2

Magnetic Resonance Imaging

2.1 Introduction

MRI had its humble beginnings in the 1970s (Lauterbur, 1973) but has since become the preferred imaging technique for a large proportion of radiological examinations. Most clinical MRI is based on the sensitivity to the presence and properties of water, which makes up 75% of the human body. The properties and amount of water in tissue can alter dramatically with disease and injury which makes MRI very sensitive as a diagnostic technique. MRI is used not just to image anatomy, but also to investigate brain function and structure.

In the late 1970s, computerized tomography (CT) was commonly used to generate high resolution images of the human body. Around the same time, there was substantial interest in MRI as a potential diagnostic tool, over CT because MRI could provide similar information without X-ray exposure. MRI was then known as nuclear magnetic resonance (NMR) imaging and when the technique was introduced in hospitals, the word 'nuclear', although scientifically accurate, fell into disfavour to the majority of people, as it implied a connection with nuclear radiation. In the early 1980s, the word 'nuclear' was dropped and the technique became known as MRI.

MRI scanners vary in size and shape but the basic design is the same. A modern MRI scanner is shown in Figure 2.1.1. It typically consists of:

- a main magnet that produces a strong constant magnetic field;
- shim coils around the main magnet for homogenizing the main magnetic field;

- radio frequency (RF) transmit and receive coils, which excite and detect the MR signals;
- a set of three gradient coils that produce gradient fields in orthogonal directions used to localize the MR signal;
- a computer system for scanner control, image display and archiving;
- physiological monitoring equipment.

Figure 2.1.1: A modern MRI scanner. Image adapted from http://www.nhs.uk/conditions/MRI-scan/Pages/Introduction.aspx

MRI is a rapidly changing and growing imaging modality. It has supplanted many traditional imaging modalities, such as CT and positron emission tomography (PET), because it is non-invasive and inherently safe to the patient as a result of it not requiring ionizing radiation or radio tracers. In addition, whereas most imaging techniques depict differences in one or two tissue characteristics, MRI has three tissue variables - proton density (often abbreviated to PD), T_1 and T_2 relaxation times - from which to construct its images and can create images with contrast arising from almost any physiological process. In this chapter, we shall review the basic principles of MRI, and the generation of contrast based on the three tissue characteristics, physiological parameters and the sensitivity of MR to flow.

2.2 Principles of MRI

2.2.1 Theory

The rigorous understanding of MRI begins with the sub-nuclear particles (quarks and gluons), to subatomic particles (electrons, protons and neutrons) and finally to the bulk sample scale of

millions of atomic molecules. Each scale is described by a different branch of physics. The sub-nuclear scale is governed by quantum field theory; the subatomic scale is governed by quantum mechanics and the bulk sample scale of atomic molecules is governed by classical mechanics. Protons are made up of one down quark and two up quarks, each with a spin of 1/2. The down quark has charge of -1/3 while the up quarks each have a charge of +2/3, which sums up to a charge of +1. The nucleus of the hydrogen atom contains one proton and therefore the nuclear spin is 1/2 by virtue of spin cancellation from the anti-parallel alignment of two of the three quarks. Subatomic particles have quantum magnetic properties which they derive from intrinsic spin and orbital angular momentum. The overall angular momentum of an atom arising from both orbital and spin angular momenta can either be zero, as for closed shell atoms, or non-zero, as for open shell atoms. When the total angular momentum is non-zero, an atom possesses a permanent magnetic dipole moment, μ. The nuclear magnetic moments present in atoms with an odd number of nucleons (for example, ^{1}H, ^{15}N, ^{19}F, ^{23}Na, ^{31}P, ^{13}C), are several orders of magnitude smaller than those of electrons. However, nuclei precess, absorb, and emit electromagnetic signals in the radio frequency range. This range is non-ionizing radiation, and makes MRI a safer choice than ionizing imaging modalities such as CT. The nucleus used most often in MRI is the Hydrogen nucleus, primarily because of its large physiological concentration in the human body (i.e., Hydrogen atoms are contained in water molecules, which make up 75% of the human body, and in many organic molecules), as well as its relatively simple nuclear structure (i.e., the Hydrogen nucleus is basically a proton). Other biological elements that are MR active and their relative sensitivities are listed in Table 2.2.1.

Element	Nuclei	Abundance in human body (mole/litre)	Magnetic moment μ	Relative sensitivity
Hydrogen	^{1}H	88	2.793	1
Oxygen	^{17}O	16×10^{-3}	-1.893	9×10^{-6}
Fluorine	^{19}F	4×10^{-6}	2.627	3×10^{-8}
Sodium	^{23}Na	80×10^{-3}	2.216	1×10^{-4}
Phosphorus	^{31}P	75×10^{-3}	1.131	6×10^{-5}

Table 2.2.1: Biologically relevant elements that are candidates for producing MR images. Hydrogen, having the largest magnetic moment and greatest abundance is the best element for general clinical utility.

Even though each scale (i.e., microscopic or macroscopic) is governed by a different branch of physics, certain phenomena are only meaningful over specific levels. For example, a magnetic dipole placed in an external magnetic field experiences a torque. However, the concept of

torque is a classical concept. It is deterministic and continuous, and is meaningful only at the atomic bulk sample scale. On a microscopic level, such as on the scale of single electrons and nucleons, quantum mechanics is the operative physics, and the state transitions are quantized. Furthermore, the scales are physically linked. For example, the bulk magnetization, which is as a result of a collection of atoms aligning with an external constant magnetic field, is the net sum of individual atomic moments. Furthermore, an RF pulse, oscillating at the frequency of the protons and acting directly on individual protons, can be used to torque the bulk magnetization vector and change its direction. Here, several aspects of MRI are described using classical concepts for the purposes of visualization and understanding.

In the body, thermal radiation randomizes the directions of the magnetic moments of the hydrogen nucleus. Therefore, in the absence of an external magnetic field, the net magnetization, $\mathbf{M}$ - defined as the overall sum of all magnetic moments in a given volume, which can also change as a function of time, t,

$$\mathbf{M}(t) = \sum_j \vec{\mu}_j(t) \tag{2.2.1}$$

- is zero. Using the principles of classical physics, the net magnetization $\mathbf{M}$ is used rather than individual nuclear spins. The net magnetization $\mathbf{M}$ is a vector that can be decomposed into a longitudinal magnetization component $\mathbf{M}_z$ along the z direction and a transverse component $\mathbf{M}_{xy}$ in the xy plane. When a patient is placed in an MRI scanner, the large constant magnetic field, $\mathbf{B}_0$, produced by the magnet of the MRI scanner, causes the randomly oriented magnetic moments to partially align either parallel or anti-parallel to $\mathbf{B}_0$, and the orientations are often referred to as "spin up" and "spin down", respectively. The parallel orientation is the lower energy state for magnets, and thereby is the more energetically favourable state for protons in a sample, the population distribution of which is determined by the absolute temperature, T, in the human body. This relationship is given by,

$$\frac{N_h}{N_l} = \exp(-\Delta E/k_B T), \tag{2.2.2}$$

where N_h is the number of protons in the higher energy state, N_l is the number of protons in the lower energy state, ΔE is the energy difference between the two states, and k_B is the Boltzmann constant. Cancellation of spins will occur due to their parallel and anti-parallel orientations and the excess small spin $(N_l - N_h)$ will be in the direction of $\mathbf{B}_0$. At 1 Tesla,

there are about 3 excess spins per million. Even if our spin excess is very small, there is a vast number of protons (about 10^{21}) in a typical voxel volume in MRI which is of order of $2 \times 2 \times 2$ mm^3 . So the excess proton in a voxel volume is 3×10^{15} which is enough to produce an observable MRI signal.

In addition to energy separation of the spin states, the protons also experience a torque from the applied magnetic field, $\mathbf{B}_0$, that causes them to precess about $\mathbf{B}_0$. This is illustrated in Figure 2.2.1. This precession occurs at an angular frequency, ω_0, known as the Larmor frequency, which is proportional to the magnetic field strength B_0:

$$\omega_0 = \gamma B_0, \tag{2.2.3}$$

where γ is the gyromagnetic ratio unique to each element and B_0 is the magnetic field strength. $\mathbf{B}_0$ is aligned along the axis from head to toe, called the z-axis. For most clinical MRI scanners, $\mathbf{B}_0$ strength is about 1 - 3 Tesla, which is approximately 30,000 times stronger than the earth's magnetic field.

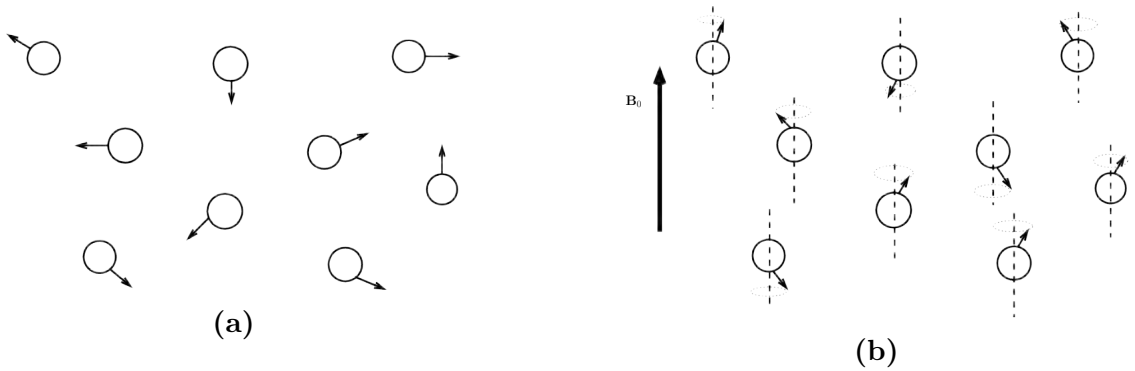

Figure 2.2.1: Illustration of the distribution of protons with and without an external magnetic field. **(a)** In the absence of an external magnetic field, a collection of protons assumes a random orientation of magnetic moments, producing a net magnetization of $\mathbf{M}$=0. **(b)** In the presence of a large homogeneous field, $\mathbf{B}_0$, the individual magnetic moments can assume any of the two possible orientations, spin up or spin down, and precess about $\mathbf{B}_0$.

In the presence of $\mathbf{B}_0$, the precessing spins are not in phase initially, and therefore the net magnetization $\mathbf{M}$ is constant and is essentially in the z direction without any xy (transverse) component. A changing magnetic field is required in order to get an MRI signal. Therefore the spins should be made to be in phase, thus producing a measurable vector component of $\mathbf{M}$ in the transverse plane. The RF transmit coil generates a time varying magnetic field, $\mathbf{B}_1$, weaker than the static $\mathbf{B}_0$, oscillating at the Larmor frequency ω_0 and applied perpendicular

to $\mathbf{B}_0$. At a quantum level, $\mathbf{B}_1$ gives the right amount of energy to some protons to transition from the low energy state to high energy state. Classically, the application of an oscillating $\mathbf{B}_1$ of frequency ω_0 causes all spins (whether initially aligned up or down) to precess around the $\mathbf{B}_1$ field, resulting in their rotation into a position on (or close to) the transverse plane. The vector sum of all the isochromats constitutes a net magnetization $\mathbf{M}$. To an observer in the *laboratory frame* of reference, $\mathbf{M}$ spirals towards the xy plane. If somehow the observer was riding along on $\mathbf{M}$, the laboratory would appear to be rotating. In this *rotating frame* of reference, $\mathbf{M}$ would appear to smoothly tip down. The tip (or flip) angle is a function of the strength and duration of $\mathbf{B}_1$. If $\mathbf{M}$ is tipped completely into the transverse plane, a 90° RF pulse is said to have been applied, while a 180° RF pulse will invert the magnetization.

After the RF pulse has been turned off, $\mathbf{M}$ will precess around the main $\mathbf{B}_0$ field at the Larmor precession frequency and induce a current in a receiver coil in the transverse plane (Figure 2.2.2). The signal decays over time due to both transverse and longitudinal relaxation processes, which are described in the next paragraphs. Importantly, the frequency of radiation given off by the still precessing protons is the Larmor frequency, so that even though the signal may not be extremely strong (as mentioned earlier, the excess is a very small ratio of the total number), the peak frequency of the emitted signal is predetermined, allowing stronger detection.

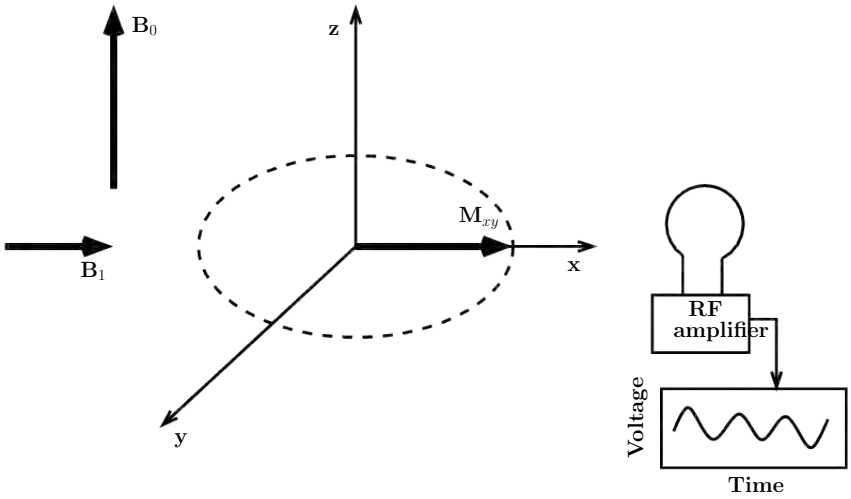

Figure 2.2.2: Precessing magnetization induces a signal in the coil.

T_1 relaxation, also called spin-lattice relaxation or longitudinal relaxation, is the process of recovery of the original longitudinal magnetization following a $\mathbf{B}_1$ perturbation. This happens when the protons slowly transfer the energy they absorbed, from the RF pulse, to their environment (historically called lattice because this process was first observed in crystals). T_1 is the time taken to recover 63% of the original longitudinal magnetization. T_1 relaxation is an

exponential process, as shown in Figure 2.2.3, described mathematically by,

$$M_z(t) = M_0(1 - e^{-t/\mathrm{T}_1}) \tag{2.2.4}$$

where M_0 is equilibrium magnetization and T_1 is the spin-lattice relaxation constant. T_1 depends on the molecular arrangement and structure of tissue, and therefore, it provides a useful source of contrast in neuroimaging.

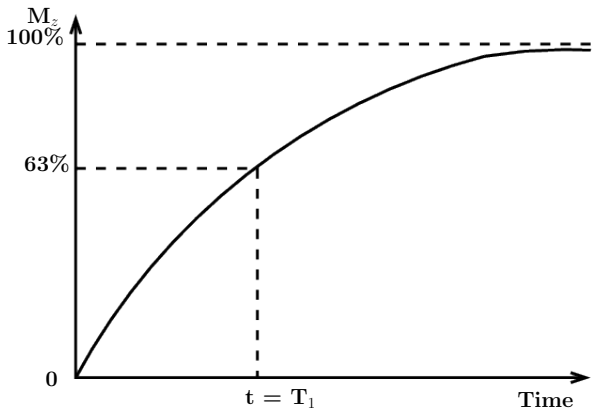

Figure 2.2.3: The return of M_z to equilibrium occurs exponentially after the RF pulse is turned off and it is characterized by the spin-lattice relaxation constant, T_1. At time t = T_1 after the 90° RF pulse, 63% of M_z is recovered.

The 90° RF pulse produces coherence in the spins thus maximizing M_{xy}. Following the $\mathbf{B}_1$ induction of in-phase precession, the spins begin to lose coherence and some precess at a faster rate than others. The result is that the transverse component of $\mathbf{M}$ decreases exponentially. This is known as transverse or spin-spin relaxation. T_2 is defined as the time it takes the transverse magnetization M_{xy} to decay by 63%. Mathematically, the relationship between T_2 and transverse magnetization recovery is given by,

$$M_{xy}(t) = M_{xy}(0)e^{-t/\mathrm{T}_2}, \tag{2.2.5}$$

where $M_{xy}(0)$ is the transverse magnetization instantaneously after pulse excitation. T_2 relaxation is caused by intrinsic spin-spin interactions in the tissues. In practice, the transverse magnetization decays much faster than would be predicted by the spin-spin interactions; this rate is denoted as $\mathrm{T}_2^\star$. $\mathrm{T}_2^\star$ characterises the rate at which the transverse magnetisation dephases due to both true spin-spin interactions (T_2) and extrinsic $\mathbf{B}_0$ magnetic field inhomogeneities (T_2') which may result from intrinsic defects in the magnet itself or from susceptibility-induced

field distortions produced by the magnetic materials in tissue (such as iron in red blood cells) or other materials placed within the field.

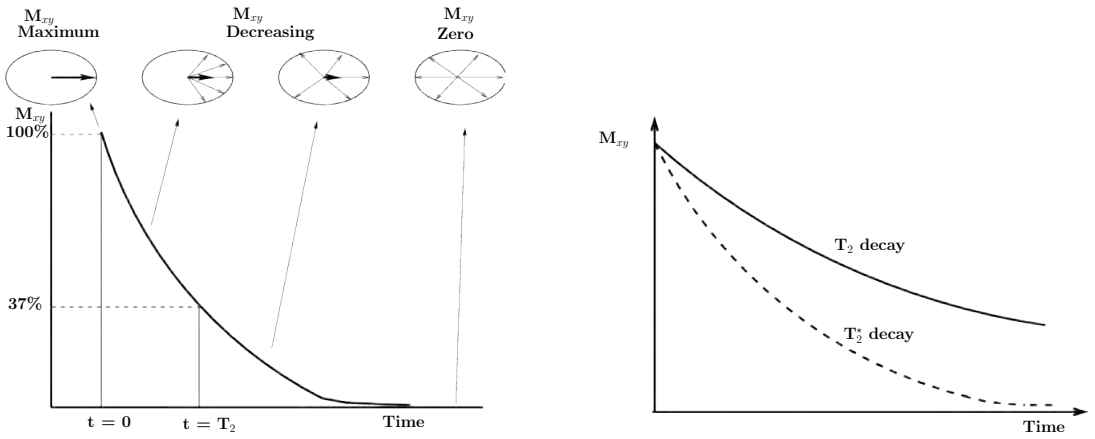

Figure 2.2.4: **(a)** The loss of the transverse signal occurs exponentially and is due to each proton's magnetic field interacting with its neighbours' magnet fields. At time T_2, M_{xy} is 37% of its original. **(b)** $T_2^\star$ is the decay time of the transverse magnetization resulting from both spin-spin interactions and extrinsic magnetic field variations.T_2 is always longer than $T_2^\star$.

2.2.2 Image contrast

The various tissues have different PD and relaxation times, therefore they end up with different MR signal intensities/brightness on MR images. PD is related to the number of hydrogen atoms in a particular volume. Tissues with high PD give higher signal intensities corresponding to brighter pixels on the image. Watery fluids such as CSF and blood have higher PD than tendon and bone. Relaxation times describe how long the tissue takes to get back to equilibrium after an RF pulse. T_1 and T_2 differ for different tissues (Table 2.2.2). In T_1-weighted images, long T_1 tissues give the weakest signal, i.e. bright pixels on T_1-weighted images are associated with short T_1 tissues. Fluids have long T_1 values (1500-1200 ms), water-based tissues are usually mid range (400-1200 ms), and fat-based tissues generally have short T_1 values (100-150 ms). In T_2-weighted images, tissues with long T_2 give the highest signal intensities, producing a bright appearance. Fluids have the longest T_2 (700-1200 ms), while water-based tissues tend to have longer T_2 values than fat-based tissue (40-200 ms and 10-100 ms respectively). T_1 and T_2 weighting are selected through the choice of machine parameters TR (repetition time) and TE (time to echo). TR refers to the time between successive applications of the RF pulse; TE refers to the time between RF excitation and signal readout. Shorter TR values (of the order of

500 ms) will increase the T_1-weighting in the image, while longer T_2 values (of the order of 100 ms) will increase T_2-weighting in the image. Long TRs and short TEs will result in minimal T_1 or T_2 weighting, so that images will be PD weighted.

Tissue	T_1 (ms)	T_2 (ms)
White matter	832	110
Grey matter	1331	80
CSF	3700	-
Muscle	898	29
Fat	382	68
Liver	809	34
Spleen	1328	61

Table 2.2.2: T_1 and T_2 values for human tissues at 3.0 tesla.

2.2.3 Signal localization

The protons in a tissue, when introduced to an external uniform magnetic field and RF energy of specific frequency, are excited and subsequently produce signal intensities that depend on the relaxation characteristics and spin density of the tissue, as previously discussed. Inside the magnetic bore reside 3 sets of spatial encoding coils to resolve spatial information in three dimensions. These coils produce magnetic fields that vary linearly along their axes. These linearly varying magnetic fields are called gradient fields, and the 3 sets of mutually orthogonal coils used that are used to produce them are called gradient coils.

The magnetic field gradients produced by the gradient coils typically vary the strength of $\mathbf{B}_0$ along a given spatial orientation, but does not alter its direction. MRI exploits the physical fact that the Larmor frequency (given by Equation 2.2.3) is directly proportional to the magnetic field, so that if the magnetic field varies across space, the precession frequency of the protons will vary as well. By turning on the magnetic field gradient, the protons at each position in the body experience a slightly different magnetic field, slightly more or less than $\mathbf{B}_0$. Thus we get a gradient of precession frequencies along that direction. We can therefore identify where a signal originated based on its precession frequency.

Selection of a particular slice requires the excitation of protons within that slice, with minimal excitement of other protons in the sample. During the application of the RF pulse, the slice-selective gradient (G_{SS}) is applied in a direction perpendicular to the desired slice, so that the frequency band of the RF pulse matches only that of the spins in the desired slice. Two

additional gradients are applied to obtain information about the distribution of atomic nuclei within the 2D slice itself. The phase encoding gradient (G_{PE}) is applied at right angles to G_{SS} and immediately after G_{SS} is turned off. While G_{PE} is applied, the spins precess at different rates depending on their position along the gradient. When it is turned off, the spins will revert to their original frequency but they would have lost phase coherence; the difference in phase will depend on their location in the slice. The phase difference will be embedded in the sampled MR signal. In order to acquire enough data to reconstruct an image, multiple phase encoding steps are needed, with the gradient strength being increased incrementally with each step. Each phase encoding step corresponds to a single measurement of the MR signal, i.e, a row of digitised values in k-space. The number of rows in k-space needs to match the number of rows in image space. The increment in gradient strength between successive phase encoding gradients is given by

$$\Delta G_{PE} = \frac{(G_{PE_{\max}} - G_{PE_{\min}})}{N_{steps} - 1} \tag{2.2.6}$$

where $G_{PE_{\max}}$ and $G_{PE_{\min}}$ are the maximum and minimum available gradients, respectively, and N_{steps} is the required number of phase encoding steps.

The frequency encoding gradient (G_{FE}), also known as the readout gradient because it is applied during data acquisition, localizes the MR signal in the second dimension of the 2D slice. G_{FE} is applied at right angles to both G_{SS} and G_{PE}. The detected MR signal is a sum of component signals, each of which has a different frequency, from different locations in the slice. Since the G_{FE} is on while the MR signal is sampled, the spatial information is embeded in the signal.

2.2.4 MRI scan parameters

The choice of acquisition parameters affects the tissue contrast, image spatial characteristics, image noise characteristics and total scan time. As already explained, the choice of TR and TE affects the image tissue contrast and leads to possibility of acquiring T_1- and T_2-weighted images.

The dimensions of the desired part of the body to be scanned, also known as the field of view (FOV), are specified by the operator. The FOV in a particular direction is related to the

bandwidth of the RF excitation pulse and the applied gradient strength G in that direction. For example, we can mathematically represent the FOV in the phase encoding direction as follows:

$$FOV_{PE} = \frac{\text{bandwidth}}{\gamma G_{PE}}. \tag{2.2.7}$$

The spatial resolution (or voxel size) is the minimum distance that can be distinguished between two points on an image. It is given by

$$\text{voxel size} = \frac{FOV_{PE}}{N_{PE}} \times \frac{FOV_{FE}}{N_{FE}} \times \text{slice thickness}. \tag{2.2.8}$$

where N_{PE} and N_{FE} are the number of pixels in the phase encoding direction and the frequency encoding direction, respectively and are determined by the image matrix size.

The signal to noise ratio (SNR) is the measure of the relative strengths of the signal and the unwanted noise . A very low SNR corresponds to having a signal that cannot be distinguished from the background noise, and this results in poor quality images. SNR is related to the voxel size, the receiver RF bandwidth, N_{PE} and the number of excitations (NEX), also referred to as the number of acquisitions/averages, by

$$SNR \propto \text{voxel volume} \times \frac{\sqrt{N_{PE} \times NEX}}{\sqrt{\text{bandwidth}}}. \tag{2.2.9}$$

Although the equation above shows only three parameters, there are several factors that affect SNR including RF coil quality, B_0, inter-slice gap effects, reconstruction algorithms, etc.

The total image acquisition time or scan time is given by

$$\text{Scan time} = TR \times N_{PE} \times NEX. \tag{2.2.10}$$

Unfortunately, optimization of image scan parameters involves some trade-offs. Gaining advantage with one parameter usually requires sacrificing another parameter. For example, increasing the FOV, thus increasing the bandwidth, will decrease the SNR. Another example is increasing the spatial resolution (decreasing voxel size) results in reduced SNR.

2.2.5 Signal processing

MRI uses a quadrature (or circularly polarized) coil system comprised of two coil pairs which are offset 90° with respect to one another, and therefore the MR signal received by these are 90 degrees out of phase. One coil detects the in-phase, or 'real', signal. One coil detects the quadrature, or 'imaginary', signal. The purpose of quadrature detection is to increase SNR by a factor of $\sqrt{2}$. The quadrature coil can generate four types of images: real, imaginary, magnitude and phase images.

After each RF excitation, a measurement is acquired. The phase encoding gradient increases incrementally for successive measurements, while the frequency encoding gradient strength remains unchanged. Each signal is sampled, with at least two samples per cycle as dictated by the Nyquist sampling theorem, and stored in a row of a 2D data matrix usually referred to as the frequency domain representation or k-space [Figure 2.2.5]. Therefore, k-space comprises a matrix of complex data (i.e., real and imaginary) that fully describes the evolution of the transverse magnetization over time after application of different phase encoding gradients and in the presence of a frequency encode gradient. Each row therefore contains the digitised signal following application of a different phase encode gradient. The matrix is converted into an MR image by performing a two dimensional Fourier transform that maps the intensity of each spatial frequency onto the image.

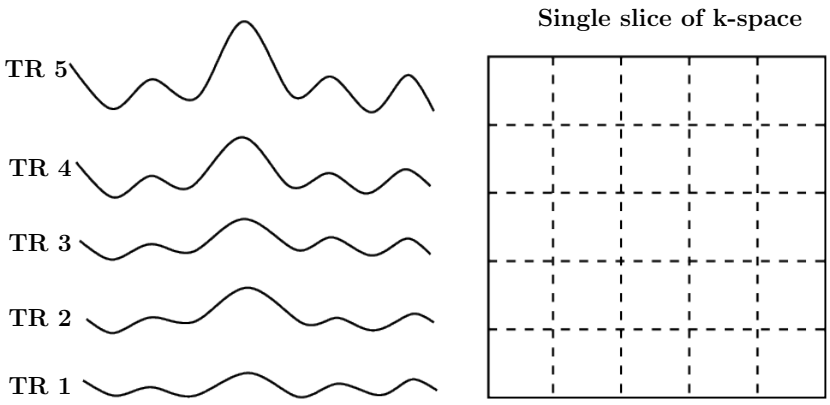

Figure 2.2.5: Illustration of k-space data matrix. Each acquired slice has its own 2D k-space. Digitized values sampled from the signal are what are stored in the each row of k-space.

2.2.6 Pulse sequence

MRI involves application of magnetic fields and field gradients at specific times to generate an image. The static magnetic field $\mathbf{B}_0$ is constantly present. The RF pulse and the gradient

magnetic fields are not. They are applied in a controlled pattern through software known as an MR pulse sequence. All MR images are produced using a pulse sequence which is stored in the scanner computer. The sequence contains all information as to the amplitude, shape, timing and duration of radio frequency and gradient pulses. There are many different types of sequences, but they all have repetition time (TR) and echo time (TE) that can be modified. Usually the operator sets TR and TE in order to get the desired tissue contrast. For example, in order to get a T_1 weighted image, both TR and TE must be short. T_2 weighting is achieved by making both TR and TE long. The two most widely used pulse sequences are the gradient echo and the spin echo sequences.

Gradient echo (GE)

Figure 2.2.6 summarizes the timing of the different components in the gradient echo pulse sequence. The diagram consists of five rows, each showing a specific event that occurs during MR imaging. The RF excitation pulse and the G_{SS} are applied simultaneously, followed by G_{PE}, and finally G_{FE} which is applied during signal acquisition. After the G_{SS} is applied, a gradient in the opposite direction is applied in order to refocus the spins that lost transverse phase coherence during the application of the G_{SS}. Basically, every time a gradient is applied, the spins dephase and this could destroy the MR signal. The G_{SS} is applied to select an image slice, but this also causes the transverse components of the spins in the slice to become dephased. Any dephasing that occurred due to this gradient is reversed by the opposite rephasing gradient. The sequence is repeated every TR with an increment in the strength of the phase encoding gradient. Prior to the application of the readout gradient, a negative dephasing gradient, which has half the area under the curve of the readout gradient, is applied. The negative gradient causes the spins to dephase. The spins get back in phase in the center of the readout period, i.e., at time TE.

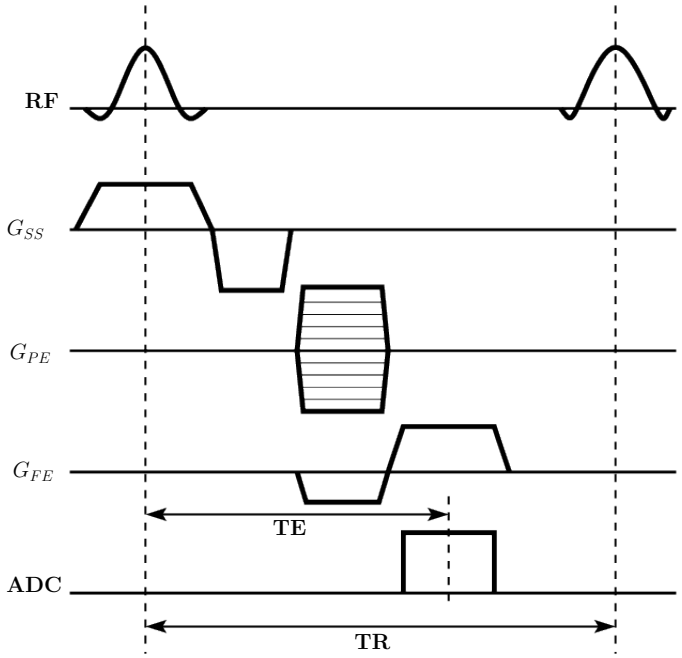

Figure 2.2.6: Simplified gradient echo pulse sequence diagram indicating the timing of G_{SS}, G_{PE} and G_{FE}, including the reversal of G_{FE}, synchronized with RF excitation and data acquisition. After a time interval TR, the sequence is repeated with a different G_{PE} strength (this is represented as a series of parrallel lines in the diagram). G_{SS}=slice select gradient, G_{PE}=phase encode gradient, G_{FE}=readout gradient, RF=radiofrequency pulse, ADC=analog-to-digital conversion, TE=time to echo, TR=repetition time.

Spin echo sequence

The timing diagram of a spin echo sequence is illustrated in Figure 2.2.7. The spin echo sequence refocuses the spin dephasing caused by T_2' dephasing by the application of a 180° RF refocusing pulse exactly halfway between the 90° excitation pulse and the centre of the echo (i.e., at a time equal to TE/2). The 180° pulse may be slice selective (i.e., have a G_{SS} applied simultaneously) or non-slice selective.

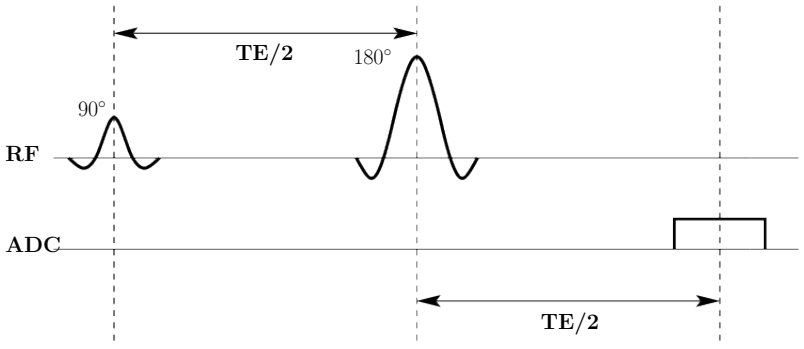

Figure 2.2.7: A spin echo pulse sequence includes a slice selective 90° RF pulse followed by a one or more 180° refocusing pulses. The spins will be back in phase at time TE.

In comparison to GE sequences, the SE sequences have higher SNR and minimal image artefact. The major disadvantage of SE sequences are the relatively long TRs required for signal relaxation due to the 90-180 degree RF pair, while GE sequences can use smaller flip angles, requiring shorter relaxation times and are therefore faster to acquire.

Echo-planar imaging

Fast techniques such as echo-planar imaging (EPI) (Mansfield, 1977; Rzedzian et al., 1983) have been introduced in order to shorten the MR acquisition times. EPI provides adequate resolution (3 mm or better) in a short time (20-100 ms per slice). Therefore, imaging of rapidly changing physiological processes has become possible.

Whereas one line of k-space is acquired each TR in a conventional MR pulse sequence, many lines of k-space are acquired from each excitation pulse are in EPI. As such, a complete (albeit low resolution) image can be acquired after a single RF excitation.

A timing diagram for a blipped spin echo echo-planar imaging (SE EPI) sequence is shown in Figure 2.2.8. Like a conventional SE sequence, an SE EPI sequence begins with the 90° and 180° RF pulses. However, after the 180° RF pulse, the G_{FE} oscillates rapidly between a positive and a negative gradient, forming a train of gradient echoes. Each oscillation of G_{FE} corresponds to a line in k-space. A small G_{PE} gradient (called a blip) is placed at each G_{FE} reversal essentially stepping up (or down) between successive rows in k-space.

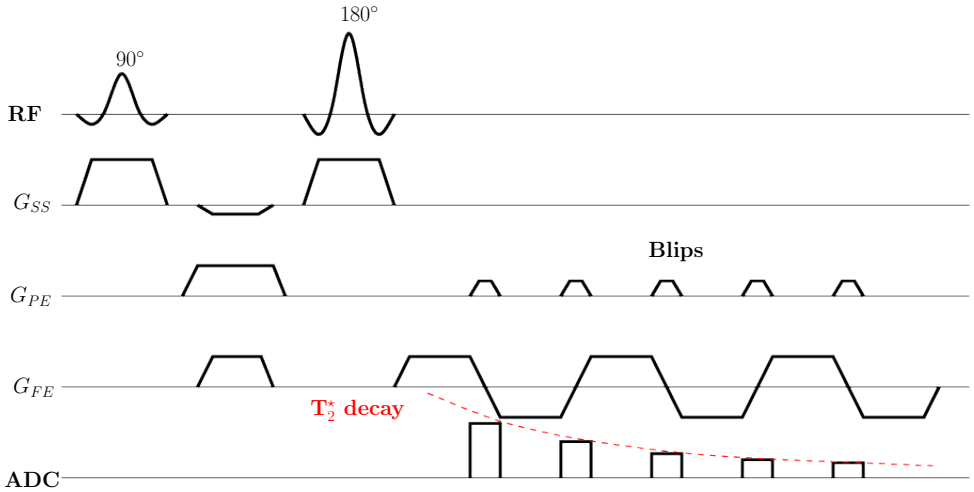

Figure 2.2.8: Spin echo echo-planar imaging. In EPI, multiple lines in k-space are acquired following a single excitation. In a blipped EPI sequence, a small phase encoding gradient (or a blip) is placed at each gradient reversal.

EPI images are prone to artefacts such as chemical shift and N/2 ghost artefacts. Therefore,

application of fat suppression and phase correction techniques is important in EPI.

Fat suppression

All hydrogen nuclei in the part of the body being imaged contribute to the MR signal. However, for many of these nuclei (e.g., hydrogen nuclei on fatty acid chains in cell membranes), their signal decays too quickly to contribute to the measured signal. The measured MR signal is mainly composed of contributions from hydrogen nuclei residing on water molecules and fat molecules in adipose tissue. In many situations in clinical MRI, it is desirable to suppress the signal from fat molecules in normal adipose tissue when the fat signal causes artefacts or obscures a tissue of interest. This is achieved by inserting a fat suppression module at the beginning of an MRI pulse sequence. A number of fat suppression techniques have been developed which exploit one or all of the following properties: 1) differences in relaxation times between fat and water (e.g., the short tau inversion recovery (STIR) technique (Bydder et al., 1998)) and 2) differences in resonance frequencies between fat and water (e.g., chemical shift selective (CHESS) technique (Haase et al., 1985)).

Phase correction

The N/2 ghost artefact occurs because of cumulative phase differences between odd and even echoes over the echo train caused mainly by the induction of eddy currents in coils in response to rapidly changing gradient pulses. Phase correction can be achieved from a reference scan without the phase encoding gradient. A phase correction pulse is usually included in most commercial EPI sequences to minimize N/2 ghosting.

2.2.7 Flexibility of MRI

The wide range of MRI contrast mechanisms is what makes MRI the most flexible and powerful tool in imaging. By careful choice of pulse sequence timing parameters (e.g., TR and TE), different characteristics of tissues being imaged can be highlighted (e.g., proton density, T_1 and T_2). The MR signal can be sensitized to several other physiological parameters that carry MRI beyond anatomical imaging, making way for fMRI and diffusion MRI. It is worth noting that the physical effects that underlie fMRI and diffusion MRI techniques (i.e., magnetic field inhomogeneities and sensitivity to motion respectively) first appeared as artefacts in conventional

anatomical MRI.

2.3 Functional magnetic resonance imaging

Functional magnetic resonance imaging (fMRI) has become the most commonly used method to study functional organisation of the human brain. It is a powerful tool in defining functional activity in both healthy and diseased brains. FMRI provides an unprecedented ability to safely and noninvasively image brain activity with both a reasonable spatial resolution and a relatively good temporal resolution, as compared to previous methods such as positron emission tomography (PET). The rush of blood to the activated areas of the brain is the physiological basis for fMRI. Several statistical software packages are available for processing and analysis of fMRI data, several of which are freely available.

2.3.1 Brain activation and physiological changes

As is true for all organs in the body, the brain requires energy for basic cellular processes, and it requires a great deal of additional energy for its primary function of neuronal signalling. The brain has virtually no reserve store of oxygen and glucose. The glucose and oxygen required for energy metabolism are continuously supplied by the vascular system. Brain function can then be mapped based on energy delivery by the blood supply. This is the basis of most functional neuroimaging techniques, including fMRI.

The physiological changes that accompany neuronal activation are not fully understood, and this is a subject of ongoing research. The evidence to date suggests that during brain activation, cerebral blood flow (CBF), cerebral metabolic rate of glucose (CMRGlc) and cerebral metabolic rate of oxygen ($CMRO_2$) increase locally. While CBF and CMRGlc remain coupled during functional activity (Madsen et al., 1995; Newberg et al., 2005; Paulson et al., 2010), $CMRO_2$ increases only by a minor degree (Fox and Raichle, 1986; Fox et al., 1988). Fox and Raichle (1986) conducted a series of PET experiments on human subjects in which they measured CBF, CMRGlc and $CMRO_2$ in the absence of brain stimulation and during visual stimulation. They found that during prolonged visual stimulation, CBF in the visual cortex increased by 50% and CMRGlc increased by 51%. However, $CMRO_2$ increased by only 5%. Most researchers have come to accept that their results indicate that most of the increase in the metabolic rate

of glucose is anaerobic glycolysis and not full oxidative metabolism. This finding has been confirmed with direct measurements of brain lactate concentration during activation (Frahm et al., 1996; Prichard et al., 1991; Sappey-Marinier et al., 1992).

2.3.2 Blood oxygenation level dependent (BOLD) response

During neural activation, cerebral oxygen consumption does not increase to the same extent as does CBF and CMRglc, an important physiological phenomenon commonly referred to as the *uncoupling of flow and oxidative metabolism* during functional activation. An imbalance between oxygen consumption and oxygen supply exists, resulting in an increase in the ratio of oxy- to deoxy-haemoglobin in the region of neuronal activation. Haemoglobin carrying oxygen (oxyHb) and deoxygenated haemoglobin (deoxyHb) have different magnetic properties. DeoxyHb is slightly paramagnetic (i.e., it has unpaired electrons and a significant magnetic moment) relative to brain tissue, whereas oxyHb is diamagnetic (i.e., it has no unpaired electrons and zero magnetic moment) (Pauling and Coryell, 1936). Vessels containing oxygenated arterial blood thus cause little or no distortion to the magnetic field in the surrounding tissue, while capillaries and veins containing blood that is partially deoxygenated distort the magnetic field in their vicinity (Ogawa et al., 1990a). The microscopic field inhomogeneities associated with the presence of deoxyHb lead to destructive interference from signal within the tissue voxel, a process that tends to shorten the $T_2^\star$ relaxation time. Thus, as oxygen extraction falls with enhanced local blood flow in a region of greater neuronal activity, the $T_2^\star$ becomes longer and the MRI signal intensity increases relative to the baseline state. The change in the MR signal triggered by neuronal activity is known as the hemodynamic response and is illustrated in Figure 2.3.1 for an extended neuronal stimulation/activity.

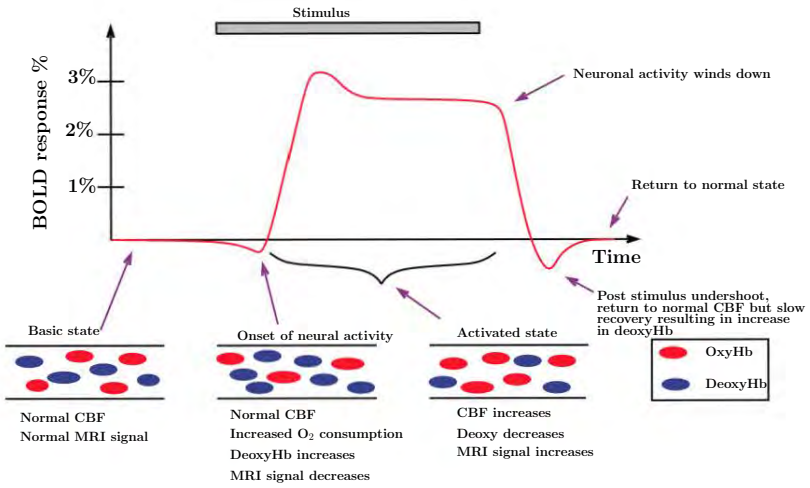

Figure 2.3.1: Schematic diagram showing the hemodynamic response during an interval of neuronal activation. A stimulus is any task the fMRI experimenters set up for the subject to do in the MRI scanner to activate the neuronal activity they are looking for. When a stimulus is applied, CBF increases significantly relative to oxygen consumption. This results in lower concentration of deoxyHb in the local blood vessels and hence a reduction in microscopic field gradients and an overall increase in the MR signal intensity.

The signal measured in fMRI depends on the change in local blood oxygenation and is referred to as the blood oxygenation level dependent (BOLD) response. The magnitude of the BOLD response increases with the square of the strength of the $\mathbf{B}_0$ field (Thulborn et al., 1982). At low field strength (i.e., less than 1.5 T) there is little difference between the tranverse relaxation values for oxygenated and deoxygenated blood. So strong magnetic fields ($\gtrsim$ 1.5 T) are necessary for MR imaging of $T_2^\star$ weighted contrast in blood (Ogawa et al., 1990b, 1993; Thulborn et al., 1982).

2.3.3 BOLD acquisition

The majority of BOLD fMRI studies routinely use multislice 2D EPI for whole brain imaging. Multislice 2D EPI is one of the many variants of EPI. In this technique, one slice is selectively excited and acquired separately at a time. A volume is imaged by simply imaging many slices in succession. The multiple slices can be acquired sequentially or in an interleaved fashion.

The entire brain volume can also be imaged using 3D EPI. In this method, the slice selective gradient is eliminated so that the entire brain is excited. Spatial information in the third dimension (z) is then encoded by phase encoding that axis in addition to the other phase encoding direction (y). For each phase encoding step in y, the full range of phase encoding steps in z must be collected.

3D EPI provides multiple benefits over multislice 2D EPI such as a higher sensitivity per unit scan time (Hu and Glover, 2007; Lai and Glover, 1998), the absence of a spin history artifact (Muftuler and Nalcioglu, 2000), and a higher SNR is reached in 3D EPI than in multislice 2D EPI even though smaller flip angles are typically used (Goerke et al., 2005). Additionally, it has been shown that 3D EPI is comparable to 2D EPI for detecting functional activation (van der Kouwe et al., 2006).

2.3.4 Task based fMRI

In *task-based* fMRI, while lying in an MRI scanner, a subject alternates between periods of performing a particular task, such as finger tapping, looking at pictures or answering questions on a computer screen, and a control state (in which the task is absent or at a lower level), while the change in BOLD signal in the brain is measured by acquiring a series of brain images with contrast weighted by $T_2^\star$.

2.3.5 Resting state fMRI

The brain consists of specialized spatially distributed regions for various cognitive functions such as processing of sensory stimuli, memory and movement. Studies have shown that even during rest, the brain is not idle but shows a vast amount of spontaneous activity that is highly correlated between brain regions (Biswal et al., 1995). Studies have shown the feasibility of examining functional connectivity between brain regions by examining the level of temporal correlation between their functional time-series using resting state fMRI (Biswal et al., 1995; Damoiseaux et al., 2006; Salvador et al., 2005).

During resting state fMRI (rs-fMRI) experiments, subjects lie in the MRI scanner, without an explicit stimulus or task, and are instructed to relax and not to think about anything in particular while their spontaneous BOLD activity is measured throughout the experiment. The resting state fMRI time series of a voxel is then correlated with that of the other voxels in the brain. Regions of the brain whose time series are highly correlated form resting state networks (RSNs). The synchronization of the spontaneous resting state activity in the brain is typically observed in the low frequency (∼0.01-0.1 Hz) BOLD fMRI signals (Cordes et al., 2001).

Most RSNs tend to show similar spatial extent to known functional networks, e.g., the primary visual network, the auditory network, the sensory motor network and higher order cognitive

networks (Biswal et al., 1997; Damoiseaux et al., 2006), supporting the functional relevance and interpretation of these networks. Of additional interest is the default mode network (DMN) which consists of functionally linked posterior cingulate cortex, medial frontal and inferior parietal regions. In contrast to the other RSNs, the regions of the DMN are known to show a synchronized, elevated level of neuronal activity only during rest (Greicius et al., 2003; Raichle et al., 2001; Raichle and Snyder, 2007).

2.3.6 Applications of resting state fMRI

Rs-fMRI offers several advantages to task-based fMRI in clinical applications. With rs-fMRI, many networks can be identified simultaneously, thus saving scanning time if information from multiple networks is required. Additionally, rs-fMRI is less demanding and can be performed on patients who may not otherwise be able to cooperate with task based paradigms, such as young children, patients with cognitive dysfunction or physical impairment and sedated patients (Liu et al., 2009; Shimony et al., 2009), especially because BOLD activity seen in rs-fMRI has also been seen during sleep and anaesthesia (Fukunaga et al., 2006).

Rs-fMRI has provided many interesting insights on functional networks in neurological and psychiatric diseases (Zhang and Raichle, 2010). Several recent studies have demonstrated that patterns of RSNs are significantly different between individuals with and without neuropathologic conditions. For example, abnormal functional connectivity patterns have been seen in patients with dementia (Greicius et al., 2004; Wu et al., 2011), epilepsy (Liao et al., 2011; Luo et al., 2011), autism (Cherkassky et al., 2006; Kennedy and Courchesne, 2008) and schizophrenia (Liang et al., 2006; Skudlarski et al., 2010).

One area in which fMRI has shown great promise is in preoperative functional mapping to help guide neurosurgical planning (Hå berg et al., 2004; Vlieger et al., 2004). Preoperative functional mapping is most often used to identify brain areas used in movement and language so that these areas can be avoided during surgical resection. However, patients may lack the ability to perform tasks well. As already mentioned, the advantages of rs-fMRI may circumvent many of the current limitations hindering task-based pre-operative mapping. Indeed several articles have recently been published showing the potential of rs-fMRI as a pre-operative mapping tool in patients with neurosurgical conditions (Liu et al., 2009; Shimony et al., 2009; Zhang et al., 2009).

2.3.7 The structural core of resting state functional connectivity

As mentioned previously, RSNs consist of spatially distinct brain regions that are functionally connected. RSNs thus reflect ongoing neuronal activity and communication between brain regions. Their functional connectivity is facilitated by bundles of white matter axons that interconnect large groups of spatially separated neurons. White matter tracts are the information highways of the brain, enabling transport of large amounts of functional data between spatially separated regions.

Recently, a number of studies have indeed suggested a direct association between functional and structural connectivity in the human brain by combining rs-fMRI with structural diffusion tensor imaging measurements (DTI). For example, Greicius et al. (Greicius et al., 2009) demonstrated the existence of white matter pathways interconnecting the different regions of the functional DMN. Another study showed that well known structural white matter tracts interconnect at least eight of the nine commonly found RSNs (van den Heuvel et al., 2009). Taken together, these and several other studies (Hagmann et al., 2008, 2007; Johnston et al., 2008; Koch et al., 2002) suggest the existence of a general structural core for resting state networks. In the next section, DTI is described in detail.

2.4 Diffusion tensor imaging

Diffusion weighted imaging (DWI) (Merboldt et al., 1985; Taylor and Bushell, 1985) is able to measure the loss of MR signal that arises from the random thermal motion of water molecules within a voxel of an image. DTI is a specific type of modelling of DW images that uses the diffusion tensor model to indirectly measure the local direction of water diffusion which corresponds to the structural orientation of large white matter pathways (Basser et al., 1994b; Pierpaoli et al., 1996). DTI has gained popularity among clinicians because it is noninvasive and uses existing MRI technology without requiring new equipment.

2.4.1 The nature of diffusion

Water molecules in the body are always in constant random thermal motion, colliding with other molecules. The molecules colliding with each other undergo small random displacements that are measurable with MRI.

The essential nature of diffusion is that a molecule in a homogeneous medium that starts out at a location has an equal probability of being on a centred spherical surface of radius r after a time t and satisfies Einstein's relation (Einstein, 1956),

$$6t = D^{-1}r^2, \tag{2.4.1}$$

where D is the diffusion coefficient. In biological structures, the diffusion of water molecules is restricted by natural barriers such as cell membranes and large protein molecules (Cooper et al., 1974). In such cases of restricted diffusion, the Einstein relation is generalized to allow for directional dependence:

$$6t = \mathbf{r}^T\mathbf{D}^{-1}\mathbf{r}, \tag{2.4.2}$$

where $\mathbf{r}$ is the displacement vector and $\mathbf{D}$ is the second order tensor which gives the diffusion coefficient in each direction. The diffusion tensor is further described in Section 2.4.3.

2.4.2 Diffusion weighted image acquisition

The MR signal can be made sensitive to the motion of water molecules by inclusion of a bipolar magnetic field gradient pulse in the MR pulse sequence. For example, the diffusion gradient pulses shown in Figure 2.4.1 would be directly inserted into the gradient echo pulse sequence in Figure 2.2.6.

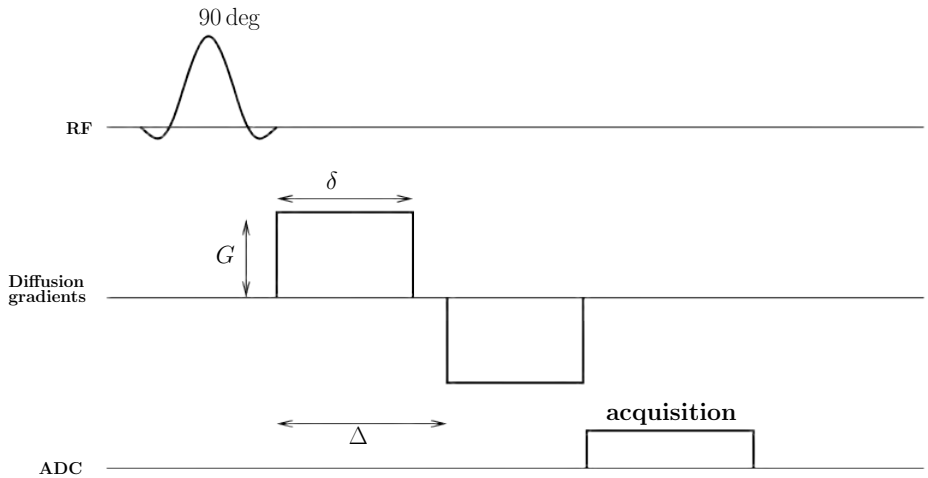

Figure 2.4.1: The MRI signal is made sensitive to diffusion by applying a bipolar gradient pulse between the signal excitation and signal detection. The axis of diffusion sensitizing gradients is arbitrary and can be adjusted by the experimenter.

The first diffusion gradient pulse acts to alter the phase shift of each proton by an amount that depends on the proton's spatial location along the gradient axis. This gradient is also called the dephasing gradient. The second gradient (applied with the same strength and duration as the first, but in the opposite direction) acts to reverse the phase shift of the protons. It is called the rephasing gradient. The rephasing is never perfect as some protons will have changed position. Only the protons that did not move between the application of the first and the second diffusion gradient pulses will be completely rephased. For the protons that moved, complete rephasing cannot happen, resulting in signal loss from this spatial location. The amount of signal loss in a voxel is given by the Stejskal-Tanner equation (Stejskal and Tanner, 1965):

$$\frac{S}{S_0} = \exp(-\gamma G^2 \delta^2 (\Delta - \frac{\delta}{3}) D), \tag{2.4.3}$$

where S is the DW signal, S_0 is the signal without any diffusion weighting (but with identical imaging parameters to S), γ is the gyromagnetic ratio, G is the diffusion gradient field strength, δ is the duration of each gradient application, Δ is the time interval between the application of the diffusion gradient pulses and D is the apparent diffusion coefficient along the gradient direction used, and will be described in more detail in the next section. The Stejskal-Tanner equation can be rewritten as

$$\frac{S}{S_0} = \exp(-bD) \tag{2.4.4}$$

where, we define the DW factor b as:

$$b = -\gamma G^2 \delta^2 (\Delta - \frac{\delta}{3}). \tag{2.4.5}$$

The parameter b, called the b-factor, describes the properties of the diffusion gradient pulse pair and essentially indicates how heavily the sequence is diffusion weighted, i.e., how much signal contrast will be affected by diffusion. In many DTI scans, typical estimate of the b-factor lie in the range 1000 s mm^{-2} - 2000 s mm^{-2} (Clark and Le Bihan, 2000; Jones, 2004; Le Bihan et al., 2001; Mulkern et al., 1999; Taylor and Biswal, 2011).

The diffusion gradients used to sensitize the MR signal to the self diffusion of water molecules are strong enough to cause eddy currents to be induced in the conducting structures around the gradient coils according to *Faraday's induction law*. The eddy currents produce geometric

distortions in the DW images. To minimize eddy current distortions and consequently improve image quality, several DWI methods have been proposed (Alexander et al., 1997; Boesch et al., 1991; Heid, 2000; Reese et al., 1998). The twice-refocussed spin echo (TRSE) pulse sequence (Reese et al., 2003) is another method that successfully reduces the cumulative eddy current effect by adjusting the timings of the gradient lobes (Figure 2.4.2), at the expense of increased TE.

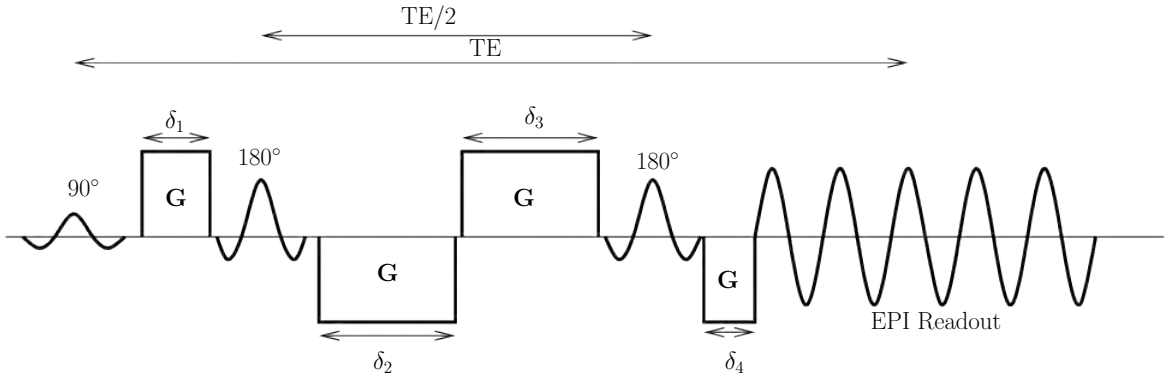

Figure 2.4.2: Timing diagram of the TRSE sequence. The 90° and the two 180° RF pulses excite and refocus the spins, respectively. The diffusion gradients **G** of lengths δ_1, δ_2, δ_3 and δ_4 are also shown. The data is acquired using an EPI readout. Other sequence elements were omitted for clarity. The sequence allows any diffusion gradient lengths such that the time between the first and the second 180° refocussing RF pulses is TE/2, and the dephasing and rephasing due to the diffusion gradients are equal.

2.4.3 The diffusion tensor model

In an anisotropic medium, the measured diffusion coefficient may be different along each different directions. Therefore, instead of being characterized by a single number, the full diffusion in three dimensions is described by a 3×3 matrix of numbers, $\boldsymbol{D}$. In a DTI experiment, if a diffusion sensitizing gradient pulse is $\mathbf{g}=\{g_x, g_y, g_z\}$, where $\mathbf{g}$ is a unit vector, then the measured value of D is given by (Hsu and Mori, 1995)

$$D = \begin{pmatrix} g_x & g_y & g_z \end{pmatrix} \begin{pmatrix} D_{xx} & D_{xy} & D_{xz} \\ D_{yx} & D_{yy} & D_{yz} \\ D_{zx} & D_{zy} & D_{zz} \end{pmatrix} \begin{pmatrix} g_x \\ g_y \\ g_z \end{pmatrix}. \tag{2.4.6}$$

We shall use the superscript T to indicate the transpose and write

$$D = \mathbf{g}^T \mathbf{D} \mathbf{g}. \tag{2.4.7}$$

The elements of $\mathbf{D}$ depend on the coordinate system used (i.e., measurements are done in the coordinate system defined by the imager gradients). One must find the coordinate transformation that produces a diagonal matrix by applying a mathematical operation known as *diagonalization*. The result is a set of three values along the main diagonal, known as eigenvalues and usually represented in decreasing order as λ_1, λ_2 and λ_3. The directions of the coordinate axes of the tensor coordinate system are called eigenvectors, usually symbolized as $\mathbf{e}_1$, $\mathbf{e}_2$ and $\mathbf{e}_3$. The largest eigenvalue (λ_1) corresponds to the value of maximum diffusion and the corresponding eigenvector ($\mathbf{e}_1$) for this maximum eigenvalue points to the direction of maximum diffusion and is typically used to indicate the orientation of structures in an imaging voxel.

Approximations are made by assuming $\mathbf{D}$ is real, symmetric (i.e., $D_{ij} = D_{ji}$ with $i, j = x, y, z$) and positive definite. Due to its symmetry, $\mathbf{D}$ has six independent quantities: the elements down the diagonal, and the three elements in one corner. One common approach to measuring $\mathbf{D}$ is to acquire one image with $b = 0$, for reference, and six images with $b = 1000$ s/mm^2 but with diffusion gradient orientations spread out in space to avoid repeating the same measurements. In research applications and in clinical settings, more than six diffusion diffusion encoding gradients are used to have error reduction in fitting of the tensor (Jones, 2004); for example, 30 is standard in research.

Geometrically, a matrix with the mathematical properties of $\mathbf{D}$, (i.e. real, symmetric and positive definite) can be viewed as an ellipsoid. The eigenvalues describe the shape of the ellipsoid while the eigenvector express the orientation of the ellipsoid. The equation of an origin-centred ellipse of arbitrary size and orientation is

$$\frac{x^2}{a^2} + \frac{y^2}{b^2} + \frac{z^2}{c^2} = 0, \tag{2.4.8}$$

where a, b and c are the hemiaxes lengths. The equation of the diffusion ellipsoid (Figure 2.4.3) can be written as

$$\frac{x^2}{2\lambda_1 T} + \frac{y^2}{2\lambda_2 T} + \frac{z^2}{2\lambda_3 T} = 0, \tag{2.4.9}$$

where λ_i, $\{i = 1, 2, 3\}$ are eigenvalues computed from the diagonalization of $\mathbf{D}$.

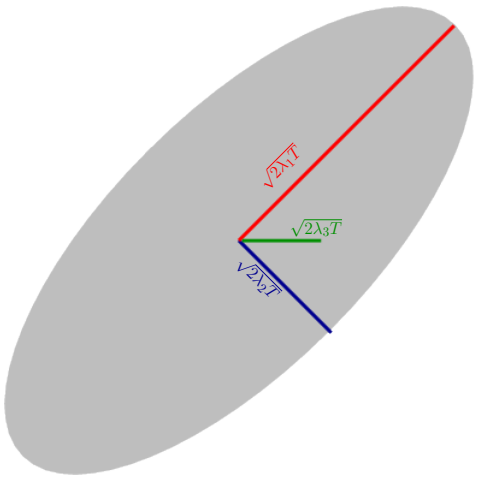

Figure 2.4.3: The diffusion tensor is usefully visualized as an ellipsoid due to its mathematical properties. As in the case with the isotropic diffusion sphere, the anisotropic diffusion ellipsoid represents the mean squared displacement in each direction, in this case differing along various directions.

Two useful scalar measures that can be extracted from the diffusion tensor are the mean diffusivity (MD) and the fractional anisotropy (FA). The MD describes the average amount of diffusion. It is simply the average of the principal diffusivities and represents the isotropic part of the diffusion tensor. MD is given by

$$\text{MD} = \frac{\lambda_1 + \lambda_2 + \lambda_3}{3} = \frac{\text{Trace}(\mathbf{D})}{3}. \tag{2.4.10}$$

The FA value is the normalised standard deviation of the eigenvalues, taking values between 0, for isotropic diffusion, and 1, for completely anisotropic diffusion. The FA is defined mathematically as

$$\text{FA} = \sqrt{\frac{3((\lambda_1 - MD)^2 + (\lambda_2 - MD)^2 + (\lambda_3 - MD)^2)}{2(\lambda_1^2 + \lambda_2^2 + \lambda_3^2)}}. \tag{2.4.11}$$

Both the MD and FA are rotationally invariant indices and allow orientation-independent comparisons of diffusion indices between different subjects (Le Bihan et al., 2001).

2.4.4 Applications of DTI

In clinical studies and applications of DTI, suitable parameters extracted from the diffusion tensor are compared between groups or between healthy and diseased brain. The MD and

FA can be used to characterize microstructural properties and integrity of brain tissue, and have proved to be useful in studying and revealing early changes in many neurological diseases (Sundgren et al., 2004). Abnormal MD and FA values have been observed in various disorders such as multiple sclerosis (Filippi et al., 2001; Guo et al., 2002b; Horsfield et al., 1996), ischemia (Sorensen et al., 1999; Thomalla et al., 2004), epilepsy (Tessa et al., 2007), and Alzheimer's disease (Bozzali et al., 2002). DTI has also been used to study human brain development, maturation and ageing, and the values of MD and FA have been shown to vary with age (Morriss et al., 1999; Mukherjee and McKinstry, 2006; Mukherjee et al., 2001; Pfefferbaum et al., 2000). Although conventional MRI can be used to demonstrate the site extent of a brain tumour, its specification and grading of tumours is limited. DTI has shown the potential to differentiate tumour invasion from normal brain tissue or edema. DTI has also been able to determine the type and grade of tumours (Kono et al., 2001) and to provide information about tumour response to therapy (Chenevert et al., 1997, 2000; Mardor et al., 2003).

A popular application of DTI is tractography (Conturo et al., 1999). The directional information contained in the diffusion tensor allows for determination of the orientation of white matter tracts in each voxel. Once the orientation of fibers at every point in the brain is known, these directions can be integrated to estimate entire pathways and hence brain connections. The process of creating 3D reconstructions of white matter is known as tractography. DTI tractography has increased our understanding of brain structure, physiology and pathology (Johnston et al., 2008). Additionally, tractography has been used in conjunction with fMRI, to establish connectivity pathways for a variety of functional networks, thus increasing our understanding of brain connectivity (Hagmann et al., 2008, 2007; Johnston et al., 2008). This has been especially useful in presurgical planning, where motor and language brain regions are to be avoided during resectioning of lesions. DTI tractography can be used to reconstruct tracts involved in motor and language systems (Bello et al., 2010).

Chapter 3

Investigating the jackknife resampling technique in estimating DTI uncertainty

Mwape Mofya[1], Ali Alhamud[1], Ernesta Meintjes[1], Paul A. Taylor[1,2]

[1]MRC/UCT Medical Imaging Research Unit, Department of Human Biology, University of Cape Town, South Africa

[2]African Institute for Mathematical Sciences (AIMS), Muizenberg, Western Cape, South Africa

This chapter has been submitted to the MRI journal for review

Abstract

Proper characterization of uncertainty in derived DTI parameters is important for reliable fibre tract reconstruction, as well as for quantitative analysis of the parameters themselves. The uncertainty of DTI parameters can be quantified through statistical confidence intervals. Previously, bootstrap methods have been mostly used for this purpose. However, this requires either the acquisition of extra data or model-dependent assumptions. The jackknife resampling technique is model free, computationally efficient and, in contrast to traditional bootstrap methods, does not require several repeated acquisitions. In this study, the ability of the jackknife resampling technique to determine 95% confidence intervals of DTI parameters is investigated using realistic, simulated data. As with all statistical resampling techniques, the jackknife requires the user to choose resampling parameters: in this case the jackknife subsample fraction and the number of iterations. We have explored wide ranges of jackknife and DTI parameters to determine whether the jackknife method can provide reliable confidence intervals for DTI parameters. We have found, from simulations, that jackknife properties are consistent across a wide variety of DTI parameter values and SNR. Furthermore, 95% confidence intervals are well approximated for a jackknife fraction of approximately 0.5-0.6 and at least 300 iterations.

Keywords: jackknife; DTI; confidence interval; rician noise.

3.1 Introduction

Diffusion tensor imaging (DTI) (Basser et al., 1994b; Pierpaoli et al., 1996) is an MRI technique that exploits the diffusive mobility of randomly moving molecules in aqueous brain tissue to provide details on its microstructure and architecture within an MRI voxel. The MR signal is made sensitive to the random motion of water molecules by the application of strong diffusion sensitizing magnetic field gradients. In addition to a reference image (without diffusion weighting), at least six diffusion weighted images (DWIs) are required, with gradients applied in different directions, to estimate the diffusion tensor in each voxel, with often 30 or more acquired in research applications, in order to reduce effects of noise (Le Bihan et al., 2001). The diffusion tensor (Basser et al., 1994b; Crank, 1975), a mathematical model of diffusion in 3D space, contains information about the degree of local anisotropy and the direction of maximum diffusion in a voxel, which is assumed to coincide with the dominant orientation of white matter fiber tracts (Moseley et al., 1990).

The diffusion tensor corresponds geometrically to an ellipsoid surface with the semi-axial radii in any direction quantifying the diffusivity in that direction and whose major axis is oriented in the direction of maximum diffusivity. Rotationally invariant quantities, such as the degree of anisotropy, can be computed from the diffusion tensor voxel by voxel, and can thus provide knowledge about white matter architecture in vivo. Based on the similarities in the neighbouring voxels in the shape and direction of diffusion, continuous trajectories throughout white matter can be reconstructed in a procedure called tractography (Basser et al., 2000; Conturo et al., 1999).

The diffusion tensor, $\mathbf{D}$, is a 3×3 positive definite, symmetric matrix. Several methods of estimating $\mathbf{D}$ from DWIs exist. These include weighted and unweighted, linear and non-linear least-squares fit (see, for example (Kingsley, 2006)). Several useful measures can be extracted from $\mathbf{D}$. The *diagonalization* of $\mathbf{D}$ results in a set of three eigenvectors ($\mathbf{e}_1$, $\mathbf{e}_2$ and $\mathbf{e}_3$), which represent the unit normal and mutually orthogonal directions of a diffusion ellipsoid's semiaxes, with a corresponding set of eigenvalues (λ_1, λ_2 and λ_3) quantifying the diffusivity values, in decreasing magnitude, along those directions, respectively. Thus, the principal eigenvector, $\mathbf{e}_1$ (corresponding to the largest eigenvalue λ_1), is typically assumed to be aligned with local white matter.

Other useful DTI quantities that can be derived from $\mathbf{D}$ include the mean diffusivity (MD) and

the fractional anisotropy (FA). The MD value is simply the average of the eigenvalues. The FA value is the normalised standard deviation of the eigenvalues, taking values between 0, for isotropic diffusion, and 1, for completely anisotropic diffusion. These quantities are defined mathematically as follows:

$$\mathrm{MD} = \frac{\mathrm{Trace}(\mathbf{D})}{3} = \frac{(\lambda_1 + \lambda_2 + \lambda_3)}{3} = \langle\lambda\rangle, \tag{3.1.1}$$

$$\mathrm{FA} = \sqrt{\frac{3((\lambda_1 - \langle\lambda\rangle)^2 + (\lambda_2 - \langle\lambda\rangle)^2 + (\lambda_3 - \langle\lambda\rangle)^2)}{2(\lambda_1^2 + \lambda_2^2 + \lambda_3^2)}}. \tag{3.1.2}$$

The mean diffusivity characterizes the overall mean-squared displacement of water molecules and is affected by white matter density and integrity (Basser et al., 1994a; Pierpaoli et al., 1996). The fractional anisotropy describes how much molecular displacements vary in space and is often related to the degree of alignment of white matter fibres (Basser and Pierpaoli, 1996). FA maps can be used to define locations of white matter for tracking, with FA > 0.2 considered to be a proxy for the location of white matter in adult humans (Mori et al., 2002; Wieshmann et al., 2000). In addition, local differences in the MD and FA values in the brain have been shown to indicate serious brain disorders (Bozzali et al., 2002; Castillo et al., 2001; Guo et al., 2002a,b; Horsfield et al., 1996; Lu et al., 2003; Sorensen et al., 1999).

Algorithms that perform 3D reconstructions of white matter are collectively known as tractography. Tractography algorithms can be classified into two types: deterministic and probabilistic. Deterministic tractography algorithms such as streamline tracking (Basser et al., 2000; Conturo et al., 1999), fibre assignment by continuous tracking (FACT) (Mori et al., 1999) and EZ tracing (Terajima and Nakada, 2002) use the principal eigenvector $\mathbf{e}_1$ to determine the white matter fibre orientation in each voxel. The termination criteria for the propagation of fibre tracts are typically determined by the maximum turning angle of the tracts between voxels and the minimum FA value within a voxel, to ensure fibre tracts propagate mainly through brain regions where $\mathbf{D}$ realistically represents white matter pathways. Other deterministic algorithms such as the tensor deflection (Lazar et al., 2003) use the entire diffusion tensor to determine the direction of white matter tracts in a voxel. The accuracy of tract reconstruction is limited by several factors, including the inherent noise in DTI, low spatial resolution ($\backsim$ 2.0-3.0 mm voxel edge length), subject motion artefacts, eddy current distortions and the inherent errors in the specific tractography algorithm itself (Lazar and Alexander, 2003). These combined factors

introduce errors in fibre propagation that accumulate along the white matter trajectories, producing artefacts in the reconstruction of white matter pathways. Deterministic tractography methods do not give any indication of the 'confidence' in reconstructed trajectories. Probabilistic tractography methods aim to incorporate the local errors/uncertainty of the reconstructed white matter pathways, by using Monte Carlo repetitions to generate thousands of trajectories. With each repetition, the FA and $\mathbf{e}_1$ are perturbed at each voxel using local uncertainty (uncertainty in ellipsoid measures). A user defined threshold for the number of tracts passing through each voxel is used to determine voxels that are likely in the white matter connecting target regions of interest.

One way of estimating the uncertainty and, relatedly, the confidence intervals (CIs) of DTI estimates in an efficient manner is statistical resampling. Currently, the most commonly used model-free statistical resampling methods for determining the uncertainty of the tensor parameters are based on the bootstrap method (Efron, 1987). Bootstrap methods have been found to be suitable for statistical analysis in DTI and have been used to evaluate and compare DT-MRI acquisition schemes (Hassan et al., 2000) and tractography algorithms (Lazar et al., 2001); to derive probability density functions for DTI parameters (Pajevic and Basser, 2003); and to determine the uncertainty in DT parameters, allowing simultaneous viewing of fiber orientation and uncertainty (Jones, 2003; Jones and Pierpaoli, 2005). The disadvantage of the traditional (non-model based) bootstrap methods is that they generally require several repeated acquisitions of datasets (O'Gorman and Jones, 2006; O'Gorman and Jones, 2005; Whitcher et al., 2005), thus greatly increasing the overall scan time. The wild bootstrap (Whitcher et al., 2005) is a resampling method that can be applied, like the jackknife, without multiple acquisitions of diffusion data. However, the former method is model-dependent, unlike jackknife resampling which is a model-free technique.

In this work, we examine the suitability of jackknife resampling to characterize estimates of DTI parameters, as well as what is a reasonable range of jackknife parameters. We perform numerical simulations of different combinations of realistic DWIs with Rician noise (Drumheller, 1993; Gudbjartsson and Patz, 1995), to address the following questions:

1. Can the jackknife method be used to reliably estimate confidence intervals of DTI parameters?

2. As with all statistical resampling methods, jackknifing requires the choice of two resampling parameters: for what subsample fraction and number of iterations do estimated

confidence intervals yield reasonable uncertainty estimates?

3. How valid/similar are confidence interval estimates of uncertainty across a typical range of expected DTI values, such as might be expected in practical brain imaging?

4. Can the Gaussian approximation, which is computationally more efficient than the percentile method, be used to estimate the confidence interval limits from the distribution intervals?

First, we introduce the basic theory of jackknifing. We then describe the setup of the simulations and the parameters examined. Finally, we present the results showing the suitability of jackknife resampling to DTI uncertainty, and the recommended ranges of resampling parameters for applying the method.

3.2 Methods

3.2.1 The jackknife resampling technique

The jackknife resampling technique is a non-parametric procedure that generates a theoretical pseudo-population of a given statistic, from which the variance and bias are estimated, by randomly drawing subsets of individual measurements without replacement (Efron, 1987). Suppose we have a set of M measurements, $\mathrm{Y}= \{\mathrm{y}_1, ..., \mathrm{y}_M\}$, which can be used to calculate a parameter of interest, θ. We can create a jackknife subsample $\mathrm{Y}' = \{\mathrm{y}'_1, ..., \mathrm{y}'_{M_{\mathrm{jk}}}\}$, by randomly selecting $M_{\mathrm{jk}} < M$ measurements from Y, from which an estimate, θ', of the parameter of interest can be computed. By repeating the procedure a large number, N_{jk}, of times, we generate a distribution of estimates, $\{\theta'_i\}$ $(i = 1, ..., N_{\mathrm{jk}})$, which is used to generate a theoretical sampling distribution of θ. Finally, we use percentiles from the distribution of $\{\theta'_i\}$ to estimate a confidence interval of our original parameter of interest. Implementation of the Jackknifing procedure requires the user to chose the jackknife fraction, f_{jk} (where $f_{\mathrm{jk}} = M_{\mathrm{jk}}/M < 1$), and the number of jackknife samples, N_{jk}.

In DTI, a typical number of individual measures (i.e., DWIs) for estimating the diffusion tensor is $M = 30$ (Jones, 2004). Suppose $M_{\mathrm{jk}} = 21$ (so that $f_{\mathrm{jk}} = 0.7$) measurements are randomly drawn without replacement and used to estimate the tensor and to evaluate its parameters. Theoretically, this process can be repeated until the number of iterations, N_{jk}, reaches a maxi-

mum value of binom(M_{jk}, M), which in the current example would be $\approx 1.4 \times 10^7$. In practice, a much smaller number of iterations can be used to generate a pseudo-population of parameter estimates with the final number being when the shape of the normalized distribution has approximately converged. From this distribution, a measure of uncertainty is obtained from confidence intervals.

3.2.2 Rician noise

The basic random noise inherently present in MR magnitude images, such as DWIs, is well characterized by the Rician distribution (Drumheller, 1993; Gudbjartsson and Patz, 1995). The measured MR signal, S, is composed of two channels; real (R) and imaginary (I). The magnitude images are formed by calculating the magnitude from the real and imaginary images.

$$S = \sqrt{R^2 + I^2}, \tag{3.2.1}$$

In practice, each channel measure contains noise, which is assumed to be approximated roughly by a zero-mean Gaussian distribution G(0,σ) with the same standard deviation σ in each channel. Due to the nonlinear compositions of the channels,

$$S_{\mathrm{n}} = \sqrt{(R + \mathrm{G}(\sigma))^2 + (I + \mathrm{G}(\sigma))^2}, \tag{3.2.2}$$

the noisy magnitude signal is no longer described by a Gaussian distribution, but instead by a Rician one.

3.2.3 Simulations

Monte Carlo simulations of DWIs with Rician noise distributions were used to test the efficacy of jackknife resampling over a range of realistic DTI values. Several datasets, each consisting of a noiseless tensor with specified FA, MD and random spatial orientation $\mathbf{e}_1$, were simulated. Each dataset contained a large number (30,000) of voxels. Eigenvalues were determined by the specified FA and MD values ($\lambda_1 > \lambda_2 = \lambda_3$, for simplicity). Specified ranges of FA, relevant for white matter tracking in human adults, were: 0.2, 0.4 and 0.8. Specified ranges of MD values as observed in human adult parenchyma were (here and below, assumed physical units of MD values are 10^{-3} mm^2/s): 0.4, 0.7 (which is the average MD value in a healthy adult human

brain) and 1.0.

From the noiseless tensor datasets, noisy DWI values were created. A baseline signal, $S_0 = 1000$, was specified, and then

$$S_i = S_0 \exp(-b\mathbf{g}_i^T \mathbf{D}\mathbf{g}_i), \tag{3.2.3}$$

where $\mathbf{g}$ is the gradient, was used to specify each ith DW signal, assuming a standard DW factor of $b = 1000$ s/mm^2. As is generally the case in real data, the $b = 0$ reference was assumed to have much higher SNR than the DW images due to a less attenuated signal, as well as to a process of averaging repeated measures; here, this was approximated by simply assuming a noiseless S_0 value. For the S_i values, the selected SNR ($= S_0/\sigma$) values were: 10, 20 and 40. With noisy datasets created and noiseless values known, we then tested a range of jackknife scenarios: jackknife fractions of $f_{\rm jk}$= 0.5, 0.6, 0.7 and 0.9; and iterations of $N_{\rm jk}$ = 100, 300, 500 and 1000.

For simulations and analysis, AFNI (Cox, 1996) and FATCAT (Taylor and Saad, 2013) functions in conjunction with in-house Python scripts were used. The following steps briefly summarise our methods of simulating diffusion data and estimating confidence intervals of DTI parameters using the jackknife technique; the AFNI and FATCAT programs used in each step are given in parentheses.

1. A set of 30,000 noiseless ellipsoids (i.e., diffusion tensors $\mathbf{D}$) were calculated with desired values of FA and MD (3dEigToDT).

2. Using a set of $M = 30$ Siemens (Erlangen, Germany) DW gradients, theoretical DWIs were generated from the ellipsoids, including Rician noise of a particular SNR (3dDT-toNoisyDWI).

3. $\mathbf{D}$ and its associated parameters of interest (FA and $\mathbf{e}_1$) were estimated from a full set of M noisy DWIs (3dDWItoDT).

4. The jackknife technique (with specified $f_{\rm jk}$ and $N_{\rm jk}$) was applied to the noisy DWIs, and confidence intervals of our DT parameters of interest (FA and $\mathbf{e}_1$) were estimated (3dDWUncert). CIs were calculated using both percentiles and Gaussian approximation, for comparison.

5. The above steps were repeated for all DTI (original FA, MD and SNR) and jackknifing ($f_{\rm jk}$ and $N_{\rm jk}$) parameters.

Nonlinear fitting was used for the "full" estimate of $\mathbf{D}$ from all DWIs. Estimation of the diffusion tensor for each jackknife subsample was made using linear fitting for speed during the many iterations. Due largely to noise, both linear and nonlinear fitting can result in tensors with negative eigenvalues, in either simulated or real data. Tensors with negative eigenvalues violate the assumptions of the DTI model. FATCAT's 3dDWUncert implements a simple iterative algorithm that finds and excludes the specific signal measures that produce diffusion tensor fits with negative eigenvalues, as described by Taylor and Biswal (2011), as follows:

1. Start looping through the jackknife subsample of M_{jk} signal measures excluding the ith measure (i=1,...,M_{jk}) and estimate the diffusion tensor, $\mathbf{D}_i$, at each iteration until the estimated $\mathbf{D}_i$ possesses only positive eigenvalues; then retain that $\mathbf{D}_i$ as the tensor estimate for that iteration and proceed to the next jackknife iteration.

2. If a positive definite diffusion tensor cannot be obtained from the exclusion of any one measure, then leave out the ith measure whose exclusion results in $\mathbf{D}_i$ with the least negative eigenvalue, and repeat Step 1 with a jackknife subsample of M_{jk} - 1 signal measures.

3. Repeat Step 2 until no negative eigenvalues are obtained, or until the maximum number of "bad" signal measures, M_{bad}, is reached (where $M_{\text{jk}} - M_{\text{bad}} > 6$).

95% CIs were estimated for each of the DT parameters considered to be useful for white matter tracking (i.e., FA and the first eigenvector, $\mathbf{e}_1$). As $\mathbf{e}_1$ has two degrees of freedom, its angular uncertainty is characterized using separate orthogonal components, i.e., how far the full estimate tilts towards each of the $\mathbf{e}_2$ and $\mathbf{e}_3$ axes. If $\mathbf{e}_1$ is the principal eigenvector of the 'full' DWI set and $\mathbf{e}'_1$ is that of a jackknifed sample, then we can mathematically define our angular difference between $\mathbf{e}_1$ and $\mathbf{e}'_1$ projected along $\mathbf{e}_2$ or $\mathbf{e}_3$ as $\Delta e'_{1,2} \equiv (\mathbf{e}_1 - \mathbf{e}'_1) \cdot \mathbf{e}_2$ or $\Delta e'_{1,3} \equiv (\mathbf{e}_1 - \mathbf{e}'_1) \cdot \mathbf{e}_3$, respectively (and each projection has units in radians) (Taylor and Saad, 2013). The average angular difference for each of the components, $\Delta e'_{1,2}$ and $\Delta e'_{1,3}$, over N_{jk} iterations provides the bias in the principal eigenvector. The FA bias was calculated by finding the mean of the differences between each jackknifed FA$'$ value and the full FA value (i.e., calculated from M DWIs).

The CIs were first estimated using the percentiles of the jackknife distribution. In this method, the distribution of values generated from jackknifing was sorted from least to greatest. Then, the interval between the 2.5th and the 97.5th percentiles defined our 95% CI. Additionally,

we examined a more computationally efficient method for CI estimation, using the Gaussian approximation, which would require that the jackknifed distributions are well described by a Gaussian distribution. Therefore, a 95% CI can be estimated without sorting, instead using the mean (μ) and standard deviation (σ) of the Gaussian distribution (i.e., $\mu \pm 2\sigma$). We compared the results of the two methods (Gaussian approximation and percentile sorting) of estimating confidence intervals when using the jackknife method for DTI. For each set of parameters, the jackknife CIs were evaluated by determining the relative number of instances in which the non-noisy (or true) DTI parameter values were contained within the estimated CIs of the whole dataset. For example, having the 'true' FA value inside the estimated CI in 28500 out of the full 30,000 voxels in a dataset would correspond to a method producing a 95% CI.

3.3 Results

3.3.1 Investigating jackknife and DTI parameters

Figure 3.3.1 shows the fractions of voxels within each dataset whose CIs (between 2.5 - 97.5 percentiles) contained the noiseless measure value as a function of f_{jk} for FA, $\Delta e_{1,2}$ and $\Delta e_{1,3}$. Various jackknife and DTI parameters are varied within panels for each row of plots: 1) SNR; 2) number of jackknife iterations, N_{jk}; 3) FA; 4) MD. 'Default' parameters in each case (i.e., not explicitly varied per plot) are shown in the right column. Typically the resulting curves were similar across each variable (FA, $\Delta e_{1,2}$ and $\Delta e_{1,3}$), particularly for a given N_{jk}. The most difference was seen for the eigenvector uncertainties when changing noiseless MD and FA values (rows 3 and 4). Theoretically, the shape of diffusion affects how $\mathbf{e}_1$ is influenced by noise. For example, $\mathbf{e}_1$ is less influenced by noise for a prolate tensor than for an oblate or spherical tensor. Therefore, the differences seen in the eigenvector uncertainty when changing MD and FA are expected. The fraction in CI of 95% was seen to match with f_{jk} values of approximately 0.5-0.6.

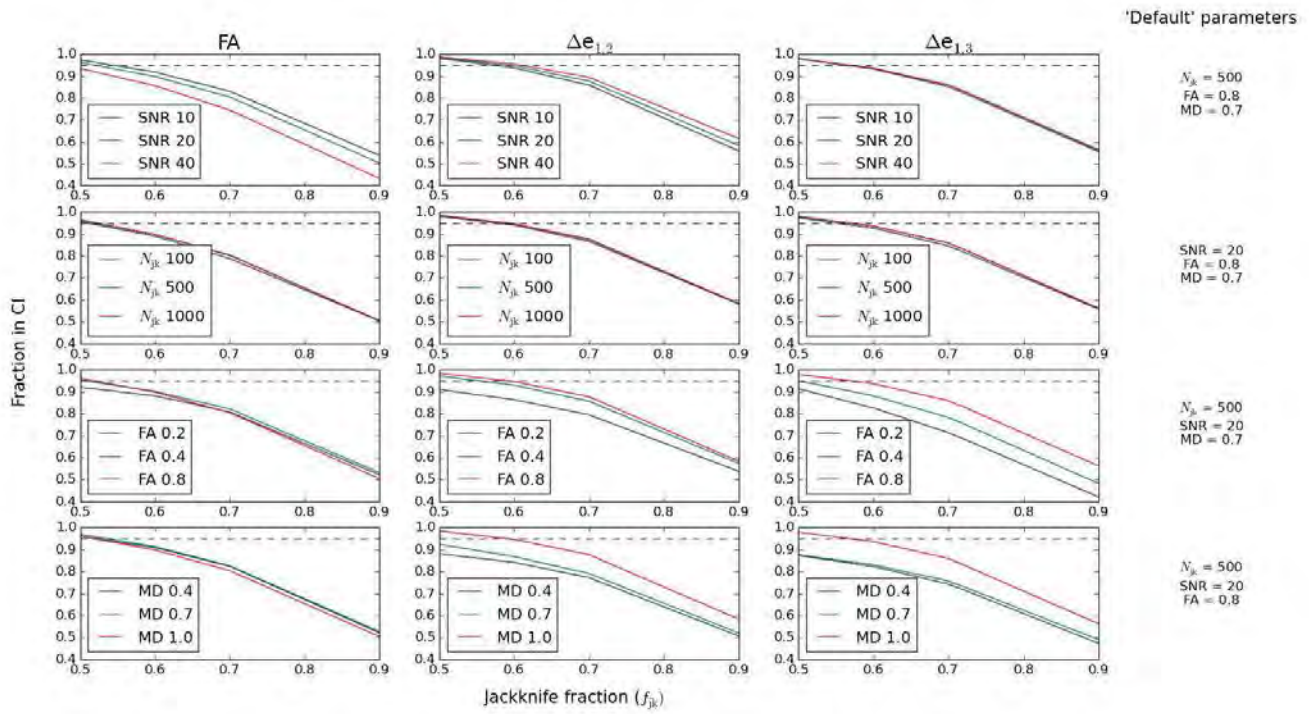

Figure 3.3.1: A graphical illustration of how the fraction of times the noiseless DTI parameter values lie within the estimated jackknife CI varies with f_{jk}. The dotted line shows a 95% confidence level, for reference. Each row shows the systematic variation of one scanner setting, resampling parameter, or DTI value; Col 1: FA; Col 2: $\Delta e_{1,2}$; Col 3: $\Delta e_{1,3}$; Col 4: the 'constant' parameters for each row.

Figure 3.3.2 shows histograms of bias and standard deviation of the FA, $\Delta e_{1,2}$ and $\Delta e_{1,3}$ for jackknife results of a single data set using different N_{jk}. In this example, FA = 0.4, MD = 0.7, SNR = 20 and $f_{\text{jk}} = 0.6$. In all panels of Figure 3.3.2, the means of the parameter bias (nearly zero in each case) and standard deviation histograms are nearly constant. The distributions of σ (2nd panel of Figure 3.3.2) are nearly identical and appear converged for all N_{jk} examined. The standard deviation in bias histograms decreases as the number of iterations increases, showing negligible difference from $N_{\text{jk}} = 300$.

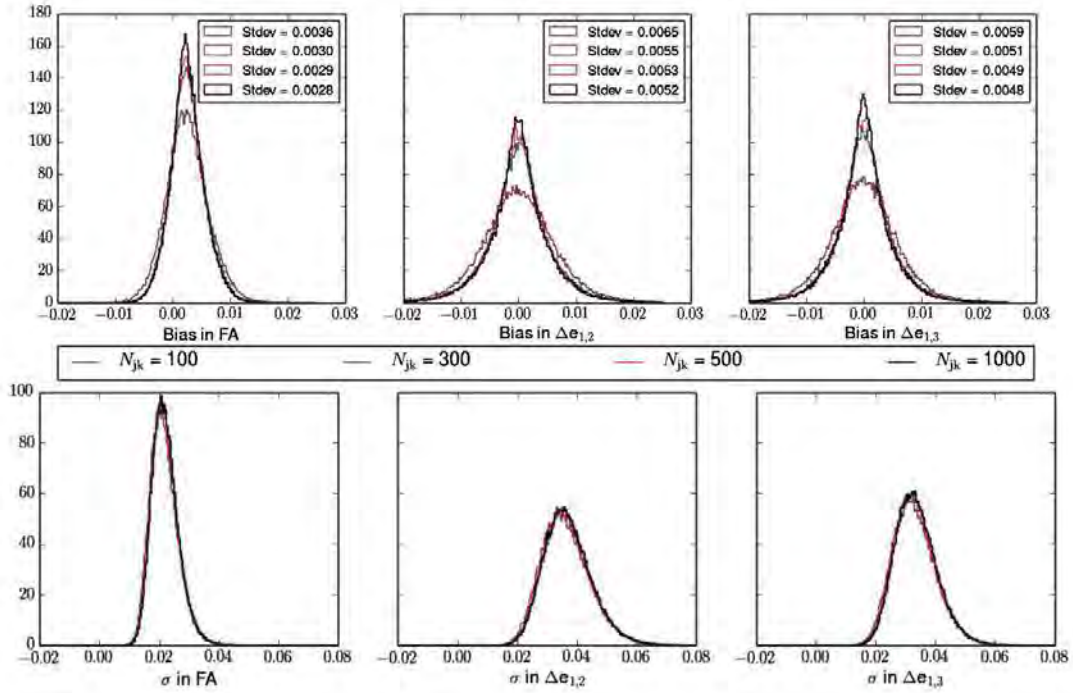

Figure 3.3.2: Normalised histograms of bias and standard deviation across a single dataset for the given values of N_{jk}; FA = 0.4, MD = 0.7, SNR = 20 and $f_{\text{jk}} = 0.6$.

3.3.2 Comparison of percentile and Gaussian approximation

The panels in Figure 3.3.3 show representative histograms of jackknifed distributions of parameters of interest (FA′, $\Delta e'_{1,2}$ and $\Delta e'_{1,3}$) from individual voxels. For visual comparison, Gaussian functions using the mean and standard deviation of the N_{jk} distribution values are overlayed on each histogram. From the plots, we see that the Gaussian function is typically a good representation of the distributions. Qualitatively, most of the distributions have roughly similar characteristics of Gaussianity (e.g., being uni-modal, bell-curve shaped and mostly lacking skewness). Row 4 has the fewest samples ($N_{\text{jk}} = 100$) in each distribution, and as expected, these distributions appear to be the least Gaussian.

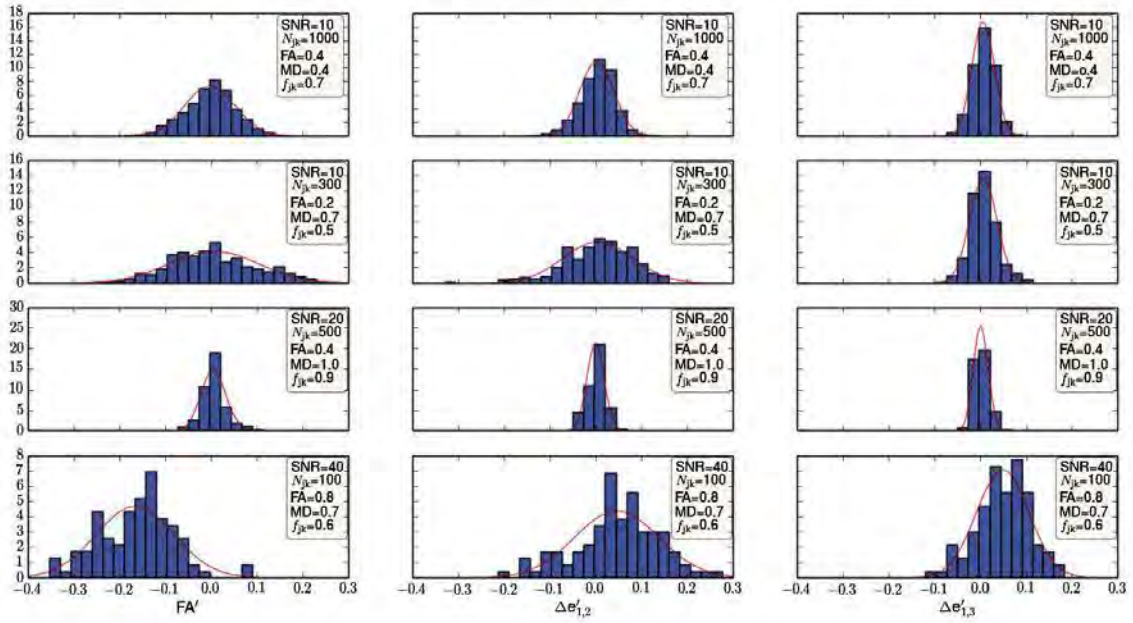

Figure 3.3.3: A few example plots of normalized jackknife distributions for individual voxels. Gaussian curves with distribution mean and standard deviation are shown for visual comparison. The general shapes of the data and the Gaussian curves compare well. The distributions in row 4, with $N_{\text{jk}} = 100$, appear least Gaussian, as expected, due to having the fewest samples.

The properties of the jackknife distributions can be further examined by comparing the CIs calculated using the explicit percentiles with those calculated using a Gaussian approximation; here, we respectively compare 95% CIs calculated using percentiles of 2.5 and 97.5, and the interval $\mu \pm 2\sigma$. Results are shown graphically in Figure 3.3.4. The two methods yield quite similar results for all parameters tested, with the Gaussian approximation method tending to have a slightly higher fraction (of order 1%) of noiseless values within the estimated CIs. In addition to permitting more efficient calculations of CIs via the Gaussian approximation, this further suggests the general Gaussianity of the typical jackknife distributions.

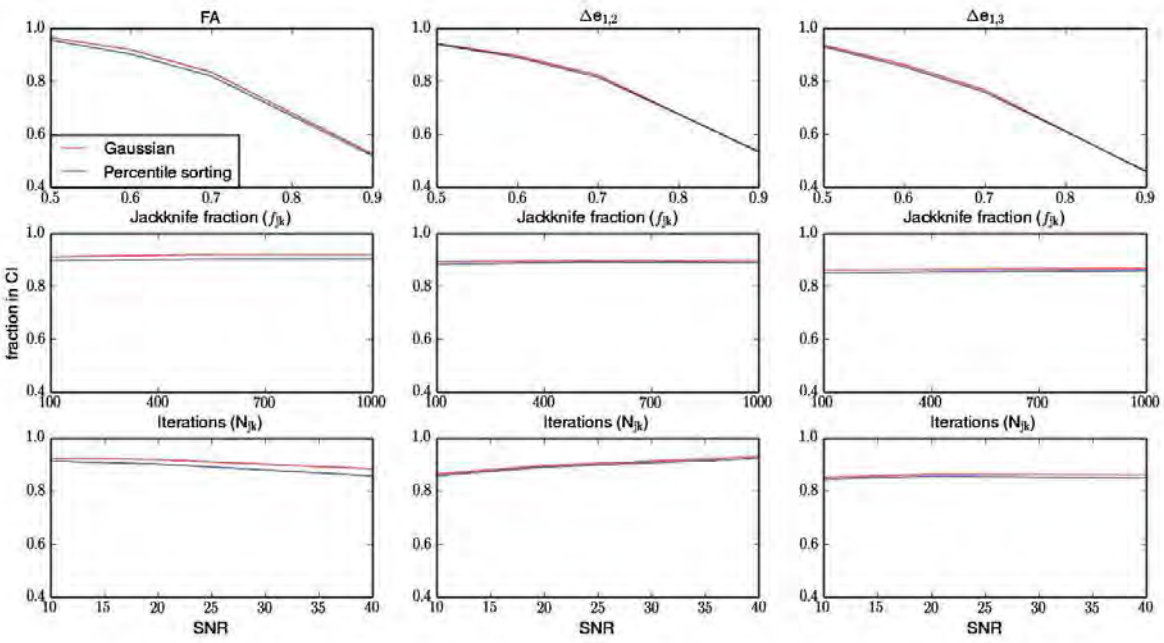

Figure 3.3.4: A comparison between the Gaussian approximation ($\mu \pm 2\sigma$) and percentile methods (2.5%-97.5%) in estimating jackknife confidence intervals for DTI parameters. The default parameters in each case except for the changing variable were SNR = 20, $N_{\text{jk}} = 500$, FA = 0.4, MD = 0.7 and $f_{\text{jk}} = 0.6$. Results with each method are quite similar in all cases.

3.4 Discussion

DTI has been a major breakthrough in white matter studies due to its ability to characterize quantitative parameters that can be used in the non-invasive delineation of white matter properties and pathways. In order to track white matter fibres in a probabilistic sense, it is important to characterise the uncertainties associated with estimated DTI parameters. In this study, we have investigated the jackknife resampling technique for estimating uncertainty in DTI parameters, using a wide range of parameters, realistic noise, and Monte Carlo simulations.

The application of the jackknife method in DTI has not been studied systematically to date. A similar non-model based resampling technique called the bootstrap method (Jones, 2003; Jones and Pierpaoli, 2005) has already been used to quantify uncertainty of DTI parameters useful for tractography. Standard bootstrap methods perform resampling across sets of repeated acquisitions (typically requiring > 4-6 repetitions to reduce bias of FA and $\mathbf{e}_1$) (Chung et al., 2006). Standard bootstrapping methods are not feasible in many scanning scenarios, such as clinical cases or in young populations who are subject to incidental motion. Additionally, with evidence that DTI parameters can be estimated more robustly when more diffusion gradients

are used (Goodlett et al., 2007), it has become common practice to use more diffusion gradients instead of multiple repetitions of the same direction.

All resampling techniques require a set of user-selected values. For example, in order to use the standard bootstrap method, the user chooses the number of repeated sets of diffusion images (Chung et al., 2006), analogous to selecting f_{jk} for jackknifing; additionally, the total number of iterations (i.e., the resampled distribution) must be chosen. Studies have shown that robust results in bootstrapping are obtained if the number of iterations (number of bootstraps) is 500 - 600 (O'Gorman and Jones, 2006; O'Gorman and Jones, 2005). Model-based bootstrap methods also require the user to input values into the method. For example, the wild bootstrap requires selection of a covariance matrix estimation and an auxiliary distribution (Whitcher et al., 2008), and optimal implementation of the wild bootstrap for DTI uncertainty estimates requires using at least 1000 wild bootstrap iterations (Zhu et al., 2008). Here, we have demonstrated the suitability of the jackknife technique to characterize diffusion parameter uncertainty, and we have examined the range of suitable method parameters, N_{jk} and f_{jk}, to be defined by the user. Theoretically, using a very low f_{jk} makes the technique susceptible to noise while a f_{jk} very close to 1 decreases statistical variability. Our results in this study demonstrate that 95% CIs are well approximated using values within an approximate interval $0.5 \leqslant f_{\mathrm{jk}} \leqslant 0.6$. This was the case for the FA and $\mathbf{e}_1$ uncertainty investigated across a wide range of SNR and ellipsoid shapes. It should also be noted that the estimated mean bias for all parameters tended to be much smaller than the standard deviation. Additionally, distribution properties appeared to be mainly converged with only about $N_{\mathrm{jk}} = 300$ iterations.

The full estimates of the diffusion tensor (i.e., the non-resampled diffusion tensor estimated from all DWIs) were calculated using nonlinear fitting, while the resampled (or jackknifed) diffusion tensors were calculated using linear fitting. Though nonlinear fitting has been shown to be more robust than linear, the former are also much more computationally demanding. Computational time for nonlinear methods can be up to 60 times more than that of linear estimation (Chang et al., 2005). Considering that the jackknife estimation needs to be iterated at least 300 times, linear fitting is more suitable for estimation of jackknife samples. From the distribution results here, this procedure did not appear to introduce bias into the significant distribution.

Tractography is a WM estimation technique which is based on the local directionality and shape of diffusion tensor ellipsoids. The confidence region of $\mathbf{e}_1$, which is assumed to indicate the fibre

tract orientation within an imaging voxel, should be quantified and visualized in 3D image space. 3D quantification and visualization of uncertainty in white matter orientation has previously been performed using the elliptical cone of uncertainty around the principal eigenvector of the diffusion tensor, whose major and minor axes coincide with the second and third eigenvectors of the diffusion tensor, respectively, and whose size is scaled by the FA (Jeong and Anderson, 2008; Koay et al., 2008). In this work, we quantified two degrees of uncertainty in $\mathbf{e}_1$ using its angular difference along the $\mathbf{e}_2$ and $\mathbf{e}_3$ axes. This directionality-dependent representation of the uncertainty in $\mathbf{e}_1$ can be an important feature during the reconstruction of fibre tracts.

As discussed in Section 3.2.2, the noise in DWIs is governed by Rician distribution. However, studies have shown that for SNR>2, the distribution is well approximated by a Gaussian distribution (Gudbjartsson and Patz, 1995). Indeed, noise perturbations can be surprisingly approximately unbiased and quasi-Gaussian in many cases (see, for example, Taylor and Biswal (2011)). In this work, we simulated DWIs with Rician noise distributions and used nonlinear signal-tensor fitting. However, we used fairly large SNRs (i.e., SNRs of 10, 20 and 40) and this explains the Gaussianity of the jackknife distributions.

In practice, there are several sources of non-physiological effects in acquired diffusion data, such as head motion, magnetic susceptibility effects, partial volume effects, etc. In this study, only Rician noise has been considered and it would be assumed that motion correction and other preprocessing would have been applied to the data. Future studies of the jackknife resampling technique with simulations of other effects, such as outliers, will be performed. For the present, jackknife uncertainty estimates can be used like the bootstrap uncertainty estimates, in quality assessment of DTI acquisitions (Lauzon et al., 2013), optimization of postprocessing protocols (Sakaie and Lowe, 2010) and fibre tracking (Jones, 2008; Jones and Pierpaoli, 2005).

3.5 Conclusion

In summary, we have demonstrated the utility of the jackknife resampling technique for diffusion tensor imaging. We have also examined the properties of the jackknife distributions by explicitly comparing the 95% CIs calculated using the Gaussian approximation with those calculated using percentile sorting. Our findings suggest that the jackknife resampling technique is suitable for DTI uncertainty measurements in whole brain data because it is not significantly affected by a wide range of variations in SNR, FA and MD, and therefore, the jackknife technique can

be used across the inhomogeneous regions of the brain. The optimal jackknife settings that resulted in well-defined 95% CIs were $N_{jk} \geqslant 300$ and $0.5 \leqslant f_{jk} \leqslant 0.6$. While both percentile and Gaussian methods yielded similar CIs, the latter are preferable due to computational efficiency. We therefore propose the use of the jackknife resampling to estimate CIs in diffusion tensor derived parameters.

Chapter 4

Methods for Simultaneous DTI-fMRI Acquisition

4.1 The navigated diffusion sequence

The twice-refocused 2D spin echo pulse sequence (TRSE) (Reese et al., 2003) was previously modified to perform prospective motion correction by acquiring an additional volumetric navigator following the acquisition of each diffusion weighted volume (Alhamud et al., 2012). The volumetric navigator is a three-dimensional multishot echo planar imaging (3D EPI) sequence element, in which a single complete slice (partition) of k-space is collected with a Cartesian sampling scheme after each excitation. The full navigator consists of a stack of k-space slices collected across multiple excitations. In contrast to the linear navigator (k-space based technique), the volumetric navigator (image based technique) contains 3D anatomical information for direct computation of motion parameters. Figure 4.1.1 summarizes the implementation of the 3D EPI navigator in the TRSE sequence. In the top part of Figure 4.1.1, the diffusion and navigator pulses (RF and gradients waveforms) are played out on the hardware of the MRI scanner, and the resulting MRI signals are then transferred to the image calculation environment (ICE). The prospective acquisition correction (PACE) algorithm (Thesen et al., 2000) shown in Figure 4.1.1, calculates motion parameters that are then sent to the sequence to update the scanner coordinate system in real time. PACE calculates motion parameters by registering each successive navigator volume to a reference volume.

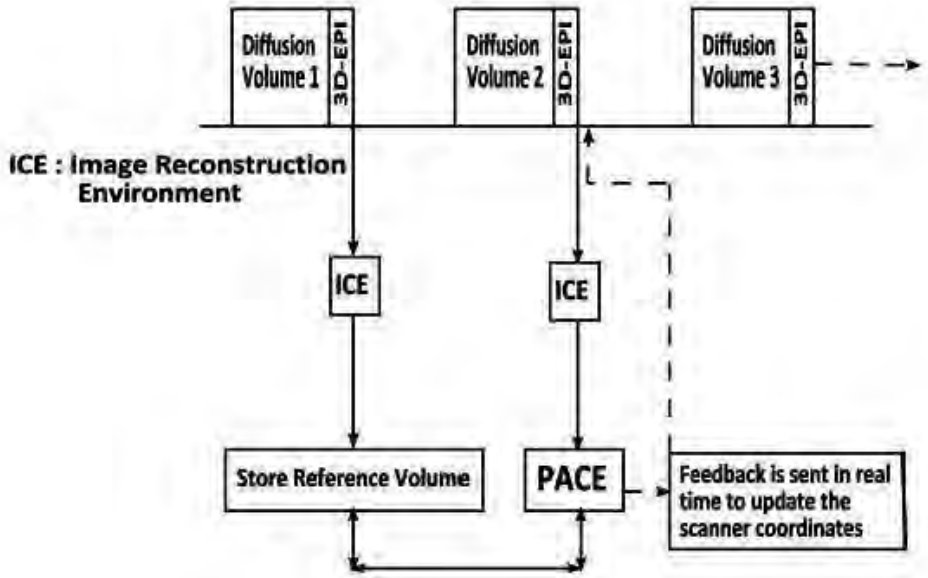

Figure 4.1.1: Flowchart of the volumetric navigated diffusion sequence. Data is transferred to ICE, registration is performed by PACE, and the subject coordinate system is updated before acquisition of the next diffusion volume. Image adapted from Alhamud et al. (2012).

In the navigated diffusion sequence (Alhamud et al., 2012), the navigator's protocol is separate from the diffusion protocol. This allows the navigator parameters to be optimized and adapted for different applications including motion correction and fMRI acquisition. For the purpose of motion correction, the navigator's parameters were implemented with a very low flip angle (2°) to minimize the impact of signal saturation on the diffusion sequence as well as with a low spatial resolution ($8 \times 8 \times 8$ mm^3) and a high receiver bandwidth (3906 Hz/px) in the readout direction to achieve rapid acquisition. For the purpose of fMRI, the navigator's protocol needed to be modified to optimise BOLD contrast by increasing the flip angle, spatial resolution, and temporal resolution. As a proof of concept, Alhamud et al. (2013) previously demonstrated successful detection of a BOLD response during a motor task using the navigator without affecting the spin history of the diffusion sequence. The navigator parameters were: spatial resolution $4 \times 4 \times 4$ mm^3, temporal resolution 6500 ms and flip angle 7° or 15°.

Despite the successful demonstration by Alhamud et al. (2013) of a BOLD response during DTI acquisition, the temporal resolution of the navigator, which is determined by the TR of the DTI sequence (6.5 s), was significantly lower than that of a standard fMRI acquisition, for which the TR is of the order 1-3 s. Furthermore, the number of fMRI measurements (34 time points) was far fewer than the standard number of measurements ($\sim$ 120 measurements) in routine fMRI. In this work, we examined the feasibility of using the simultaneous DTI-fMRI sequence used by Alhamud et al. (2013) (called from here on forward the single nav) with slightly different imaging parameters for resting state fMRI. Additionally, we explored the possibility of using

two navigators inserted within one diffusion volume (called the double nav sequence), with the aim of increasing the temporal resolution of fMRI.

In the case of the single nav, a single navigator was inserted after the acquisition of each diffusion volume and therefore all the navigator volumes experience the same amount of magnetization (spin history) from DTI slices. In the double nav sequence, one navigator was inserted into the middle of the diffusion sequence (i.e., after acquisition of the even numbered slices) and the other at the end of the diffusion sequence (after acquisition of the odd numbered slices). The first navigator excites the remaining longitudinal magnetization following excitation and partial recovery of the even numbered slices, while the second navigator excites the remaining longitudinal magnetization following excitation and partial recovery of all (even and odd) DTI slices. To ensure similar contrast between the first and second navigator, we needed the remaining longitudinal magnetization before excitation to be identical. This was achieved by exciting all DTI slices before each navigator acquisition, but only reading the signal from the even or odd echoes before the first and second navigator, respectively. Those slices not to be read had their transverse magnetization immediately destroyed (or spoiled) after excitation. In this work, we refer to the slices that are excited and read as undergoing 'normal' excitation, while those that are excited and spoiled undergo 'fast' excitation. The normal and fast excitation schemes are illustrated in Figure 4.1.2 for eight DTI slices.

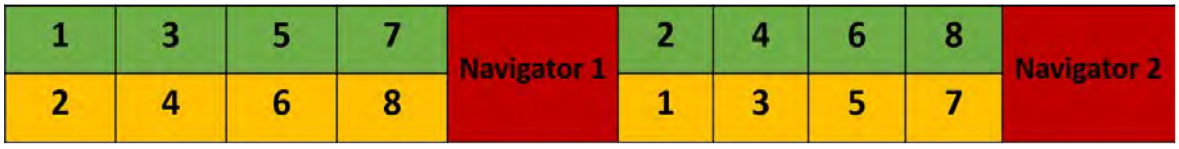

Figure 4.1.2: Double navigator DTI-fMRI excitation scheme to ensure similar contrast between the first and second navigator. The slices in the bottom yellow row are excited normally and those in the top green row are excited and spoiled. First, slice 1 is excited and spoiled (fast excitation); then, slice 2 is excited and read normally. This is repeated for slices 3 and slice 4 until the whole volume has been acquired.

Sequence timing diagram for the modified DTI sequence

The basic elements of the pulse sequence timing diagrams for the normal and fast excitation designs in the twice-refocused spin echo (TRSE) sequence are shown in Figure 4.1.3. After the fat saturation pulse is applied, the first slice is selected, excited and immediately spoiled. Slice selection of the second slice follows, which is excited normally and from which diffusion

information is acquired. In this manner each navigator will experience the same amount of spin history from excitation and recovery of all slices in the DTI acquisition (Figure 4.1.4).

A CHEmical Shift Selective (CHESS) pulse was used to perform fat suppression. This method uses a frequency-selective 90° pulse to excite the hydrogen nuclei in fat leaving the water protons unexcited. Spoiler gradients are applied immediately after the CHESS pulse to dephase the transverse fat magnetization. Since there is no remaining net magnetization from fat, fat will not contribute to the signal generated by the subsequent imaging sequence.

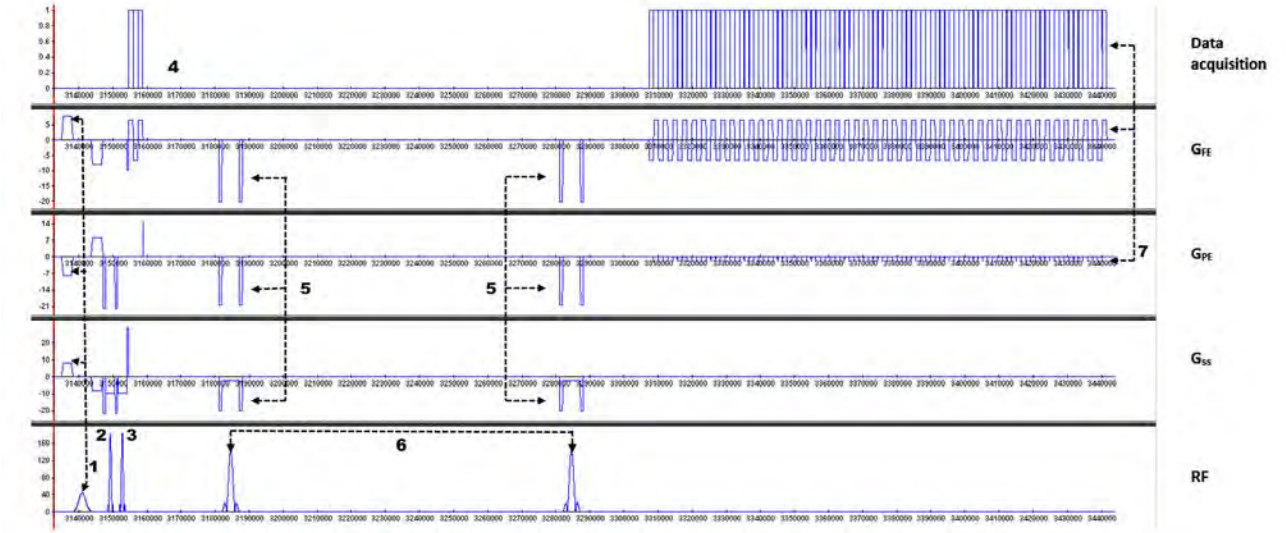

Figure 4.1.3: An illustration of the sequence elements of a single slice of the double nav pulse sequence used in this study. The elements are [1] CHESS RF pulse, [2] fast excitation pulse, [3] normal excitation pulse, [4] phase correction pulse, [5] spoiler gradients, [6] refocussing pulses of the twice-refocused spin echo (TRSE), and [7] elements of the blipped EPI readout. The x-axis represents the time and the y-axis represents the magnitude of the different components.

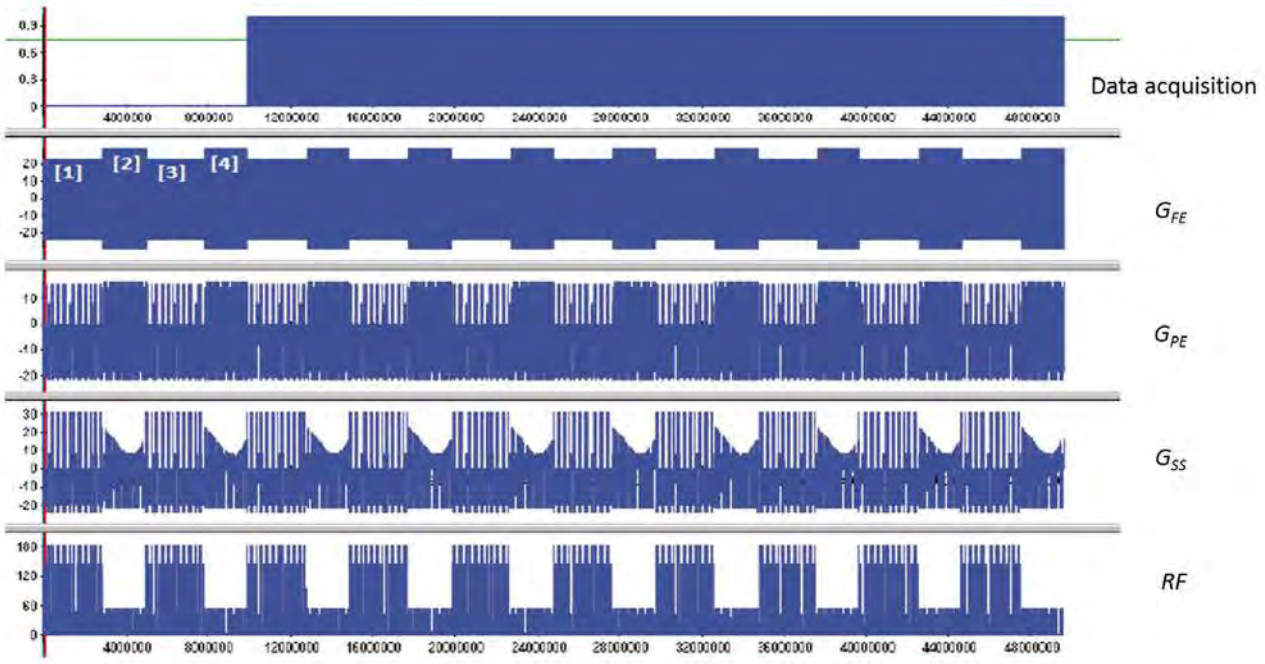

Figure 4.1.4: A sequence timing diagram for 5 diffusion volumes with 40 interleaved slices in each volume. The first volume is a dummy scan which also includes the two navigators to keep the TR consistent. The first navigator [2] is inserted after the first 20 DTI slices [1], while the second navigator [4] is inserted after the next 20 DTI slices [3].

4.2 Participants

The subjects for MRI scanning were volunteers from the University of Cape Town (UCT). The two participants (aged 25 and 37 years) were healthy male adults without any history of psychiatric or neurological disorders.

4.3 Ethics Approval

This study was approved by the Faculty of Health Sciences Human Research Ethics Committee at UCT. Prior to participation, each participant signed a written informed consent in which the procedure and the research related risks were explained. The brain scans collected from each participant were kept confidential and were identified using only a code number. This study was conducted in compliance with the International Convention on Harmonisation Good Clinical Practice (ICH GCP) guidelines.

4.4 MRI Scanning

Data acquisition was performed on a Siemens Allegra 3T scanner (Siemens Healthcare, Erlangen, Germany) at the Cape Universities Brain Imaging Center (CUBIC) in Tygerberg at the Stellenbosch University Faculty of Health Sciences, South Africa. The following scans were acquired for each participant: 1) a high resolution T_1 weighted image, 2) standard separate resting state 2D EPI BOLD and DTI, 3) simultaneous DTI-fMRI with a single navigator, and 4) simultaneous DTI-fMRI with a double navigator. During the scanning, the participants were instructed to relax and not to think about anything in particular.

The DTI sequences for the three different DTI protocols (i.e., standard DTI, single nav and double nav) use interleaved multi-slice 2D EPI. Rather than exciting the whole DTI volume (volume imaging or 3D EPI imaging), each slice is excited separately in an interleaved manner. The DTI acquisition parameters were: TR = 132.5 ms per slice, TE = 86 ms, 40 slices, matrix size = 112 × 112, voxel size = 2.5 × 2.5 × 2.5 mm^3, four b=0 scans and three repetitions of 30 non-collinear diffusion gradients for b values of 999, 1000, and 1001 s/mm^2 to achieve 94 and 188 time points for single and double navigator scans, respectively.

The T_1-weighted structural images were acquired using the motion navigated multiecho magnetization prepared rapid gradient echo (MEMPR) sequence (Tisdall et al., 2012; van der Kouwe et al., 2008) with TR 2530 msec, TEs (1.53, 3.19, 4.86, 6.53) msec, TI 1100 msec, flip angle 7°, resolution 1 × 1 ×1 mm^3, acquisition matrix 224 ×224 ×144.

The scan parameters for the 3D EPI navigators, in both the single nav and double nav sequences, were: TR = 79 ms for each partition, TE = 30 ms, voxel size = 3.9 × 3.9 × 4.0 mm^3, matrix size = 64 × 64 × 28, FOV = 250 × 250 × 112 mm^3, bandwidth = 3906 Hz/px, flip angle = 11°, total acquisition time including fat saturation and phase correction = 2.3 s. The flip angle used for the standard BOLD acquisition was 77° and the rest of the parameters were the same as for the navigator sequence. A total of 188 time points were acquired for the standard BOLD data. The temporal resolution of the rs-fMRI data were 2.3 s, 7.6 s, and 4.95 s for the standard BOLD, single nav and double nav sequences, respectively. The overall scan time with the standard BOLD sequence was 7.2 mins; the total scan times for the single nav and double nav sequences were 11.9 mins and 15.5 mins, respectively.

4.5 Analysis of fMRI data

The analysis of resting state fMRI images was performed using AFNI (Cox, 1996). All resting state functional images were compared for the same scan time. Additionally, standard and double nav resting state acquisitions were compared for the same number of time points (i.e., 188 measurements). To compare fMRI-DTI data acquired in the same scan time as the standard BOLD acquisition (7.2 mins), 57 and 87 EPI volumes from the single nav and double nav acquisitions, respectively, were used in analyses.

The first step in the analysis of rs-fMRI images was conversion of MRI DICOM images to NIFTI format. The single subject pre-processing steps of BOLD data were chosen and performed using AFNI's afni_proc.py tool. The fMRI pre-processing consisted of: 1) correction of differences in slice timing (as the slices were acquired using an interleaved sequence); 2) 3D motion correction by registering all volumes to the third volume; 3) spatial smoothing (smoothing radius 6 mm); 4) the regression of signal time courses from CSF and WM (to account for any subject motion); 5) removal of mean, linear and quadratic trends; 6) temporal filtering (low-frequency fluctuations (LFFs) range = 0.01-0.1 Hz); 7) warping to standard Talairach space to allow concordance with coordinate systems of standard BOLD, single nav and double nav sequences.

Statistical connectivity analysis was performed on the pre-processed resting state functional datasets using AFNI's InstaCorr tool. Instacorr allows the user to select a seed voxel, whose time series is correlated with that of every other voxel in the brain, to instantly visualize the functional connectivity of the whole brain to this seed. Selections of seed voxels was based on a single subject's standard BOLD resting state networks. Functional networks associated with the seed voxels were determined for each subject by thresholding the Pearson correlation values at $r > 0.5$. Networks of interest included the default mode network, the sensory motor network and the visual networks.

The quality of the imaging protocols was compared using SNR. In this work, SNR is defined, mathematically as the ratio of the mean signal intensity ($\overline{S}$) measured in an ROI in a region inside the anatomy of the object being imaged and the standard deviation (σ_N) of the signal intensity in a region outside the anatomy of the object being imaged (i.e. a region from which no brain tissue signal is obtained);

$$\text{SNR} = \frac{\overline{S}}{\sigma_N}. \tag{4.5.1}$$

Since we are more interested in signal from gray matter in fMRI, we chose an ROI in the gray matter region. For each acquisition, we placed an ROI in the same location and computed SNR at each time point. The variation of the SNR was then plotted for each acquisition.

4.6 Jackknife analysis of DTI data

Pre-processing of DWIs and subsequent analysis of DTI data involved several software tools in FSL [http://fsl.fmrib.ox.ac.uk/fsl/fslwiki/], AFNI (Abe et al., 2008)1996, FATCAT (Taylor and Saad, 2013) and in-house Python scripts. Preprocessing of DWIs involved: 1) visual image inspection to discard volumes and gradient directions with excessive motion; 2) corrections for aspects of motion, performed using FSL's mcflirt tool, by registering all the DW volumes to the first volume; and 3) averaging the first 4 b=0 scans (b_0 images) to obtain a single b_0 image with higher SNR. Nonlinear fitting of the diffusion tensors and calculation of their parameters were performed using AFNI's 3dDWItoDT. For each diffusion dataset from the three DTI protocols, the standard deviation in the FA values were estimated using AFNI's 3dDWUncert tool, which uses the jackknife resampling technique. As demonstrated in Chapter 3, optimal implementation of the jackknife resampling technique for DTI uncertainty estimates requires a jackknife fraction of approximately 0.5-0.6 and at least 300 iterations. We used a jackknife fraction of 0.55 and 500 iterations.

Differences in FA measures for the standard DTI, single nav and double nav images were compared using ROI and histogram analysis. ROIs were manually drawn on each subject's high resolution anatomical image, which was co-registered to the diffusion maps from each of the three DTI protocols. ROIs were drawn in brain specific areas of interest, including CSF (in the left and right lateral ventricles), GM (in the left and right caudate) and WM (in the body of the corpus callosum (CC)) (see Figure 4.6.1). To ensure the ROIs contained only the tissue of interest, the ROI was masked with each individual's tissue of interest masks (e.g., the WM ROI was masked with a WM mask), which were generated from AFNI's tissue segmentation function, 3dSeg. For each ROI, for each of the three DTI protocols for the same subject, the mean FA and the mean jackknife distribution standard deviation, $\overline{\sigma(\Delta \mathrm{FA})}$, over all pixels within the ROI were computed. ROI statistical comparisons between the standard DTI and the navigated DTI (i.e., single nav and double nav) sequences were performed using the paired student t-test. Histogram analysis of DTI data involved plotting distributions of whole brain FA and MD for the different DTI image acquisitions.

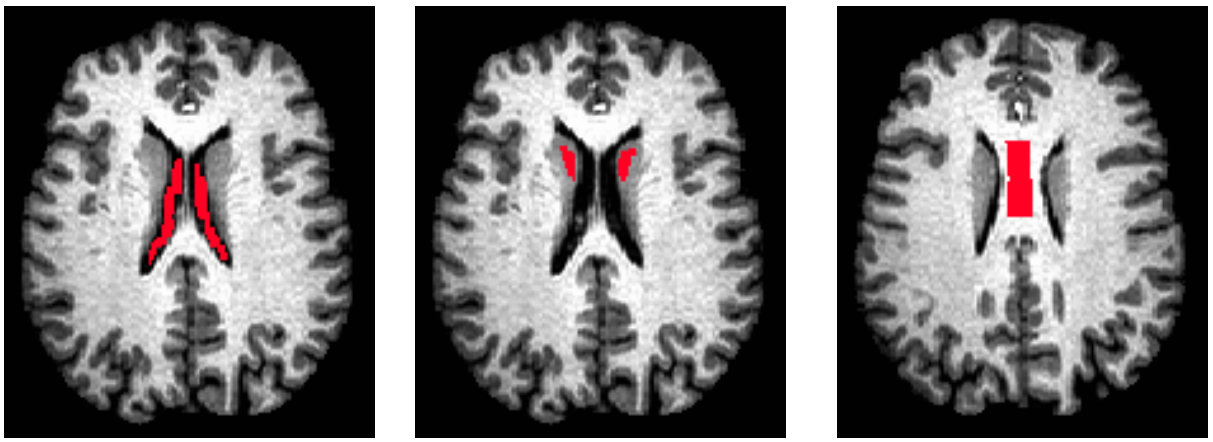

(a) CSF **(b)** GM **(c)** WM

Figure 4.6.1: ROIs used in this study. ROIs were drawn on anatomical images in selected **(a)** CSF, **(b)** GM and **(c)** WM regions for each participant.

Next, tractographic and functional connectivity comparisons were made, using the thresholded functional networks from the standard BOLD acquisition, which were mapped to each subject's diffusion space via their T_1 image. Target ROIs for tractography analysis were generated using 3dROIMaker: the cluster volume threshold was set to 15 voxels and each GM ROI was inflated by 2 voxels so that it intersected with WM. A WM skeleton was used as a guide for the ROI expansion, with the expansion terminating if it reached a WM voxel with FA > 0.25. White matter tracts between target ROIs were estimated, with the aid of DTI jackknife uncertainty estimates, using FATCAT's 3dTrackID function with the mini-probabilistic mode. The number of Monte Carlo iterations of perturbed diffusion tensor values (via jackknife uncertainty estimations) was set to 1000. Tractography results and connectivity matrices representing the mean FA values in WM regions connecting the ROIs were visualized using SUMA (Saad et al., 2004).

Chapter 5

Results for Simultaneous DTI-fMRI Acquisition

In this chapter, the results obtained from simultaneous DTI-fMRI acquisitions using the single nav and double nav protocols are presented. In addition, the DTI uncertainty results determined using the optimal jackknife settings proposed in Chapter 3 are presented.

5.1 FMRI Comparisons

In each subject, resting state networks obtained from the data acquired using the standard BOLD, single nav and the double nav sequences were compared, with the standard BOLD connectivity maps as the gold standard. After application of the same preprocessing steps to each of the fMRI datasets, a seed voxel was selected, based on the standard BOLD resting state networks, to investigate whole brain correlation to this seed using InstaCorr thresholded at $r > 0.5$. Figure 5.1.1 shows comparisons of correlation maps for four resting state networks for data acquired in 7.2 minutes of scan time using each of the three sequences (i.e., 188, 57 and 87 timepoints were acquired for the standard BOLD, single nav and double nav sequences, respectively). Talairach coordinates of seeds are provided in the figure caption. The different columns show connectivity maps for a seed in the default mode network (DMN), sensorimotor network (SMN), primary visual network (PVis) and medial visual network (MVis), respectively. Each row of Figure 5.1.1 shows images from different acquisition protocols: standard BOLD (Row 1); single nav (Row2); double nav (Row 3). In the single nav case, despite the resting

state connectivity maps being visually recognisable, they appeared quite noisy, and in some cases entire regions did not show connectivity. For example, connectivity to the seed was not observed in the medial prefrontal cortex of the DMN. The double nav connectivity maps were more similar to the standard BOLD connectivity maps, particularly for the DMN and the visual networks. However, they were not as robust as the BOLD maps in the sense that they had smaller regions showing connectivity to the seed, and showed less left-right homology for bilateral networks (e.g., in the inferior slices of the MVis and of the DMN).

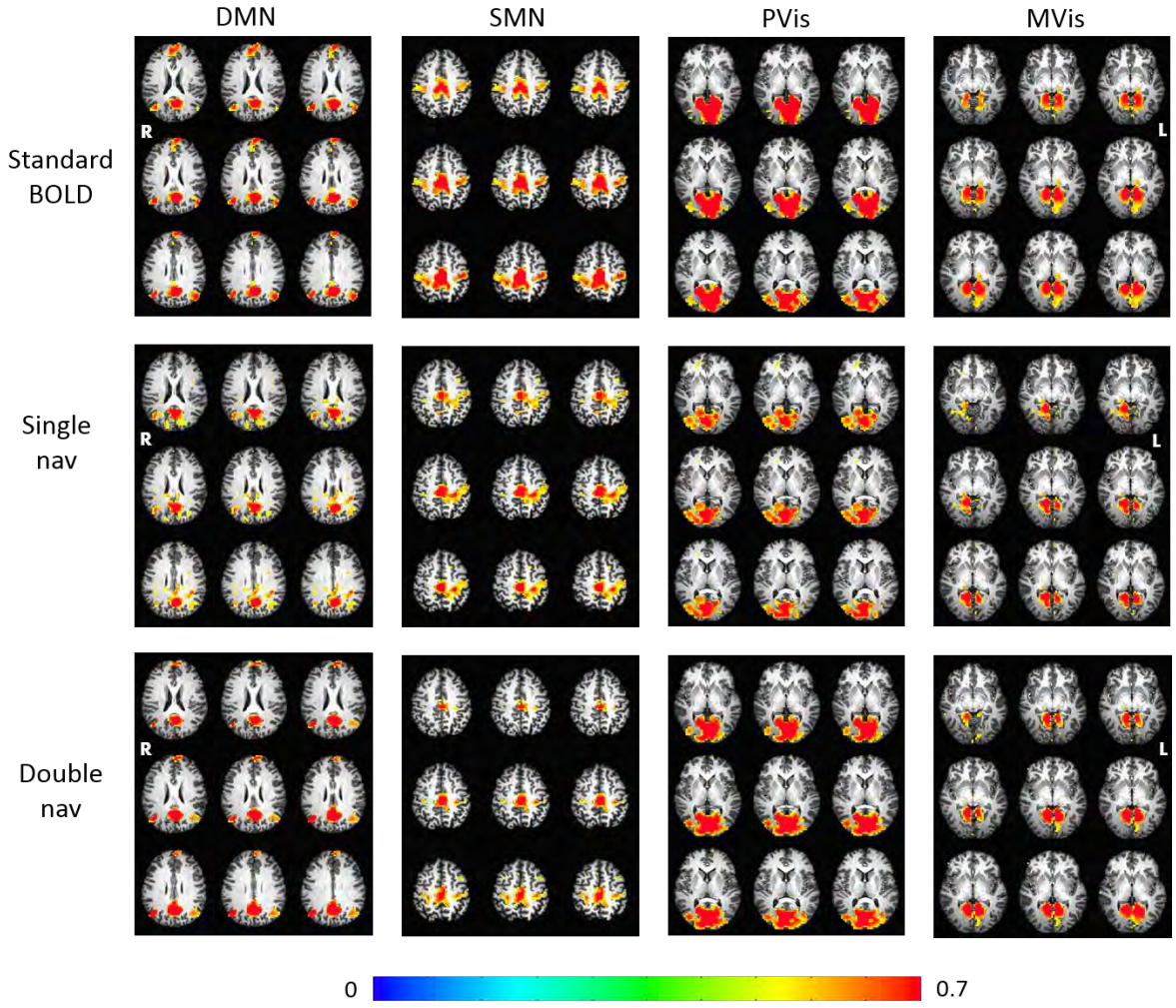

Figure 5.1.1: Spatial maps for one subject of regions functionally connected to four different seeds (columns). Connectivity maps were generated from resting state data acquired in 7.2 minutes of scanning using the standard BOLD, single nav and double nav sequences, respectively (rows), using InstaCorr and thresholded at $r > 0.5$.The single nav maps (Row 2) appear noisy and connectivity is not seen in some areas. The double nav maps (Row 3) appear more similar to the standard BOLD maps (Row 1). Talairach coordinates for the seed voxels used to generate these connectivity maps were: DMN (-1.95, 61, 29); SMN (-3.25, 24, 45); PVis(-5.85, 71, 6) and MVis(-8.45, 51, -2). DMN: default mode network. SMN: sensorimotor network. PVis: primary visual network. MVis: medial visual network.

Using the same seed for each network, standard BOLD and double nav fMRI connectivity maps

were then compared for the same number of time points. A total number of 188 time points acquired in 7.2 minutes and 11.9 minutes with the standard BOLD and double nav sequences, respectively, were used for this comparison. The results are shown in Figure 5.1.2 for the standard BOLD (Row 1) and the double nav (Row 2). Again, the double nav connectivity maps appeared quite similar to the standard BOLD connectivity maps in terms of the spatial extent of the regions showing connectivity to the seed.

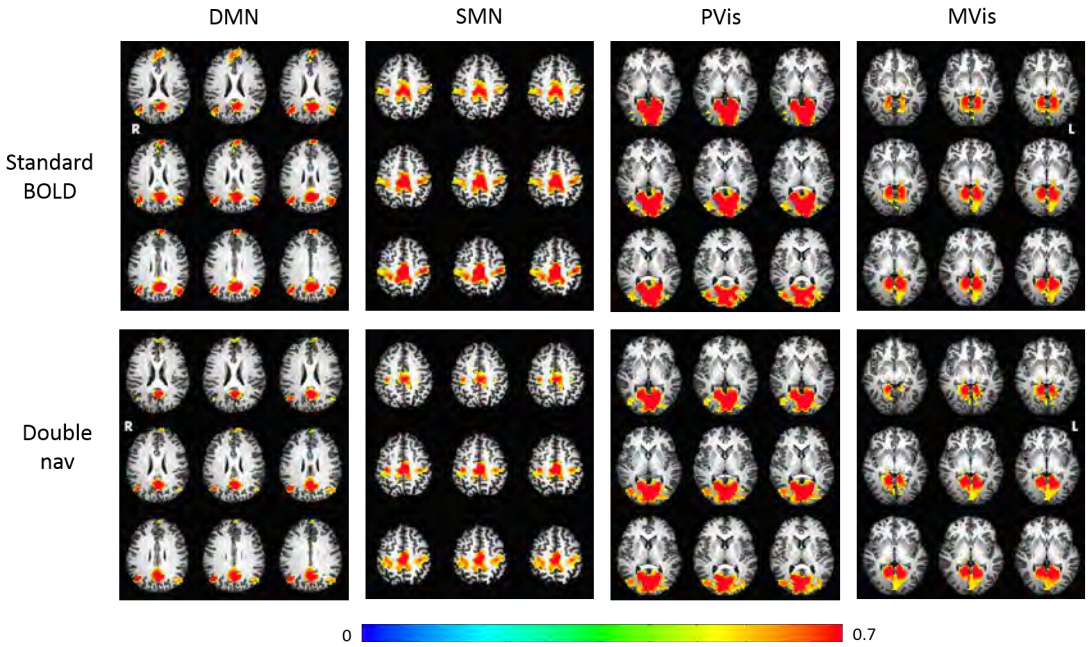

Figure 5.1.2: Spatial maps for a single subject showing regions functionally connected to four different seeds (columns) generated using InstaCorr and thresholded at $r > 0.5$, from 188 measurements obtained using the standard BOLD and double nav images from a single subject. The double nav maps (Row 2) appear similar to the standard BOLD maps (Row 1). Talairach coordinates for the seed voxels used to generate these connectivity maps were the same as those used for the same scan time comparisons [See Figure 5.1.1 caption].

SNR measurements were also used to compare the quality of the data for the different scanning sequences. Figure 5.1.3 shows the variation in SNR for the three scans for the same amount of scan time. As expected the standard BOLD sequence had the highest SNR (91.968 ± 7.205). The SNR of the double nav and single nav was comparable (47.503 ± 4.165 and 47.279 ± 2.880, respectively).

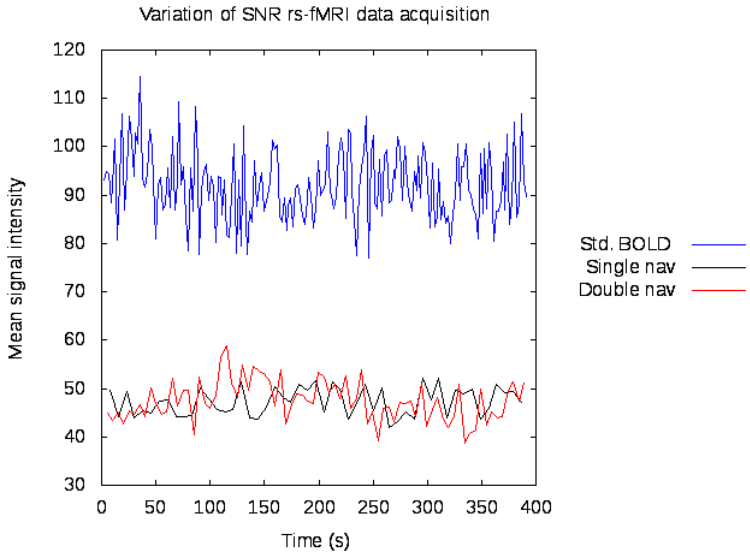

Figure 5.1.3: Plots of SNR variation for the three scans.

5.2 DTI Comparisons

The whole brain distributions of FA and MD are compared in Figure 5.2.1. The distributions are similar among the different acquisition protocols. The means of the whole brain FA and MD for the histograms of participant are given in Table 5.2.1.

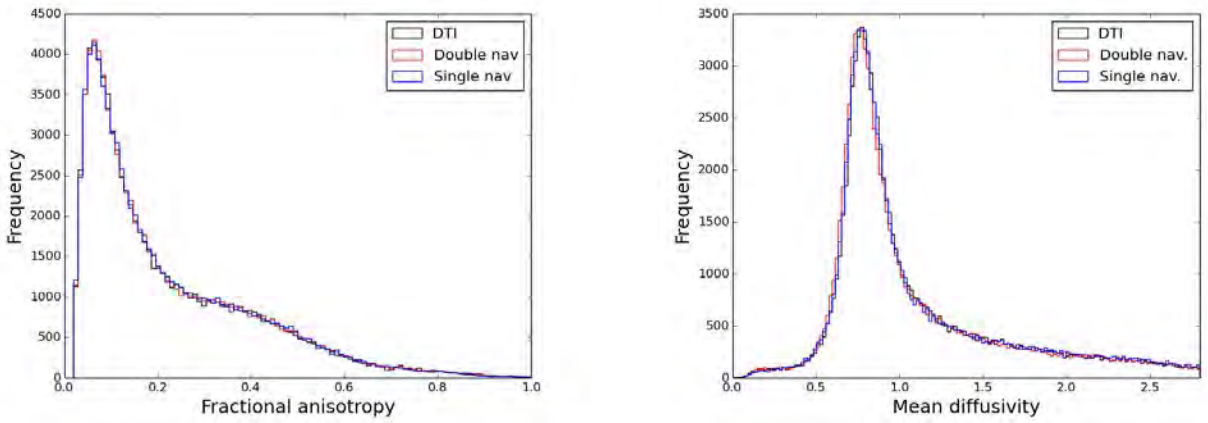

Figure 5.2.1: Distributions of whole brain FA (left) and MD (right) of DTI data acquired with and without the navigators.

	Mean FA	Mean MD
Standard DTI	0.220(±0.180)	1.127(±0.590)
Single nav	0.221(±0.181)	1.127(±0.593)
Double nav	0.221(±0.181)	1.122(±0.602)

Table 5.2.1: The average and standard deviation of the whole brain FA and MD for the three DTI acquisition protocols.

ROI analysis of DTI data included calculating the mean FA and the standard deviation of the jackknife distribution mean, $\overline{\sigma(\Delta \mathrm{FA})}$, within ROIs from three brain tissues: CSF, GM and WM. The values are shown in Table 5.2.2, along with the results of t-tests comparing results from each navigated volume to the standard one. There were few significant differences between results for the navigator and standard ROIs for mean FA and for the uncertainty values, $\overline{\sigma(\Delta \mathrm{FA})}$. In the double nav, significant differences were mainly in GM in both the mean FA and $\overline{\sigma(\Delta \mathrm{FA})}$.

	Mean FA			$\overline{\sigma(\mathbf{\Delta FA})}$		
ROI	Standard DTI	Single nav	Double nav	Standard DTI	Single nav	Double nav
WM	0.61(±0.16)	0.67(±0.25)*	0.65(±0.23)	0.05(±0.03)	0.05(±0.02)	0.06(±0.05)
GM	0.17(±0.08)	0.17(±0.08)	0.23(±0.12)***	0.04(±0.02)	0.04(±0.01)	0.05(±0.02)***
CSF	0.15(±0.09)	0.14(±0.05)	0.19(±0.08)*	0.05(±0.02)	0.06(±0.02)*	0.05(±0.02)

Table 5.2.2: Average and standard deviation of FA and jackknife uncertainty of the FA for ROIs in white matter (WM), gray matter (GM) and celebrospinal fluid (CSF) in DTI data from the standard DTI, single nav and double nav acquisitions. Significant differences in the diffusion data for the ROI analysis between the standard DTI acquisition and the single nav and double nav acquisitions are indicated by asterisks (* for $p < 0.05$, ** for $p < 0.01$ and *** for $p < 0.001$).

Further comparisons of diffusion data were made using tractography in a single network (standard BOLD DMN) for each DTI acquisition. Here, mini-probabilistic tracking using DTI jackknife estimates was used (Taylor et al., 2015). Figure 5.2.2 shows the AND-logic tracts connecting the DMN regions with ROIs mapped from the standard BOLD acquisition. Similar tractographic patterns between the standard DTI and navigated diffusion images are seen with a few visible differences highlighted with arrows.The connectivity matrices in Figure 5.2.3 show

the differences between mean FA of the standard and each of the navigated sequences for each tract connecting the pairs of ROIs. We note that overall differences are small indicating that connections derived from the three DTI protocols were overall similar.

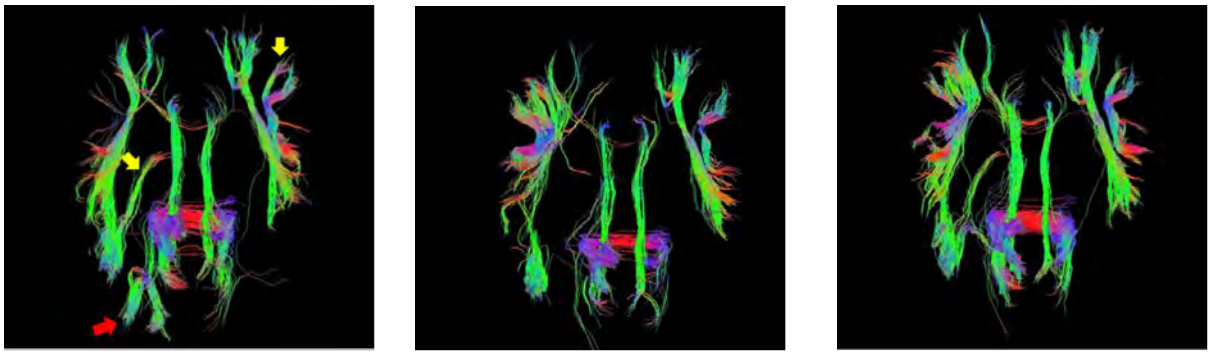

(a) DTI **(b)** single nav **(c)** double nav

Figure 5.2.2: Comparison of fibre tacking results through the ROIs generated from the activated regions forming the default mode network of the standard BOLD acquisition and mapped to the diffusion image space of both the double nav and the single nav. Noteworthy tracts that are visible in the standard DTI but are missing in both the single nav and double nav are indicated by the red arrow, while the yellow arrows indicate tracts missing in the single nav.

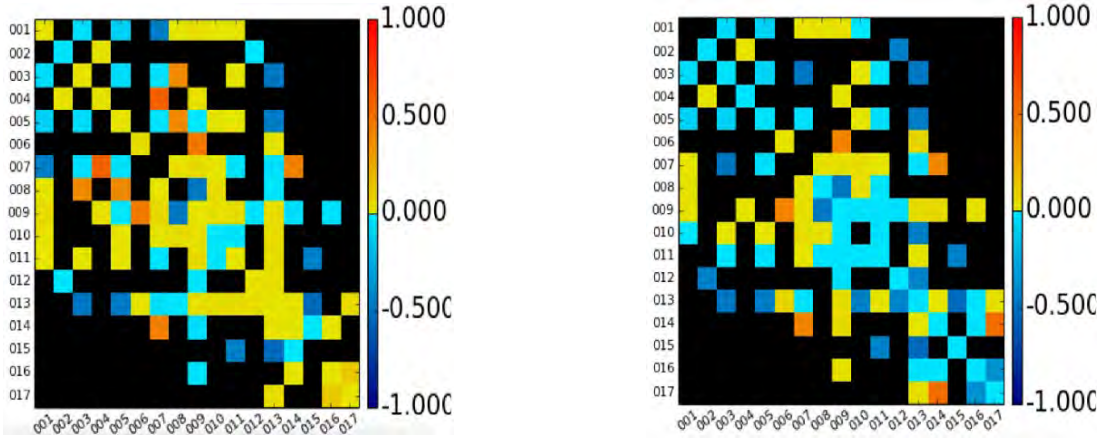

(a) **(b)**

Figure 5.2.3: Connectivity matrices showing the differences in the mean FA in WM tracts connecting pairs of ROIs in the DMN, reconstructed for the same subject in the three different DTI acquisition protocols: **(a)** double nav minus standard DTI and **(b)** single nav minus standard DTI. Cells that are coloured black represent target regions that were found not to be connected. ROIs were defined based on the thresholded DMN from the standard BOLD acquisition and were then mapped to each acquisition's diffusion space.

Chapter 6

Discussion

The aim of this study was to investigate the possibility of simultaneously acquiring diffusion and functional data using the navigated diffusion sequence (Alhamud et al., 2012). In the single nav sequence, a 3D EPI navigator inserted after each diffusion volume, is used to acquire the fMRI data. This has previously been attempted in the experiment by Alhamud et al. (2013) where activation was observed in the motor cortex during a finger tapping task. However, the spatial extent of the activation was not as large as the activation with the standard BOLD sequence. This was due to the small number of 3D EPI time points and the low temporal resolution (6.5 s). In this work, we acquired the navigated diffusion sequence data with a different choice of imaging parameters during resting state. Additionally, we aimed to increase the temporal resolution of fMRI by inserting two 3D EPI navigators in each diffusion volume (the double nav).

It is common practice in fMRI experiments to select the flip angle to be equal to the Ernst angle (Ernst, 1966), as it is at this angle that both the temporal SNR (TSNR) (the primary measure of the ability to detect BOLD signal) (Bellgowan et al., 2006; Parrish et al., 2000) and SNR of gray matter reach their maximum. Recently it has been shown that the use of flip angles other than the Ernst angle do not necessarily reduce the ability to detect BOLD signal (Gonzalez-Castillo et al., 2011). This can be exploited to perform fMRI experiments at imaging angles well below the Ernst angle. Gonzalez-Castillo et al. (2011) showed that a flip angle as low as 7.63° can be used in fMRI. In the navigated diffusion sequence, the effective TR of fMRI depends on the lengths of both the DTI and the 3D EPI acquisitions. Therefore, using flip angles lower than the Ernst angle for the 3D EPI acquisitions reduces the overall TR of fMRI. In the simultaneous DTI-fMRI experiment by Alhamud et al. (2013), flip angles of 7°

and 15° were used in the 3D EPI acquisitions. In this work, we used a flip angle of 11°, after having performed analyses to test the 3D EPI data obtained using flip angles of 7°, 11° and 15°, and finding that the 11° flip angle was best in terms of maximizing SNR while minimizing the TR.

In the single nav design of the navigated DTI sequence, each 3D EPI navigator (acquired once every DTI TR) experiences the same spin history. However, if two 3D EPI navigators are inserted at different time points in DTI volume, each navigator will experience a different spin history and this distorts the BOLD signal. To resolve this issue, we proposed the "fast and spoiling" excitation scheme to ensure that all DTI slices contribute equally to the spin history prior to each navigator excitation. Successive slices were alternately excited and immediately spoiled (fast and spoiling excitation) or excited and read (normal excitation).

In this manner, two fMRI time points were acquired in each DTI volume in the double nav sequence. Therefore, only sixty-eight time points can be acquired in one "typical" DTI sequence (consisting of four b_0 images and 30 DWIs acquired using non-collinear diffusion gradient directions). In order to achieve 94 and 188 time points for the single and double nav scans, respectively, the 30 non-collinear diffusion gradient directions were repeated three times for DW gradient values of 999, 1000 and 1001 s mm^{-2}; the sequence selection required different b values, but the values were chosen to be essentially constant.

The processing implemented in this study were typical of standard FMRI and DTI steps in the general literature. For example, single subject pre-processing of fMRI data was performed using the afni_proc.py tool. In afni_proc.py, segmentation can and was invoked through the (default) mask block via the mask_segment_anat option, which uses the 3dSeg function to segment brain volume into three tissue classes (i.e., WM, GM and CSF), from which WM and CSF were used as tissue based regressors. These masks were also used to guide the manual drawing of ROIs in GM, WM and CSF regions used for analysis in this work. Another pre-processing step performed on fMRI data was 3D motion correction by registering all volumes to the reference third volume. Typically, one of the early volumes in the time series is utilized for registration, and AFNI's 3dvolreg uses the third volume as the default reference volume.

The standard resting state 2D EPI BOLD and the navigator protocols were compared using SNR estimates. Two ROI regions were manually drawn: one in gray matter and the other outside the brain anatomy (i.e., background ROI). The SNR was calculated by finding the ratio of the mean signal in the gray matter ROI to the noise in the background ROI. To ensure

that the background ROI contained only thermal noise without artefacts, the background ROI was drawn in a region free from any visible motion and N/2 ghost artefacts. As expected, the standard BOLD sequence had the highest SNR, while the SNRs of the single and double navs were comparable to each other.

Resting state connectivity studies have typically focussed on low frequency fluctuations (< 0.1 Hz) in the BOLD fMRI signals, which are believed to originate predominantly from neuronal activity. Aliasing of higher frequency, non-neuronal noise such as cardiac and respiratory activity may occur in the sampling of resting state BOLD signals. This can be avoided by using fMRI protocols with higher sampling rates. Common rs-fMRI acquisitions use TRs of 2 to 3 s, which have a Nyquist frequency around 0.25 to 0.17 Hz (i.e., the sampling rate is at least twice the highest frequency present in the LLFs). The rs-fMRI TRs for the standard BOLD sequence, single nav and double nav were 2.3 s, 7.6 s, and 4.95 s, respectively. Therefore, the Nyquist frequencies for the single nav and double nav were 0.06 Hz and 0.1 Hz, respectively. As the Nyquist frequency of the single nav was much lower than the double nav, the likelihood of aliasing of higher frequency noise is increased in the former acquisition. Thus, finer characterization of RSNs was expected (and observed) in the double nav sequence. In addition, the single nav had fewer number of time points (57 time points) acquired in a scan time of 7.2 minutes compared to the double nav (87 time points) and standard sequences.

Uncertainty in DTI parameters have mostly been estimated using nonparametric bootstrap methods. Although the jackknife resampling technique has been used in a few recent studies (Taylor and Biswal, 2011; Taylor et al., 2015), its suitability to estimate DTI uncertainty has only recently been studied. In Chapter 3, the utility of the jackknife technique in DTI was investigated and an optimal implementation was proposed. This technique was implemented using FATCAT's 3dDWUncert function to measure bias and standard deviation in the FA for the standard DTI, single nav and double nav diffusion data in Chapter 5. The mean of the jackknife distribution standard deviation provides a measure of the noise in the DTI data for each of the three acquisitions.

Statistical analysis of DTI data acquired using the standard, single nav and double nav sequences was performed using manually selected ROIs in CSF, WM and GM regions. The mean FA and the jackknife standard error within the ROIs were calculated. ROI analysis results showed few significant differences ($p < 0.05$) in mean FA in WM and CSF between the standard DTI and the single nav. The jackknife standard error was comparable among the three

acquisition protocols, with it being slightly larger in WM for the double nav sequence compared to the standard and single nav sequences. Due to the longer acquisition of diffusion data, it was expected that noise due to head motion would be larger with the double nav. This was confirmed by additional experiments which showed that there was more translation along the *z-axis* in the double nav compared to the single nav and standard scans.

Mini-probabilitic tractography was implemented using FATCAT's 3dTrackID package, which estimates WM tracts between target ROIs and provides quantitative structural measures (such as average FA and MD) for tracts between the target ROIs. Mini-probabilistic tracking allows for the combinations of deterministic tracking and DTI parameter uncertainty measurements (from the jackknife based estimates of FATCAT's 3dDWUncert function) to be incorporated in the WM bundle estimates. Using 7 Monte Carlo iterations of perturbed DTI parameters (via jackknife uncertainty estimations), tracts connecting pairs of target ROIs were reconstructed. Visual inspection of tractography results showed similar tractographic patterns between the standard DTI and the navigated DTI acquitions. This was verified by the reconstructed FA connectivity matrices where connectivity similarities were also apparent.

In any DTI acquisition, the full set of M gradients are typically chosen to be "well-spread out" in intersecting the surface of a unit sphere (in this case, the M=30 gradients were the standard Siemens set), in order to optimize the tensor fitting Jones et al. (1999). One consideration for jackknife resampling, which was not implemented here but may be in the future, would be to require each subset of M_{jk} gradients to also be "well-spread out" in order to provide unbiased fits in the distribution. As the minimal number of gradients needed to estimate the ellipsoid surface is 6 (i.e., the number of independent terms in the DT), this requirement would likely have the largest effect in cases where the jackknife subsample M_{jk} were near to 6. In the present study in which M=30, most M_{jk} were much larger than this minimum, and therefore one would expect very few artefactual outlier estimates here. However, this subsampling "spacing" requirement would have little computational cost and allow for more generalized applications of this method.

In the histogram analysis, we showed the whole brain distributions of FA and MD. Histogram analysis reflected negligible differences between the diffusion data from the standard DTI and the navigated DTI sequences. Whole-brain distributions of FA appeared similar among the three DTI protocols.

ROI, tractograpy and histogram analyses showed similarities between the standard DTI and

the navigated DTI sequences. It is worth noting that the results presented in this work were obtained from only two subjects and should hence be considered as preliminary for future studies.

6.1 Conclusion and future work

In conclusion, this study has shown a significant 'proof of concept' of successfully acquiring simultaneous DTI and fMRI data, without the mutual interference of DTI and fMRI acquisitions, and therefore for investigating brain structural and functional connectivity simultaneously. The major challenge with the navigated diffusion sequence is the low temporal resolution of rs-fMRI. The rs-fMRI TR for the single nav was 7.6 s. With the implementation of the double nav sequence, the TR was reduced to 4.95 s. In future, we hope to further decrease the TR. This could be achieved by inserting more navigators in the DTI sequence. To make the insertion of multiple navigators more efficient, 3D EPI could be used for both DTI and fMRI parts. In this case, the entire volume in each excitation would be excited for both parts and this could significantly minimize the spin history effects. Decreasing the DTI spatial resolution would also help to decrease the TR. Lastly, motion correction can also be implemented in the double nav sequence to correct DTI and fMRI data in real time.

References

Abe, O., Yamasue, H., Aoki, S., Suga, M., Yamada, H., Kasai, K., Masutani, Y., Kato, N., Kato, N., and Ohtomo, K. (2008). Aging in the CNS: comparison of gray/white matter volume and diffusion tensor data. *Neurobiol. Aging*, 29(1):102–16.

Alexander, A. L., Tsuruda, J. S., and Parker, D. L. (1997). Elimination of eddy current artifacts in diffusion weighted echo-planar images: the use of bipolar gradients. *Magn. Reson. Med.*, 38:1016 – 1021.

Alhamud, A., Robertson, F., Donaldson, D., van der Kouwe, A. J. W., and Meintjes, E. M. (2013). Simultaneous fMRI-DTI using the Navigated Diffusion Sequence. In *Proc ISMRM Conf.*, Utah, USA.

Alhamud, A., Tisdall, M. D., Hess, A. T., Hasan, K. M., Meintjes, E. M., and van der Kouwe, A. J. W. (2012). Volumetric navigators for real-time motion correction in diffusion tensor imaging. *Magn. Reson. Med.*, 68(4):1097–108.

Basser, P. J., Mattiello, J., and LeBihan, D. (1994a). Estimation of the effective self-diffusion tensor from the NMR spin echo. *J. Magn. Reson. B*, 103(3):247–54.

Basser, P. J., Mattiello, J., and LeBihan, D. (1994b). MR diffusion tensor spectroscopy and imaging. *Biophys. J.*, 66(1):259–67.

Basser, P. J., Pajevic, S., Pierpaoli, C., Duda, J., and Aldroubi, A. (2000). In vivo fiber tractography using DT-MRI data. *Magn. Reson. Med.*, 44(4):625–32.

Basser, P. J. and Pierpaoli, C. (1996). Microstructural and physiological features of tissues elucidated by quantitative-diffusion-tensor MRI. *J. Magn. Reson. B*, 111(3):209–19.

Bellgowan, P. S. F., Bandettini, P. A., van Gelderen, P., Martin, A., and Bodurka, J. (2006). Improved BOLD detection in the medial temporal region using parallel imaging and voxel volume reduction. *Neuroimage*, 29(4):1244–51.

Bello, L., Castellano, A., Fava, E., Casaceli, G., Riva, M., Scotti, G., Gaini, S. M., and Falini, A. (2010). Intraoperative use of diffusion tensor imaging fiber tractography and subcortical mapping for resection of gliomas: technical considerations. *Neurosurg. Focus*, 28(2):E6.

Biswal, B., Zerrin Yetkin, F., Haughton, V. M., and Hyde, J. S. (1995). Functional connectivity in the motor cortex of resting human brain using echo-planar mri. *Magn. Reson. Med.*, 34(4):537–541.

Biswal, B. B., Van Kylen, J., and Hyde, J. S. (1997). Simultaneous assessment of flow and BOLD signals in resting-state functional connectivity maps. *NMR Biomed.*, 10(4-5):165–70.

Boesch, C., Gruetter, R., and Martin, E. (1991). Temporal and spatial analysis of fields generated by eddy currents in superconducting magnets: optimization of corrections and quantitative characterization of magnet/gradient systems. *Magn. Reson. Med.*, 20:268 – 284.

Bozzali, M., Falini, A., Franceschi, M., Cercignani, M., Zuffi, M., Scotti, G., Comi, G., and Filippi, M. (2002). White matter damage in Alzheimer's disease assessed in vivo using diffusion tensor magnetic resonance imaging. *J. Neurol. Neurosurg. Psychiatry*, 72(6):742–6.

Bydder, G., Hajnal, J., and Young, I. (1998). MRI: Use of the inversion recovery pulse sequence. *Clin. Radiol.*, 53(3):159–176.

Castillo, M., Smith, J. K., Kwock, L., and Wilber, K. (2001). Apparent diffusion coefficients in the evaluation of high-grade cerebral gliomas. *AJNR. Am. J. Neuroradiol.*, 22(1):60–4.

Chang, L.-C., Jones, D. K., and Pierpaoli, C. (2005). RESTORE: Robust estimation of tensors by outlier rejection. *Magn. Reson. Med.*, 53(5):1088–1095.

Chenevert, T. L., McKeever, P. E., and Ross, B. D. (1997). Monitoring early response of experimental brain tumors to therapy using diffusion magnetic resonance imaging. *Clin. Cancer Res.*, 3(9):1457–66.

Chenevert, T. L., Stegman, L. D., Taylor, J. M., Robertson, P. L., Greenberg, H. S., Rehemtulla, A., and Ross, B. D. (2000). Diffusion magnetic resonance imaging: an early surrogate marker of therapeutic efficacy in brain tumors. *J. Natl. Cancer Inst.*, 92(24):2029–36.

Cherkassky, V. L., Kana, R. K., Keller, T. A., and Just, M. A. (2006). Functional connectivity in a baseline resting-state network in autism. *Neuroreport*, 17(16):1687–90.

Chung, S., Lu, Y., and Henry, R. G. (2006). Comparison of bootstrap approaches for estimation of uncertainties of DTI parameters. *Neuroimage*, 33(2):531–41.

Clark, C. A. and Le Bihan, D. (2000). Water diffusion compartmentation and anisotropy at high b values in the human brain. *Magn. Reson. Med.*, 44(6):852–9.

Conturo, T. E., Lori, N. F., Cull, T. S., Akbudak, E., Snyder, A. Z., Shimony, J. S., McKinstry, R. C., Burton, H., and Raichle, M. E. (1999). Tracking neuronal fiber pathways in the living human brain. *Proc. Natl. Acad. Sci. U. S. A.*, 96(18):10422–7.

Cooper, R. L., Chang, D. B., Young, A. C., Martin, C. J., and Ancker-Johnson, D. (1974). Restricted diffusion in biophysical systems. Experiment. *Biophys. J.*, 14(3):161–77.

Cordes, D., Haughton, V. M., Arfanakis, K., Carew, J. D., Turski, P. A., Moritz, C. H., Quigley, M. A., and Meyerand, M. E. (2001). Frequencies contributing to functional connectivity in the cerebral cortex in "resting-state" data. *AJNR. Am. J. Neuroradiol.*, 22(7):1326–33.

Cox, R. W. (1996). AFNI: Software for Analysis and Visualization of Functional Magnetic Resonance Neuroimages. *Comput. Biomed. Res.*, 29(3):162–173.

Crank, J. (1975). *The Mathematics of Diffusion*. Oxford University Press, Oxford, 2 edition.

Damoiseaux, J. S., Rombouts, S. A. R. B., Barkhof, F., Scheltens, P., Stam, C. J., Smith, S. M., and Beckmann, C. F. (2006). Consistent resting-state networks across healthy subjects. *Proc. Natl. Acad. Sci. U. S. A.*, 103(37):13848–53.

Dougherty, R. F., Ben-Shachar, M., Bammer, R., Brewer, A. A., and Wandell, B. A. (2005). Functional organization of human occipital-callosal fiber tracts. *Proc. Natl. Acad. Sci. U. S. A.*, 102(20):7350–5.

Drumheller, D. (1993). General expressions for Rician density and distribution functions. *IEEE Trans. Aerosp. Electron. Syst.*, 29(2):580–588.

Efron, B. (1987). *The Jackknife, the Bootstrap, and Other Resampling Plans (CBMS-NSF Regional Conference Series in Applied Mathematics)*. Society for Industrial Mathematics.

Einstein, A. (1956). *Investigations on the Theory of Brownaian Movement*. Dover Publication, Inc.

Ernst, R. R. (1966). Application of Fourier Transform Spectroscopy to Magnetic Resonance. *Rev. Sci. Instrum.*, 37(1):93.

Filippi, M., Cercignani, M., Inglese, M., Horsfield, M. A., and Comi, G. (2001). Diffusion tensor magnetic resonance imaging in multiple sclerosis. *Neurology*, 56(3):304–11.

Fox, P. T. and Raichle, M. E. (1986). Focal physiological uncoupling of cerebral blood flow and oxidative metabolism during somatosensory stimulation in human subjects. *Proc. Natl. Acad. Sci. U. S. A.*, 83(4):1140–4.

Fox, P. T., Raichle, M. E., Mintun, M. A., and Dence, C. (1988). Nonoxidative glucose consumption during focal physiologic neural activity. *Science*, 241(4864):462–4.

Frahm, J., Krüger, G., Merboldt, K.-D., and Kleinschmidt, A. (1996). Dynamic uncoupling and recoupling of perfusion and oxidative metabolism during focal brain activation in man. *Magn. Reson. Med.*, 35(2):143–148.

Fukunaga, M., Horovitz, S. G., van Gelderen, P., de Zwart, J. A., Jansma, J. M., Ikonomidou, V. N., Chu, R., Deckers, R. H. R., Leopold, D. A., and Duyn, J. H. (2006). Large-amplitude, spatially correlated fluctuations in BOLD fMRI signals during extended rest and early sleep stages. *Magn. Reson. Imaging*, 24(8):979–92.

Goerke, U., Möller, H. E., Norris, D. G., and Schwarzbauer, C. (2005). A comparison of signal instability in 2D and 3D EPI resting-state fMRI. *NMR Biomed.*, 18(8):534–42.

Gonzalez-Castillo, J., Roopchansingh, V., Bandettini, P. A., and Bodurka, J. (2011). Physiological noise effects on the flip angle selection in BOLD fMRI. *Neuroimage*, 54(4):2764–78.

Goodlett, C., Fletcher, P. T., Lin, W., and Gerig, G. (2007). Quantification of measurement error in DTI: theoretical predictions and validation. *Med. Image Comput. Comput. Assist. Interv.*, 10(Pt 1):10–7.

Greicius, M. D., Krasnow, B., Reiss, A. L., and Menon, V. (2003). Functional connectivity in the resting brain: a network analysis of the default mode hypothesis. *Proc. Natl. Acad. Sci. U. S. A.*, 100(1):253–8.

Greicius, M. D., Srivastava, G., Reiss, A. L., and Menon, V. (2004). Default-mode network activity distinguishes Alzheimer's disease from healthy aging: evidence from functional MRI. *Proc. Natl. Acad. Sci. U. S. A.*, 101(13):4637–42.

Greicius, M. D., Supekar, K., Menon, V., and Dougherty, R. F. (2009). Resting-state functional connectivity reflects structural connectivity in the default mode network. *Cereb. Cortex*, 19(1):72–8.

Gudbjartsson, H. and Patz, S. (1995). The rician distribution of noisy mri data. *Magn. Reson. Med.*, 34(6):910–914.

Guo, A. C., Cummings, T. J., Dash, R. C., and Provenzale, J. M. (2002a). Lymphomas and high-grade astrocytomas: comparison of water diffusibility and histologic characteristics. *Radiology*, 224(1):177–83.

Guo, A. C., MacFall, J. R., and Provenzale, J. M. (2002b). Multiple sclerosis: diffusion tensor MR imaging for evaluation of normal-appearing white matter. *Radiology*, 222(3):729–36.

Guye, M., Parker, G. J. M., Symms, M., Boulby, P., Wheeler-Kingshott, C. A. M., Salek-Haddadi, A., Barker, G. J., and Duncan, J. S. (2003). Combined functional MRI and tractography to demonstrate the connectivity of the human primary motor cortex in vivo. *Neuroimage*, 19(4):1349–60.

Hå berg, A., Kvistad, K. A., Unsgå rd, G., and Haraldseth, O. (2004). Preoperative blood oxygen level-dependent functional magnetic resonance imaging in patients with primary brain tumors: clinical application and outcome. *Neurosurgery*, 54(4):902–14; discussion 914–5.

Haase, A., Frahm, J., Hanicke, W., and Matthaei, D. (1985). 1 H NMR chemical shift selective (CHESS) imaging. *Phys. Med. Biol.*, 30(4):341–344.

Hagmann, P., Cammoun, L., Gigandet, X., Meuli, R., Honey, C. J., Wedeen, V. J., and Sporns, O. (2008). Mapping the structural core of human cerebral cortex. *PLoS Biol.*, 6(7):e159.

Hagmann, P., Kurant, M., Gigandet, X., Thiran, P., Wedeen, V. J., Meuli, R., and Thiran, J.-P. (2007). Mapping human whole-brain structural networks with diffusion MRI. *PLoS One*, 2(7):e597.

Hassan, K. M., Parker, D. L., and Alexander, A. L. (2000). Bootstrap Analysis of DT-MRI Encoding Techniques. In *Proc 8th Annu. Meet. ISMRM*, page 789, Denver.

Heid, O. (2000). Eddy current-nulled diffusion weighting. In *Proc. 8th Annu. Meet. ISMRM*, page 799, Denver.

Hendler, T., Pianka, P., Sigal, M., Kafri, M., Ben-Bashat, D., Constantini, S., Graif, M., Fried, I., and Assaf, Y. (2003). Delineating gray and white matter involvement in brain lesions: three-dimensional alignment of functional magnetic resonance and diffusion-tensor imaging. *J. Neurosurg.*, 99(6):1018–27.

Honey, C. J., Sporns, O., Cammoun, L., Gigandet, X., Thiran, J. P., Meuli, R., and Hagmann, P. (2009). Predicting human resting-state functional connectivity from structural connectivity. *Proc. Natl. Acad. Sci. U. S. A.*, 106(6):2035–40.

Horsfield, M. A., Lai, M., Webb, S. L., Barker, G. J., Tofts, P. S., Turner, R., Rudge, P., and Miller, D. H. (1996). Apparent diffusion coefficients in benign and secondary progressive multiple sclerosis by nuclear magnetic resonance. *Magn. Reson. Med.*, 36(3):393–400.

Hsu, E. W. and Mori, S. (1995). Analytical expressions for the NMR apparent diffusion coefficients in an anisotropic system and a simplified method for determining fiber orientation. *Magn. Reson. Med.*, 34(2):194–200.

Hu, Y. and Glover, G. H. (2007). Three-dimensional spiral technique for high-resolution functional MRI. *Magn. Reson. Med.*, 58(5):947–51.

Jeong, H.-K. and Anderson, A. W. (2008). Characterizing fiber directional uncertainty in diffusion tensor MRI. *Magn. Reson. Med.*, 60(6):1408–21.

Johnston, J. M., Vaishnavi, S. N., Smyth, M. D., Zhang, D., He, B. J., Zempel, J. M., Shimony, J. S., Snyder, A. Z., and Raichle, M. E. (2008). Loss of resting interhemispheric functional connectivity after complete section of the corpus callosum. *J. Neurosci.*, 28(25):6453–8.

Jones, D., Horsfield, M., and Simmons, A. (1999). Optimal strategies for measuring diffusion in anisotropic systems by magnetic resonance imaging. *Magn. Reson. Med.*, 42(3):515–525.

Jones, D. K. (2003). Determining and visualizing uncertainty in estimates of fiber orientation from diffusion tensor MRI. *Magn. Reson. Med.*, 49(1):7–12.

Jones, D. K. (2004). The effect of gradient sampling schemes on measures derived from diffusion tensor MRI: a Monte Carlo study. *Magn. Reson. Med.*, 51(4):807–15.

Jones, D. K. (2008). Tractography gone wild: probabilistic fibre tracking using the wild bootstrap with diffusion tensor MRI. *IEEE Trans. Med. Imaging*, 27(9):1268–74.

Jones, D. K. and Pierpaoli, C. (2005). Confidence mapping in diffusion tensor magnetic resonance imaging tractography using a bootstrap approach. *Magn. Reson. Med.*, 53(5):1143–9.

Kennedy, D. P. and Courchesne, E. (2008). The intrinsic functional organization of the brain is altered in autism. *Neuroimage*, 39(4):1877–85.

Kim, M., Ducros, M., Carlson, T., Ronen, I., He, S., Ugurbil, K., and Kim, D.-S. (2006). Anatomical correlates of the functional organization in the human occipitotemporal cortex. *Magn. Reson. Imaging*, 24(5):583–90.

Kingsley, P. B. (2006). Introduction to diffusion tensor imaging mathematics: Part III. Tensor calculation, noise, simulations, and optimization. *Concepts Magn. Reson. Part A*, 28A(2):155–179.

Koay, C. G., Nevo, U., Chang, L.-C., Pierpaoli, C., and Basser, P. J. (2008). The elliptical cone of uncertainty and its normalized measures in diffusion tensor imaging. *IEEE Trans. Med. Imaging*, 27(6):834–46.

Koch, M. A., Norris, D. G., and Hund-Georgiadis, M. (2002). An investigation of functional and anatomical connectivity using magnetic resonance imaging. *Neuroimage*, 16(1):241–50.

Kono, K., Inoue, Y., Nakayama, K., Shakudo, M., Morino, M., Ohata, K., Wakasa, K., and Yamada, R. (2001). The role of diffusion-weighted imaging in patients with brain tumors. *AJNR. Am. J. Neuroradiol.*, 22(6):1081–8.

Lai, S. and Glover, G. H. (1998). Three-dimensional spiral fMRI technique: a comparison with 2D spiral acquisition. *Magn. Reson. Med.*, 39(1):68–78.

Lauterbur, P. C. (1973). Image Formation by Induced Local Interactions: Examples Employing Nuclear Magnetic Resonance. *Nature*, 242(5394):190–191.

Lauzon, C. B., Asman, A. J., Esparza, M. L., Burns, S. S., Fan, Q., Gao, Y., Anderson, A. W., Davis, N., Cutting, L. E., and Landman, B. A. (2013). Simultaneous Analysis and Quality Assurance for Diffusion Tensor Imaging. *PLoS One*, 8(4):e61737.

Lazar, M. and Alexander, A. L. (2003). An error analysis of white matter tractography methods: synthetic diffusion tensor field simulations. *Neuroimage*, 20(2):1140–53.

Lazar, M., Hasan, K. M., and Alexander, A. (2001). Bootstrap Analysis of DT-MRI Tractography Techniques: Streamlines and Tensorlines. In *Proc 9th Annu. Meet. ISMRM*, page 1527, Denver.

Lazar, M., Weinstein, D. M., Tsuruda, J. S., Hasan, K. M., Arfanakis, K., Meyerand, M. E., Badie, B., Rowley, H. A., Haughton, V., Field, A., and Alexander, A. L. (2003). White matter tractography using diffusion tensor deflection. *Hum. Brain Mapp.*, 18(4):306–21.

Le Bihan, D., Mangin, J. F., Poupon, C., Clark, C. A., Pappata, S., Molko, N., and Chabriat, H. (2001). Diffusion tensor imaging: concepts and applications. *J. Magn. Reson. Imaging*, 13(4):534–46.

Liang, M., Zhou, Y., Jiang, T., Liu, Z., Tian, L., Liu, H., and Hao, Y. (2006). Widespread functional disconnectivity in schizophrenia with resting-state functional magnetic resonance imaging. *Neuroreport*, 17(2):209–13.

Liao, W., Zhang, Z., Pan, Z., Mantini, D., Ding, J., Duan, X., Luo, C., Wang, Z., Tan, Q., Lu, G., and Chen, H. (2011). Default mode network abnormalities in mesial temporal lobe epilepsy: a study combining fMRI and DTI. *Hum. Brain Mapp.*, 32(6):883–95.

Liu, H., Buckner, R. L., Talukdar, T., Tanaka, N., Madsen, J. R., and Stufflebeam, S. M. (2009). Task-free presurgical mapping using functional magnetic resonance imaging intrinsic activity. *J. Neurosurg.*, 111(4):746–54.

Lowe, M. J., Beall, E. B., Sakaie, K. E., Koenig, K. A., Stone, L., Marrie, R. A., and Phillips, M. D. (2008). Resting state sensorimotor functional connectivity in multiple sclerosis inversely correlates with transcallosal motor pathway transverse diffusivity. *Hum. Brain Mapp.*, 29(7):818–27.

Lu, S., Ahn, D., Johnson, G., and Cha, S. (2003). Peritumoral Diffusion Tensor Imaging of High-Grade Gliomas and Metastatic Brain Tumors. *AJNR Am. J. Neuroradiol.*, 24(5):937–941.

Luo, C., Li, Q., Lai, Y., Xia, Y., Qin, Y., Liao, W., Li, S., Zhou, D., Yao, D., and Gong, Q. (2011). Altered functional connectivity in default mode network in absence epilepsy: a resting-state fMRI study. *Hum. Brain Mapp.*, 32(3):438–49.

Madsen, P. L., Hasselbalch, S. G., Hagemann, L. P., Olsen, K. S., Bülow, J., Holm, S., Wildschiø dtz, G., Paulson, O. B., and Lassen, N. A. (1995). Persistent resetting of the cerebral oxygen/glucose uptake ratio by brain activation: evidence obtained with the Kety-Schmidt technique. *J. Cereb. Blood Flow Metab.*, 15(3):485–91.

Mansfield, P. (1977). Multi-planar image formation using NMR spin echoes. *J. Phys. C Solid State Phys.*, 10(3):L55–L58.

Mardor, Y., Pfeffer, R., Spiegelmann, R., Roth, Y., Maier, S. E., Nissim, O., Berger, R., Glicksman, A., Baram, J., Orenstein, A., Cohen, J. S., and Tichler, T. (2003). Early detection

of response to radiation therapy in patients with brain malignancies using conventional and high b-value diffusion-weighted magnetic resonance imaging. *J. Clin. Oncol.*, 21(6):1094–100.

Menon, V., Ford, J. M., Lim, K. O., Glover, G. H., and Pfefferbaum, A. (1997). Combined event-related fMRI and EEG evidence for temporal-parietal cortex activation during target detection. *Neuroreport*, 8(14):3029–37.

Merboldt, K.-D., Hanicke, W., and Frahm, J. (1985). Self-diffusion NMR imaging using stimulated echoes. *J. Magn. Reson.*, 64(3):479–486.

Mori, S., Crain, B. J., Chacko, V. P., and van Zijl, P. C. (1999). Three-dimensional tracking of axonal projections in the brain by magnetic resonance imaging. *Ann. Neurol.*, 45(2):265–9.

Mori, S., Frederiksen, K., van Zijl, P. C. M., Stieltjes, B., Kraut, M. A., Solaiyappan, M., and Pomper, M. G. (2002). Brain white matter anatomy of tumor patients evaluated with diffusion tensor imaging. *Ann. Neurol.*, 51(3):377–80.

Morriss, M. C., Zimmerman, R. A., Bilaniuk, L. T., Hunter, J. V., and Haselgrove, J. C. (1999). Changes in brain water diffusion during childhood. *Neuroradiology*, 41(12):929–34.

Moseley, M. E., Cohen, Y., Kucharczyk, J., Mintorovitch, J., Asgari, H. S., Wendland, M. F., Tsuruda, J., and Norman, D. (1990). Diffusion-weighted MR imaging of anisotropic water diffusion in cat central nervous system. *Radiology*, 176(2):439–45.

Muftuler, L. T. and Nalcioglu, O. (2000). Improvement of temporal resolution in fMRI using slice phase encode reordered 3D EPI. *Magn. Reson. Med.*, 44(3):485–90.

Mukherjee, P. and McKinstry, R. C. (2006). Diffusion tensor imaging and tractography of human brain development. *Neuroimaging Clin. N. Am.*, 16(1):19–43, vii.

Mukherjee, P., Miller, J. H., Shimony, J. S., Conturo, T. E., Lee, B. C., Almli, C. R., and McKinstry, R. C. (2001). Normal brain maturation during childhood: developmental trends characterized with diffusion-tensor MR imaging. *Radiology*, 221(2):349–58.

Mulkern, R. V., Gudbjartsson, H., Westin, C. F., Zengingonul, H. P., Gartner, W., Guttmann, C. R., Robertson, R. L., Kyriakos, W., Schwartz, R., Holtzman, D., Jolesz, F. A., and Maier, S. E. (1999). Multi-component apparent diffusion coefficients in human brain. *NMR Biomed.*, 12(1):51–62.

Mullinger, K. and Bowtell, R. (2011). Combining EEG and fMRI. *Methods Mol. Biol.*, 711:303–26.

Newberg, A. B., Wang, J., Rao, H., Swanson, R. L., Wintering, N., Karp, J. S., Alavi, A., Greenberg, J. H., and Detre, J. A. (2005). Concurrent CBF and CMRGlc changes during human brain activation by combined fMRI-PET scanning. *Neuroimage*, 28(2):500–6.

Ogawa, S., Lee, T. M., Kay, A. R., and Tank, D. W. (1990a). Brain magnetic resonance imaging with contrast dependent on blood oxygenation. *Proc. Natl. Acad. Sci.*, 87(24):9868–9872.

Ogawa, S., Lee, T. M., Kay, A. R., and Tank, D. W. (1990b). Brain magnetic resonance imaging with contrast dependent on blood oxygenation. *Proc. Natl. Acad. Sci. U. S. A.*, 87(24):9868–72.

Ogawa, S., Menon, R. S., Tank, D. W., Kim, S. G., Merkle, H., Ellermann, J. M., and Ugurbil, K. (1993). Functional brain mapping by blood oxygenation level-dependent contrast magnetic resonance imaging. A comparison of signal characteristics with a biophysical model. *Biophys. J.*, 64(3):803–12.

O'Gorman, R. L. and Jones, D. K. (2006). Just how much data need to be collected for reliable bootstrap DT-MRI? *Magn. Reson. Med.*, 56:884–890.

O'Gorman, R. and Jones, D. K. (2005). How many bootstraps make a buckle? In *Proc. 13th Annu. Meet. ISMRI*, page 225, Miami Beach.

Pajevic, S. and Basser, P. J. (2003). Parametric and non-parametric statistical analysis of DT-MRI data. *J. Magn. Reson.*, 161:1–14.

Parrish, T. B., Gitelman, D. R., LaBar, K. S., and Mesulam, M. M. (2000). Impact of signal-to-noise on functional MRI. *Magn. Reson. Med.*, 44(6):925–32.

Pauling, L. and Coryell, C. D. (1936). The Magnetic Properties and Structure of Hemoglobin, Oxyhemoglobin and Carbonmonoxyhemoglobin. *Proc. Natl. Acad. Sci. U. S. A.*, 22(4):210–6.

Paulson, O. B., Hasselbalch, S. G., Rostrup, E., Knudsen, G. M., and Pelligrino, D. (2010). Cerebral blood flow response to functional activation. *J. Cereb. Blood Flow Metab.*, 30(1):2–14.

Pfefferbaum, A., Sullivan, E. V., Hedehus, M., Lim, K. O., Adalsteinsson, E., and Moseley, M. (2000). Age-related decline in brain white matter anisotropy measured with spatially corrected echo-planar diffusion tensor imaging. *Magn. Reson. Med.*, 44(2):259–68.

Pierpaoli, C., Jezzard, P., Basser, P. J., Barnett, A., and Di Chiro, G. (1996). Diffusion tensor MR imaging of the human brain. *Radiology*, 201(3):637–48.

Prichard, J., Rothman, D., Novotny, E., Petroff, O., Kuwabara, T., Avison, M., Howseman, A., Hanstock, C., and Shulman, R. (1991). Lactate rise detected by 1H NMR in human visual cortex during physiologic stimulation. *Proc. Natl. Acad. Sci. U. S. A.*, 88(13):5829–31.

Raichle, M. E., MacLeod, A. M., Snyder, A. Z., Powers, W. J., Gusnard, D. A., and Shulman, G. L. (2001). A default mode of brain function. *Proc. Natl. Acad. Sci. U. S. A.*, 98(2):676–82.

Raichle, M. E. and Snyder, A. Z. (2007). A default mode of brain function: a brief history of an evolving idea. *Neuroimage*, 37(4):1083–90; discussion 1097–9.

Reese, T. G., Heid, O., Weisskoff, R. M., and Wedeen, V. J. (2003). Reduction of eddy-current-induced distortion in diffusion MRI using a twice-refocused spin echo. *Magn. Reson. Med.*, 49(1):177–82.

Reese, T. G., Weisskoff, R. M., and Wedeen, V. J. (1998). Diffusion NMR facilitated by a refocused eddy-current EPI pulse sequence. In *Proc. 6th Annu. Meet. ISMRM*, page 663, Sydney, Australia.

Rykhlevskaia, E., Gratton, G., and Fabiani, M. (2008). Combining structural and functional neuroimaging data for studying brain connectivity: a review. *Psychophysiology*, 45(2):173–87.

Rzedzian, R., Chapman, B., Mansfield, P., Coupland, R. E., Doyle, M., Chrispin, A., Guilfoyle, D., and Small, P. (1983). Real-time nuclear magnetic resonance clinical imaging in paediatrics. *Lancet (London, England)*, 2(8362):1281–2.

Saad, Z., Reynolds, R., Argall, B., Japee, S., and Cox, R. (2004). SUMA: An interface for surface-based intra- and inter-subject analysis with AFNI. In *2004 2nd IEEE Int. Symp. Biomed. Imaging Macro to Nano (IEEE Cat No. 04EX821)*, volume 2, pages 1510–1513. IEEE.

Sakaie, K. E. and Lowe, M. J. (2010). Quantitative assessment of motion correction for high angular resolution diffusion imaging. *Magn. Reson. Imaging*, 28(2):290–6.

Salvador, R., Suckling, J., Coleman, M. R., Pickard, J. D., Menon, D., and Bullmore, E. (2005). Neurophysiological architecture of functional magnetic resonance images of human brain. *Cereb. Cortex*, 15(9):1332–42.

Sappey-Marinier, D., Calabrese, G., Fein, G., Hugg, J. W., Biggins, C., and Weiner, M. W. (1992). Effect of photic stimulation on human visual cortex lactate and phosphates using 1H and 31P magnetic resonance spectroscopy. *J. Cereb. Blood Flow Metab.*, 12(4):584–92.

Schonberg, T., Pianka, P., Hendler, T., Pasternak, O., and Assaf, Y. (2006). Characterization of displaced white matter by brain tumors using combined DTI and fMRI. *Neuroimage*, 30(4):1100–11.

Shimono, M., Mano, H., and Niki, K. (2012). The brain structural hub of interhemispheric information integration for visual motion perception. *Cereb. Cortex*, 22(2):337–44.

Shimony, J. S., Zhang, D., Johnston, J. M., Fox, M. D., Roy, A., and Leuthardt, E. C. (2009). Resting-state spontaneous fluctuations in brain activity: a new paradigm for presurgical planning using fMRI. *Acad. Radiol.*, 16(5):578–83.

Skudlarski, P., Jagannathan, K., Anderson, K., Stevens, M. C., Calhoun, V. D., Skudlarska, B. A., and Pearlson, G. (2010). Brain connectivity is not only lower but different in schizophrenia: a combined anatomical and functional approach. *Biol. Psychiatry*, 68(1):61–9.

Smits, M., Vernooij, M. W., Wielopolski, P. A., Vincent, A. J. P. E., Houston, G. C., and van der Lugt, A. (2007). Incorporating functional MR imaging into diffusion tensor tractography in the preoperative assessment of the corticospinal tract in patients with brain tumors. *AJNR. Am. J. Neuroradiol.*, 28(7):1354–61.

Sorensen, A. G., Wu, O., Copen, W. A., Davis, T. L., Gonzalez, R. G., Koroshetz, W. J., Reese, T. G., Rosen, B. R., Wedeen, V. J., and Weisskoff, R. M. (1999). Human acute cerebral ischemia: detection of changes in water diffusion anisotropy by using MR imaging. *Radiology*, 212(3):785–92.

Stejskal, E. O. and Tanner, J. E. (1965). Spin Diffusion Measurements: Spin Echoes in the Presence of a Time-Dependent Field Gradient. *J. Chem. Phys.*, 42(1):288.

Sundgren, P. C., Dong, Q., Gómez-Hassan, D., Mukherji, S. K., Maly, P., and Welsh, R. (2004). Diffusion tensor imaging of the brain: review of clinical applications. *Neuroradiology*, 46(5):339–50.

Supekar, K., Uddin, L. Q., Prater, K., Amin, H., Greicius, M. D., and Menon, V. (2010). Development of functional and structural connectivity within the default mode network in young children. *Neuroimage*, 52(1):290–301.

Taylor, D. G. and Bushell, M. C. (1985). The spatial mapping of translational diffusion coefficients by the NMR imaging technique. *Phys. Med. Biol.*, 30(4):345–349.

Taylor, P. A. and Biswal, B. (2011). Geometric analysis of the b-dependent effects of Rician signal noise on diffusion tensor imaging estimates and determining an optimal b value. *Magn. Reson. Imaging*, 29(6):777–88.

Taylor, P. A., Jacobson, S. W., van der Kouwe, A., Molteno, C. D., Chen, G., Wintermark, P., Alhamud, A., Jacobson, J. L., and Meintjes, E. M. (2015). A DTI-based tractography study of effects on brain structure associated with prenatal alcohol exposure in newborns. *Hum. Brain Mapp.*, 36(1):170–86.

Taylor, P. A. and Saad, Z. S. (2013). FATCAT: (an efficient) Functional and Tractographic Connectivity Analysis Toolbox. *Brain Connect.*, 3:523–35.

Terajima, K. and Nakada, T. (2002). EZ-tracing: a new ready-to-use algorithm for magnetic resonance tractography. *J. Neurosci. Methods*, 116(2):147–55.

Tessa, C., Michelucci, R., Nobile, C., Giannelli, M., Della Nave, R., Testoni, S., Bianucci, D., Tinuper, P., Bisulli, F., Sofia, V., De Feo, M. R., Giallonardo, A. T., Tassinari, C. A., and Mascalchi, M. (2007). Structural anomaly of left lateral temporal lobe in epilepsy due to mutated LGI1. *Neurology*, 69(12):1298–300.

Thesen, S., Heid, O., Mueller, E., and Schad, L. R. (2000). Prospective acquisition correction for head motion with image-based tracking for real-time fMRI. *Magn. Reson. Med.*, 44(3):457–65.

Thomalla, G., Glauche, V., Koch, M. A., Beaulieu, C., Weiller, C., and Röther, J. (2004). Diffusion tensor imaging detects early Wallerian degeneration of the pyramidal tract after ischemic stroke. *Neuroimage*, 22(4):1767–74.

Thulborn, K. R., Waterton, J. C., Matthews, P. M., and Radda, G. K. (1982). Oxygenation dependence of the transverse relaxation time of water protons in whole blood at high field. *Biochim. Biophys. Acta*, 714(2):265–70.

Tisdall, M. D., Hess, A. T., Reuter, M., Meintjes, E. M., Fischl, B., and van der Kouwe, A. J. W. (2012). Volumetric navigators for prospective motion correction and selective reacquisition in neuroanatomical MRI. *Magn. Reson. Med.*, 68(2):389–99.

Upadhyay, J., Ducros, M., Knaus, T. A., Lindgren, K. A., Silver, A., Tager-Flusberg, H., and Kim, D.-S. (2007). Function and connectivity in human primary auditory cortex: a combined fMRI and DTI study at 3 Tesla. *Cereb. Cortex*, 17(10):2420–32.

Valdes-Sosa, P. A., Sanchez-Bornot, J. M., Sotero, R. C., Iturria-Medina, Y., Aleman-Gomez, Y., Bosch-Bayard, J., Carbonell, F., and Ozaki, T. (2009). Model driven EEG/fMRI fusion of brain oscillations. *Hum. Brain Mapp.*, 30(9):2701–21.

van den Heuvel, M. P., Mandl, R. C. W., Kahn, R. S., and Hulshoff Pol, H. E. (2009). Functionally linked resting-state networks reflect the underlying structural connectivity architecture of the human brain. *Hum. Brain Mapp.*, 30(10):3127–41.

van der Kouwe, A. J. W., Benner, T., Salat, D. H., and Fischl, B. (2008). Brain morphometry with multiecho MPRAGE. *Neuroimage*, 40(2):559–69.

van der Kouwe, A. J. W., Wastiaux, L. M., Benner, T., and Greve, D. N. (2006). Comparison of 2D EPI and 3D Segmented EPI with Online Motion Correction for Functional MRI. In *Proc. 12th Annu. Meet. Organ. Hum. Brain Mapp.*, page 250.

Vlieger, E.-J., Majoie, C. B., Leenstra, S., and Den Heeten, G. J. (2004). Functional magnetic resonance imaging for neurosurgical planning in neurooncology. *Eur. Radiol.*, 14(7):1143–53.

Werring, D. J., Clark, C. A., Barker, G. J., Miller, D. H., Parker, G. J., Brammer, M. J., Bullmore, E. T., Giampietro, V. P., and Thompson, A. J. (1998). The structural and functional mechanisms of motor recovery: complementary use of diffusion tensor and functional magnetic resonance imaging in a traumatic injury of the internal capsule. *J. Neurol. Neurosurg. Psychiatry*, 65(6):863–9.

Werring, D. J., Clark, C. A., Parker, G. J., Miller, D. H., Thompson, A. J., and Barker, G. J. (1999). A direct demonstration of both structure and function in the visual system: combining diffusion tensor imaging with functional magnetic resonance imaging. *Neuroimage*, 9(3):352–61.

Wheeler-Kingshot, C. A. M., Parker, G. J. M., Boulby, P. A., Symms, M. R., Jones, D. K., and Barker, G. J. (2001). Investigating potential of simultaneous DT-fMRI. In *ISMRM 9th Meet.*, page 1266.

Whitcher, B., Tuch, D. S., Wisco, J. J., Sorensen, A. G., and Wang, L. (2008). Using the wild

bootstrap to quantify uncertainty in diffusion tensor imaging. *Hum. Brain Mapp.*, 29(3):346–62.

Whitcher, B., Wang, L., and Tush, D. S. (2005). The wild bootstrap to quantify variability in diffusion tensor mri. In *Proc 13th Annu. Meet. ISMRM*, page 1333.

Wieshmann, U. C., Symms, M. R., Parker, G. J., Clark, C. A., Lemieux, L., Barker, G. J., and Shorvon, S. D. (2000). Diffusion tensor imaging demonstrates deviation of fibres in normal appearing white matter adjacent to a brain tumour. *J. Neurol. Neurosurg. Psychiatry*, 68(4):501–3.

Wu, X., Li, R., Fleisher, A. S., Reiman, E. M., Guan, X., Zhang, Y., Chen, K., and Yao, L. (2011). Altered default mode network connectivity in Alzheimer's disease–a resting functional MRI and Bayesian network study. *Hum. Brain Mapp.*, 32(11):1868–81.

Zhang, D., Johnston, J. M., Fox, M. D., Leuthardt, E. C., Grubb, R. L., Chicoine, M. R., Smyth, M. D., Snyder, A. Z., Raichle, M. E., and Shimony, J. S. (2009). Preoperative sensorimotor mapping in brain tumor patients using spontaneous fluctuations in neuronal activity imaged with functional magnetic resonance imaging: initial experience. *Neurosurgery*, 65(6 Suppl):226–36.

Zhang, D. and Raichle, M. E. (2010). Disease and the brain's dark energy. *Nat. Rev. Neurol.*, 6(1):15–28.

Zhu, T., Liu, X., Connelly, P. R., and Zhong, J. (2008). An optimized wild bootstrap method for evaluation of measurement uncertainties of DTI-derived parameters in human brain. *Neuroimage*, 40(3):1144–56.